Doctoral Dissertation

Solar neutrino measurement in Super-Kamiokande-IV

(スーパーカミオカンデIVにおける太陽ニュートリノ測定)

Department of Physics, Graduate School of Science, Kobe University

Hasegawa Makoto
(長谷川 誠)

January, 2019

Abstract

Standard model is successful to describe particle physics based on gauge theory. On the other hand, a neutrino oscillation within the framework of a beyond standard model explains a deficit of solar neutrino fluxes, called solar neutrino problem. In the calculation of the solar neutrino oscillation, in general, an effect expected from matter is considered. However, a spectrum distortion expected from the matter effect have not observed clearly. Furthermore, it is concerned that the oscillation parameter, Δm^2_{21}, has a tension of $\sim 2\sigma$ between neutrino and anti-neutrino experiments. These remaining problems are main motivations on the solar neutrino observation of Super-Kamiokande (SK). SK, a neutrino experiment using a water Cherenkov detector in Japan, have observed the solar neutrino since April, 1996. In this thesis, the solar neutrino flux and oscillation parameters are calculated using SK data of 5695 days and results by all solar experiments. Moreover, improved analyses, such as an energy scale and systematic uncertainties, are applied to phase IV of SK data (SK-IV) in this thesis. The observed ^{8}B neutrino flux in combined SK is $(2.33 \pm 0.04) \times 10^6$ /cm^2/s assuming without the neutrino oscillation. The oscillation parameters obtained from the combined SK data are $\sin^2\theta_{12,\mathrm{SK}} = 0.332\ ^{+0.027}_{-0.022}$ and $\Delta m^2_{21,\mathrm{SK}} = (4.73\ ^{+1.35}_{-0.80}) \times 10^{-5}$ eV^2. These parameters obtained from all solar neutrino experiments and a reactor neutrino experiment are $\sin^2\theta_{12} = 0.310\ ^{+0.013}_{-0.012}$ and $\Delta m^2_{21} = (7.49\ ^{+0.19}_{-0.17}) \times 10^{-5}$ eV^2.

Contents

Chapter 1

Introduction

Standard Solar Model (SSM) had explained the solar structure and reactions in the Sun well. The generating process of solar neutrinos and the solar neutrino flux observed on the Earth are also predicted by the SSM. The solar neutrino is electron neutrino generated by nuclear fusion reactions in a core of the Sun. However, the observed flux on the Earth is significantly less than the expected flux by the SSM. This is called solar neutrino problem. It was thought that the deficit is caused by a neutrino oscillation that the electron neutrinos transit to other flavor neutrinos such as muon neutrino and tau neutrino. The neutrino oscillation of the solar neutrino was demonstrated by the solar neutrino experiments so far. Furthermore, the neutrino oscillation of other flavor neutrinos are also observed by other experiments. Study of the neutrino oscillation is on going as a research topic of the beyond Standard Model of particle physics.

A matter effect (MSW effect) is one of the physics target of the solar neutrino observation at Super-Kamiokande (SK). The MSW effect is that electron neutrinos oscillate more strongly than the oscillation in vacuum by interactions with the electrons in the material. However, a spectrum distortion expected from the MSW effect has not been observed.

SK detector is the largest water Cherenkov detector with purified water, in the world, and has enough energy resolution and statistics on the solar neutrino detection. SK-I was started in April, 1996 and SK-IV was stopped in May, 2018 for repair works. In the solar neutrino analysis of SK, we observe the Cherenkov light emitted from the recoil electron of the solar neutrino-electron elastic scattering in the water. From the detection information, the position of the reaction point of the event (vertex), the direction and the energy of the recoil electrons are reconstructed.

In this study, improvements of the solar neutrino analysis are done against the SK data of 2860 days from October 2008 to the end of December 2017 in SK-IV. Then, an oscillation analysis is performed using the SK data of 5695 days. For high precision observation of the solar neutrinos, I improved the energy scale in the solar neutrino analysis and re-estimated systematic uncertainties. In order to avoid possible increase of the systematic uncertainty in the energy scale from increase of the PMT gain, a gain correction was incorporated into the reconstruction program for the solar neutrino analysis. In addition, the energy scale was confirmed by electron linear accelerator (LINAC) calibration.

Chapter 2

Physics background and motivation

2.1 Neutrino in Standard Model

Standard Model (SM) of the particle physics is a theory for elementary particles and three fundamental interactions based on gauge theory [1]. As shown in Fig. 2.1, it consists of six quarks, six leptons, gauge bosons and a Higgs particle. Neutrinos (electron neutrino ν_e, muon neutrino ν_μ, and tau neutrino ν_τ) are one of the leptons in the SM. The neutrinos are electrically neutral, and defined as massless in the SM.

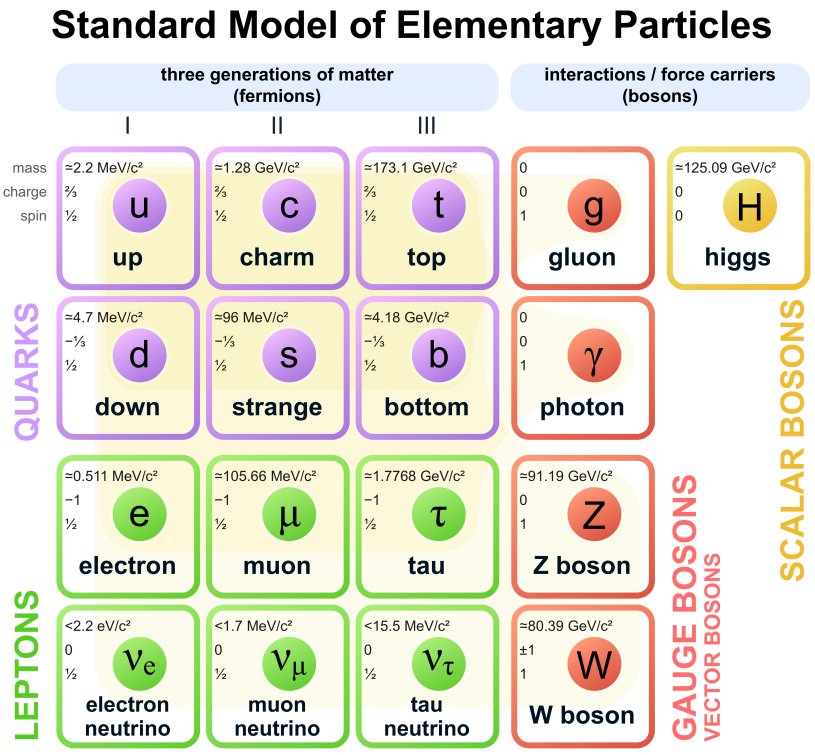

Figure 2.1: Elementary particles in the Standard Model [2]

The neutrinos interact with other particles via only weak interaction. Therefore, the cross

section of the neutrino is smaller than that of other particles. For example, the cross sections of the elastic scattering of an electron and a neutrino are shown in Fig. 2.2.

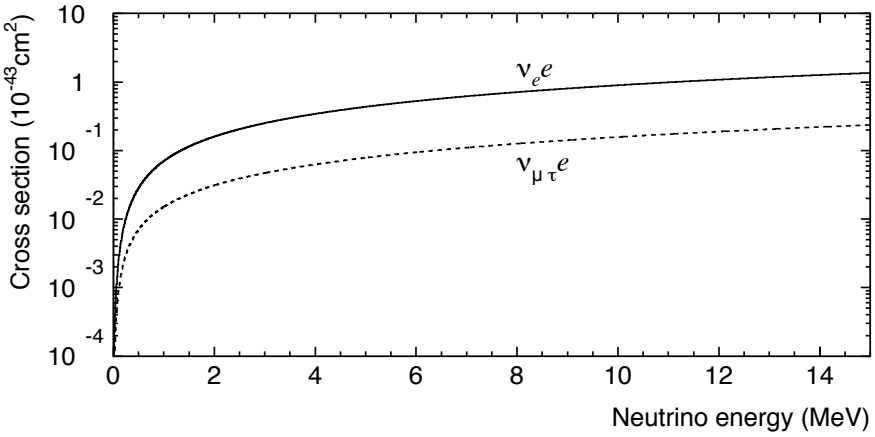

Figure 2.2: Cross section distributions of the elastic scattering of the electron and the neutrinos [3]. Difference of the cross section between ν_e and ν_μ, ν_τ is derived from that ν_μ, ν_τ are interacted with the electron via only neutral current reactions, but ν_e is interacted via both neutral current and charged current reactions.

2.2 Neutrino oscillation

Although the neutrinos are massless in SM, neutrino oscillations have been observed in reality. The neutrino oscillation can occur only when the neutrino has a finite mass. In this section, a brief summary of standard neutrino oscillation phenomenon with $m_\nu \neq 0$ will be explained.

2.2.1 Neutrino oscillation in vacuum

The flavor eigenstate of the neutrinos ν_α (α = e, μ, τ) consists of a superposition of mass eigenstate ν_l (l = 1, 2, 3) which has different mass each other. Each mass eigenstate exhibits the different behavior while the neutrino travels. Therefore, the probability of detecting each flavor state changes with time, it is named neutrino oscillation suggested by Pontecorvo [4]. Eq. 2.1 shows the superposition state of the mass eigenstate when the neutrino travels in vacuum.

$$|\nu_\alpha\rangle = \sum_l U_{\alpha l} \, |\nu_l\rangle \tag{2.1}$$

$|\nu_l\rangle$ is the mass eigenstate, $|\nu_\alpha\rangle$ is the flavor eigenstate, and U is an unitary matrix for the neutrino mixing. For the sake of simplicity, I explain that the neutrino oscillation among two flavor neutrinos (ν_α, ν_β) and the mass eigenstates (ν_1, ν_2). In such case, the unitary matrix, are defined as

$$U = \begin{pmatrix} \cos\theta & \sin\theta \\ -\sin\theta & \cos\theta \end{pmatrix} \tag{2.2}$$

where θ is a mixing angle. In the case that an initial state is Eq. 2.1, the flavor eigenstate has time development as described in Eq. 2.3, since the time dependence of the mass eigenstate ν_l with energy[1] E_ν is $|\nu_l(t)\rangle = e^{-iE_\nu t}\,|\nu_l\rangle$.

$$|\nu_\alpha(t)\rangle = \sum_l e^{-iE_\nu t} U_{\alpha l}\,|\nu_l\rangle \tag{2.3}$$

The flavor eigenstate where ν_α at $t = 0$ changes to ν_β after t s can be expressed as following equation:

$$\langle \nu_\beta \,|\, \nu_\alpha(t)\rangle = \sum_l e^{-iE_\nu t} U_{\alpha l} U^*_{\beta l.} \tag{2.4}$$

Furthermore, a probability of this neutrino mixing is described in following equation:

$$P(\nu_\alpha \to \nu_\beta) = |\,\langle \nu_\beta \,|\, \nu_\alpha(t)\rangle\,|^2 = \sum_{l,m} |U_{\alpha l} U^*_{\beta l} U_{\alpha m} U^*_{\beta m}| \cos\left(\frac{2\pi x}{L_{lm}} - \phi_{\alpha\beta lm}\right), \tag{2.5}$$

where, the time of flight (t) corresponds to the traveling distance (x) because we can assume neutrinos move with speed of light. Then, an oscillation length (L_{lm}) and a mass difference (Δm^2_{lm}) are defined as

$$L_{lm} \equiv \frac{4\pi E_\nu}{\Delta m^2_{lm}} \tag{2.6}$$

and

$$\Delta m^2_{lm} \equiv |m^2_l - m^2_m|. \tag{2.7}$$

Therefore, the oscillation probability and the survival probability by the neutrino oscillation among two flavors are represented by

$$P(\nu_\alpha \to \nu_\beta) = \sin^2 2\theta \sin^2\left(\frac{\Delta m^2_{lm}}{4E_\nu} x\right) \tag{2.8}$$

$$P(\nu_\alpha \to \nu_\alpha) = 1 - \sin^2 2\theta \sin^2\left(\frac{\Delta m^2_{lm}}{4E_\nu} x\right). \tag{2.9}$$

2.2.2 Neutrino oscillation in matter

The behavior of the neutrino oscillation is different between in vacuum and in matter because the normal matter contains electrons, but it does not contain muons and taus. It is called Mikheyev-Smirnov-Wolfenstein (MSW) effect, which was introduced by [5–7]. Therefore, an interaction in the matter is also different: electron neutrinos and electrons in the matter are affected via both

[1] Unless otherwise noted, variables for energy are defined as follows in this thesis.
Unit of these variables is [MeV].
E : Recoil electron kinetic energy
E_e : Recoil electron total energy
E_ν : Total energy of neutrino

neutral current (NC) and charged current (CC) reactions. However, the muon/tau neutrinos and electrons in the matter only interact via the neutral current reaction.

In the case of the neutrino oscillation of ν_μ and ν_e, the evolution equation and the mixing angle of the flavor eigenstate are

$$i\frac{d}{dt}\begin{pmatrix}\nu_e(t)\\ \nu_\mu(t)\end{pmatrix} = H'\begin{pmatrix}\nu_e(t)\\ \nu_\mu(t)\end{pmatrix}, \tag{2.10}$$

where

$$H' = E_\nu + \frac{m_1^2+m_2^2}{4E_\nu} + \begin{pmatrix} -\frac{\Delta m^2}{4E_\nu}\cos 2\theta & \frac{\Delta m^2}{4E_\nu}\sin 2\theta \\ \frac{\Delta m^2}{4E_\nu}\sin 2\theta & \frac{\Delta m^2}{4E_\nu}\cos 2\theta \end{pmatrix}. \tag{2.11}$$

In the matter, potential energies of the charged current and the neutral current reactions are calculated from the effective Lagrangian, respectively.

$$V_{\rm CC} = \sqrt{2}G_F n_e \tag{2.12}$$

$$V_{\rm NC} = -G_F n_n/\sqrt{2} \tag{2.13}$$

Then, these potential energies are added to Hamiltonian of the evolution equation (Eq. 2.11).

$$H = E_\nu + \frac{m_1^2+m_2^2}{4E_\nu} - \frac{1}{\sqrt{2}}G_F n_n + \begin{pmatrix} -\frac{\Delta m^2}{4E_\nu}\cos 2\theta + \sqrt{2}G_F n_e & \frac{\Delta m^2}{4E_\nu}\sin 2\theta \\ \frac{\Delta m^2}{4E_\nu}\sin 2\theta & \frac{\Delta m^2}{4E_\nu}\cos 2\theta \end{pmatrix} \tag{2.14}$$

As a result, the effective mass changes, and the mixing angle becomes biggest if the density of the number of electron satisfies $A/(\Delta m^2\cos 2\theta) = 1.0$, as shown in Fig. 2.3, where the variable A of the x-axis is proportional to the matter density. Therefore, the mixing of ν_e and ν_μ obtains the maximum by $\theta = \pi/4$ in the matter even if the mixing angle is small in the vacuum. The effective mass ($\tilde{m}_{1,2}$) under the uniform matter environment is

$$\tilde{m}_{1,2}^2 = \frac{1}{2}\left[(m_1^2+m_2^2+A \mp \sqrt{(\Delta m^2\cos 2\theta - A)^2 + (\Delta m^2 \sin 2\theta)^2})\right] \tag{2.15}$$

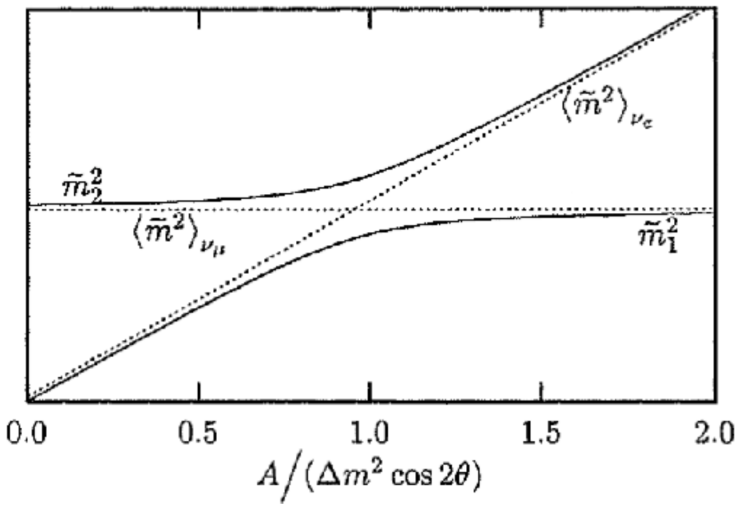

Figure 2.3: Effective mass of the ν_e and ν_μ in the matter [8].

2.3 Solar neutrino

The Sun is a fixed star at the center of the Solar System and an average distance of 1.5 $\times 10^8$ km (1 AU: astronomical unit) away from the Earth. The Sun with a diameter of about 1.4 $\times 10^6$ km consists of core, radiative zone and convection zone from the inside to the outside. Solar neutrino is the electron neutrino generated by nuclear fusion reaction in the core as shown in Eq. 2.16.

$$4p \rightarrow \alpha + 2e^+ + 2\nu_e + \gamma \tag{2.16}$$

The temperature at the center in the core is predicted approximately 1.5 $\times 10^6$ K, and gradually decreased to 6.0 $\times 10^3$ K on the surface of the Sun as shown in the left of Fig. 2.4. Therefore, the core is under a plasma state of the high electron density as shown in the right of Fig. 2.4. These solar physics such as the nuclear fusion, an evolution and a structure of the Sun are predicted by Standard Solar Model (SSM) [9–13].

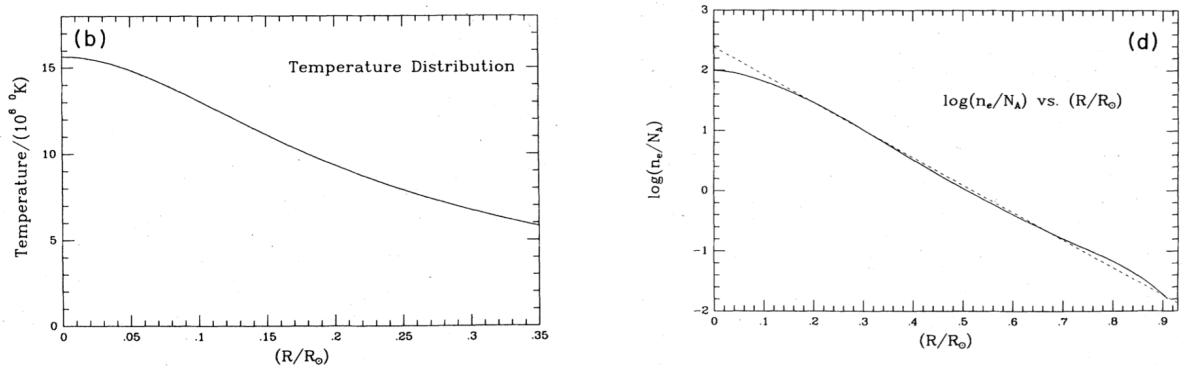

Figure 2.4: (Left) A distribution of the temperature inside the Sun [10]. The horizontal axis shows ratio of the distance from the center of the Sun and the solar radius. (Right) A distribution of the density of the electron inside the Sun.

Furthermore, the SSM also predicts the solar neutrino physics, for example, the solar neutrino production by the nuclear fusion in the core, and the solar neutrino fluxes. The nuclear fusion in the Sun has two reaction processes: Proton-proton (pp) chain and Carbon-Nitrogen-Oxygen (CNO) cycle. Under the current solar temperature environment, the nuclear fusion mainly occurs via the pp-chain. On the other hand, the CNO cycle occurs at higher temperature. The pp-chain reactions of the nuclear fusion are shown in Fig. 2.5.

The solar neutrinos are generated via decays of several elements in the pp-chain reactions and travel from the solar core to the Earth with a speed of light because the cross section of the neutrino is very small. Expected spectrum of the solar neutrino fluxes observed on the Earth is estimated by a SSM [11] as shown in Fig. 2.6. List of the solar neutrino fluxes from each reaction in the pp-chain is shown in Table 2.1.

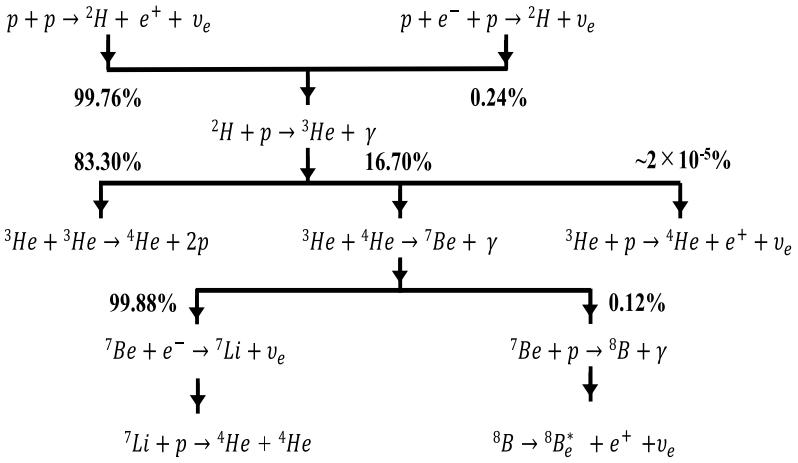

Figure 2.5: pp-chain reaction of the nuclear fusion

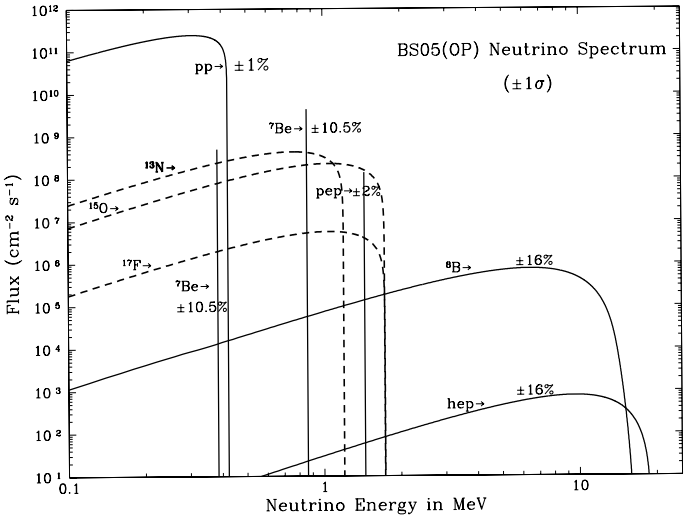

Figure 2.6: Expected energy spectrum of the solar neutrino flux from the Sun [11]

Table 2.1: Solar neutrino fluxes of each reaction in the pp-chain [12].

Source	BP 2004 expected flux [/cm^2/s]
pp	$5.94(1 \pm 0.01) \times 10^{10}$
pep	$1.40(1 \pm 0.02) \times 10^{8}$
hep	$7.88(1 \pm 0.16) \times 10^{3}$
^{7}Be	$4.86(1 \pm 0.12) \times 10^{9}$
^{8}B	$5.79(1 \pm 0.23) \times 10^{6}$

2.4 Solar neutrino experiments

In this section, the solar neutrino experiments are introduced. Furthermore, KamLAND experiment, a reactor neutrino experiment, is also introduced.

2.4.1 Homestake

Homestake experiment [14] is the first neutrino experiment targeting to observe the electron neutrino from the Sun. The experiment counts the number of ^{37}Ar via the following reaction based on a radiochemical detection and estimates the electron neutrino reaction rate.

$$\nu_e + {}^{37}\mathrm{Cl} \rightarrow \mathrm{e}^- + {}^{37}\mathrm{Ar} \tag{2.17}$$

The Homestake experiment has a target mass of 615 metric tons. An energy threshold of the Homestake experiment is 0.814 MeV, then the solar neutrino derived from ^{7}Be and ^{8}B in the pp-chain are the main experimental target.

The advantage of the radiochemical detection is that the neutrino can be detected in the low energy region ($\sim$1 MeV). However, an energy, a traveling direction and an arrival time of the electron neutrino can not be measured. The latest result from the Homestake experiment [14] is

$$2.56 \pm 0.16\,(\mathrm{stat.}) \pm 0.16\,(\mathrm{syst.})\,\mathrm{SNU}.^2 \tag{2.18}$$

2.4.2 KAMIOKANDE-II/III

Kamioka Nucleon Decay Experiment (KAMIOKANDE) [15] is the neutrino experiment based on water Cherenkov detection. The experiment, a predecessor of Super-Kamiokande, observed the Cherenkov light produced by the recoil electron of the elastic scattering in the pure water of 3,000 tons as described in Eq. 2.19.

$$\nu_\alpha + e \rightarrow \nu_\alpha + e \ (\alpha = e, \mu, \tau) \tag{2.19}$$

The total livetime combined KAMIOKANDE-II and KAMIOKANDE-III is 2079 days. KAMIOKANDE used three different energy thresholds of 9.3 MeV (449 days), 7.5 MeV (794 days) and 7.0 MeV (836 days).

The latest result of the neutrino flux obtained from KAMIOKANDE-II/III [15] is

$$(2.80 \ \pm 0.19\,(\mathrm{stat.}) \pm 0.33\,(\mathrm{syst.})) \ \times 10^6/\mathrm{cm}^2/\mathrm{s}. \tag{2.20}$$

The advantage of the Cherenkov detection is that we can know the direction of the recoil electron close to an incoming direction of the observed neutrino and probe the solar neutrino. On the other hand, the neutrino experiments which use other detections can not have any information for the direction of the solar neutrino. Then, an interaction time of the elastic scattering can be accurately known by the Cherenkov detection.

However, since an energy threshold of the electron for emitting the Cherenkov light is 0.775 MeV in the water, the recoil electron less than the energy threshold can not be measured by the detector. Furthermore, the detection in low energy region close to the energy threshold is difficult to identification of the recoil electron by the elastic scattering because the signals are covered with backgrounds, mainly radon daughters, from the detector and in the water.

[2] SNU: Solar Neutrino Unit. 1 SNU is equal to the neutrino flux per 1 s captured by a target with 10^{36}atoms

2.4.3 SAGE, Gallex/GNO

Soviet-American Gallium Experiment (SAGE) [16] and Gallium Experiment (Gallex)/ Gallium Neutrino Observatory (GNO) experiments [17, 18] are based on the radiochemical detection with gallium (^{71}Ga). The gallium target has the mass of 30∼50 tons (SAGE) and 30 tons (Gallex/GNO). The main observation target of these experiments is pp neutrinos because the energy threshold of the reaction (Eq. 2.21) is 0.233 MeV.

$$\nu_e + {}^{71}\mathrm{Ga} \rightarrow \mathrm{e}^- + {}^{71}\mathrm{Ge} \tag{2.21}$$

The advantage of the radiochemical detection using gallium is that the neutrinos in very low-energy region can be detected. The latest combined result [16] from SAGE and Gallex/GNO is

$$66.1 \pm 3.1\,\mathrm{SNU}. \tag{2.22}$$

2.4.4 Super-Kamiokande

The details of Super-Kamiokande will be discussed later. The Super-Kamiokande is also based on the water Cherenkov detection same as KAMIOKANDE.

2.4.5 SNO

Sudbury Neutrino Observatory (SNO) experiment [19–22] based on heavy water target uses three interactions as follows.

$$\begin{aligned}
\text{Elastic scattering} &: \quad \nu_\alpha + e^- \rightarrow \nu_\alpha + e^- && (2.23)\\
\text{Charged current} &: \quad \nu_e + D \rightarrow e^- + p + p && (2.24)\\
\text{Neutral current} &: \quad \nu_\alpha + D \rightarrow \nu_\alpha + p + n, && (2.25)
\end{aligned}$$

where D, p and n show deuterium, proton and neutron, respectively. The advantage of the heavy water target is that these reactions can be detected by using the same detector. The result of the elastic scattering reaction can be also possible to cross-check the solar neutrino flux measured by other experiments using the elastic scattering reaction such as Super-Kamiokande. Early measurements of the charged current reaction in SNO and the elastic scattering reaction in Super-Kamiokande suggested that the SSM prediction was correct, and gave strong evidence for the solar neutrino oscillation. The latest results of the solar neutrino flux obtained from the neutral current reaction is $(5.25 \pm 0.16(\mathrm{stat.})\ ^{+0.11}_{-0.13}(\mathrm{syst.})) \times 10^6$ /cm^2/s [22] and the charged current reaction is $(1.67\ ^{+0.05}_{-0.04}(\mathrm{stat.})\ ^{+0.07}_{-0.08}(\mathrm{syst.})) \times 10^6$ /cm^2/s [21]. In Chapter 9, we use ^{8}B flux constraint as $(5.25 \pm 0.20(\mathrm{stat.} + \mathrm{syst.})) \times 10^6$ /cm^2/s based on neutral current reaction in SNO.

2.4.6 Borexino

Boron solar neutrino experiment (Borexino) which detects the recoil electron in the energy region from 0.19 MeV to 2.93 MeV is based on scintillation light detection [23]. The detector has 278 tons liquid scintillator. The observation targets of Borexino are mainly ^{7}Be, pp, pep and ^{8}B neutrinos in the pp-chain. The experiment also uses the elastic scattering reaction of the solar

neutrino with the electron in the liquid scintillator. The latest result of ^{7}Be solar neutrino event rate [23] from Borexino is

$$48.3 \pm 1.1\,(\text{stat.})\,^{+0.4}_{-0.7}\,(\text{syst.})\,\text{cpd}/100\,\text{t}.^3 \tag{2.26}$$

2.4.7 KamLAND

Kamioka Liquid Scintillator Anti-Neutrino Detector (KamLAND) is an anti-electron neutrino experiment detecting the neutrinos from reactors with 1 kton of a liquid scintillator as following reaction [24].

$$\bar{\nu}_e + p \rightarrow e^+ + n \tag{2.27}$$

The vertex and the energy for the events are reconstructed by using the timing and charge distributions of scintillation photons detected by the ID PMTs. The energy threshold of this experiment is above 0.9 MeV. Averaged distance from reactors to KamLAND is approximately 180 km. The survival probability of the neutrinos is related to the mass difference and the ratio of distance to neutrino energy as shown in Eq. 2.9. The oscillation parameters of the reactor neutrino can be compared with that of the solar neutrino because the ratio of the mass difference, the oscillation length and the neutrino energy of the reactor neutrino detected by this experiment is similar level to that of the current solar neutrino oscillation region.

2.5 Remaining problems

The presence of the solar neutrino oscillation is confirmed from the observation of the solar neutrinos experiments, but there are some remaining problems. Among them, I will introduce two main problems: spectrum upturn and tension between solar and reactor neutrino experiments in this section.

2.5.1 Spectrum upturn

One of the research targets of Super-Kamiokande is the search for the MSW upturn effect of the neutrino oscillation by using the solar neutrino (^{8}B neutrino). An upturn on the energy dependence of the survival probability is expected by the MSW effect inside the Sun. The survival probability of the electron neutrinos is $\sim$0.3 in the energy region detected by SK (and SNO) based on the neutrino oscillation calculation with the MSW effect in the Sun. On the other hand, the probability in the energy region about 1 MeV or less increases about twice as shown in Fig. 2.7, since the oscillation in vacuum is dominant in this energy region. These behaviors are called "spectrum upturn" which means the survival probability increases as energy is lowered from the energy region observed by SK.

However, the measurements in this energy region are not enough. Now, the MSW effect can be seen by other neutrino experiments, for example, atmospheric neutrino [25]. However, the upturn of the solar neutrino is not yet discovered by the solar neutrino experiments. Since some different shapes of the energy dependence of the survival probability due to non-standard interaction (NSI) as shown in Fig. 2.7 are reported in the paper [26]. The spectrum upturn of the solar neutrino should be verified to understand neutrino physics.

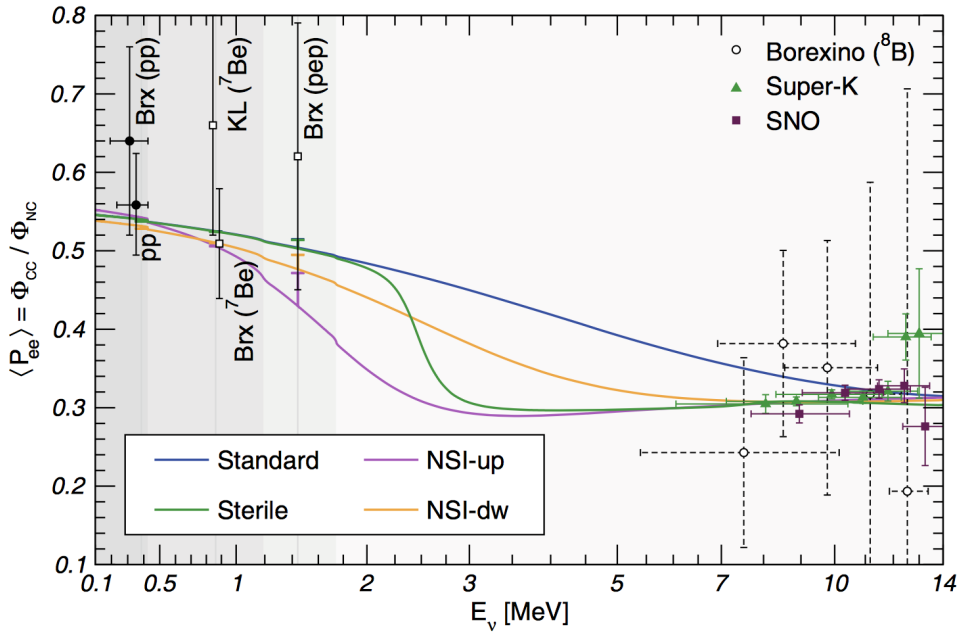

Figure 2.7: Survival probability as a function of the neutrino energy [26].

2.5.2 Tension between solar and reactor neutrino experiments

The second remaining problem of Super-Kamiokande is the evaluation of the possible difference between neutrino and anti-neutrino. In Fig. 2.8, the two-dimensional plot represents as function of Δm^2_{21} and $\sin^2\theta_{12}$. Green contour shows a result of Δm^2_{21} and $\sin^2\theta_{12}$ of the neutrino from all solar neutrino experiments. Blue contour shows the result of the anti-electron neutrino from the reactor neutrino experiment (KamLAND). Red contour shows a combined result from the solar and the reactor neutrino experiments. The tension between the neutrino and the anti-neutrino is close to 2σ on $\Delta\chi^2$ for Δm^2_{21}. If the significant difference is found, it means that the neutrino and the anti-neutrino have a different property each other. It is considered that one of the reasons of the difference would be CPT violation. If CPT symmetry is established, the neutrino and the anti-neutrino should have same oscillation parameters under the standard neutrino oscillation. Therefore, in the case the tension exists, there is a possibility that the phenomenon relates to new physics.

2.6 Motivation of this thesis

I approach by the following items and will discuss the results of the spectrum upturn and the tension of the oscillation parameter in this thesis.

- Increase data statistics by an additional (observation) period of 1.7 times (2860 days in total), from the previous paper [27]
- Improve an estimation method of an absolute energy scale
- Re-estimate systematic uncertainties of SK-IV

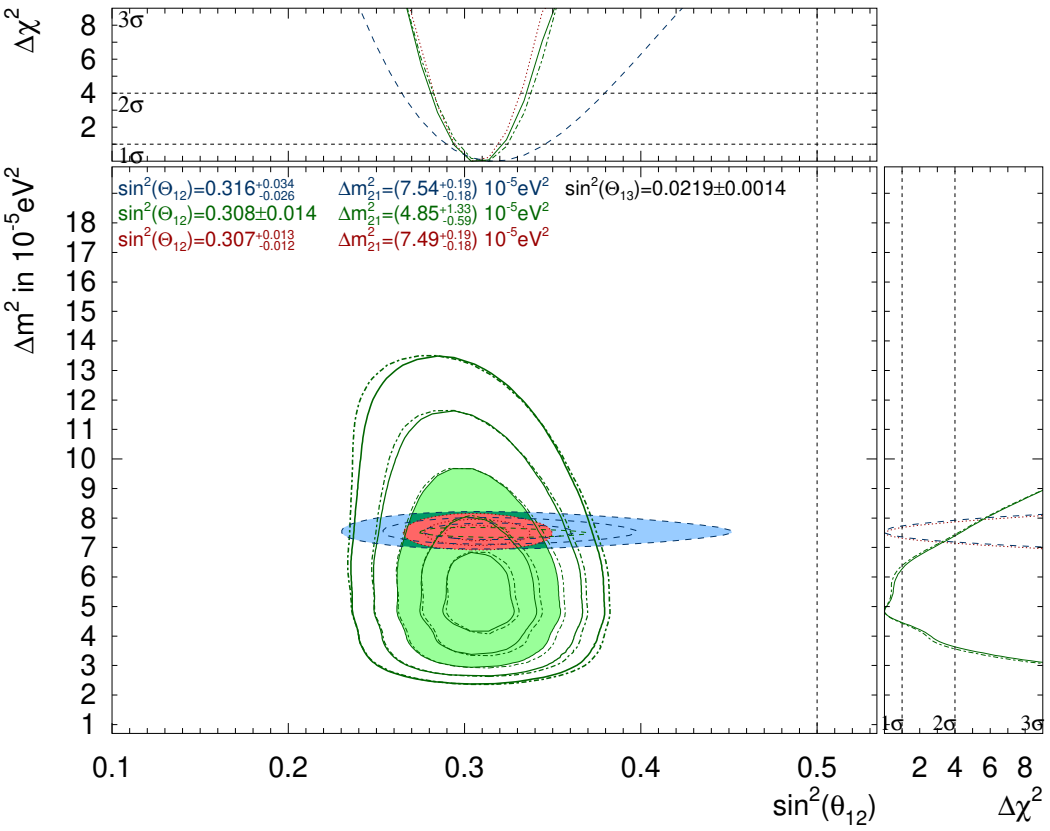

Figure 2.8: Oscillation parameters allowed by the neutrino experiments in the previous results [27]. Blue area shows the KamLAND contour (3σ), green area shows the all solar contour (3σ) and red area shows the results of the combined all solar and KamLAND (3σ). Lines show 1, 2, 3, 4, 5σ C.L. of these oscillation parameters, and dashed line shows the result of the combined SK and SNO.

Chapter 3

Super-Kamiokande detector

Super-Kamiokande (SK) is a neutrino experiment targeting mainly solar neutrinos, atmospheric neutrinos, proton decay, supernova (relic) neutrinos, and accelerator neutrinos. This chapter briefly describes about SK detector, detection principle and event reconstruction related to the solar neutrino analysis. The details are explained in [28].

3.1 Overview of SK detector

Super-Kamiokande detector is located at 2700 meter-water equivalent (m.w.e) mean overburden at geographic coordinate 36'25'32.6"N, 137 18'37.1E, at 1,000 m underground of Mount Ikenoyama, in Gifu Prefecture, Japan. The SK detector is a water Cherenkov detector filled with 50k tons of ultra pure water in a cylindrical stainless-steel tank with a diameter of 39.3 m and a height of 41.4 m in Fig. 3.1.

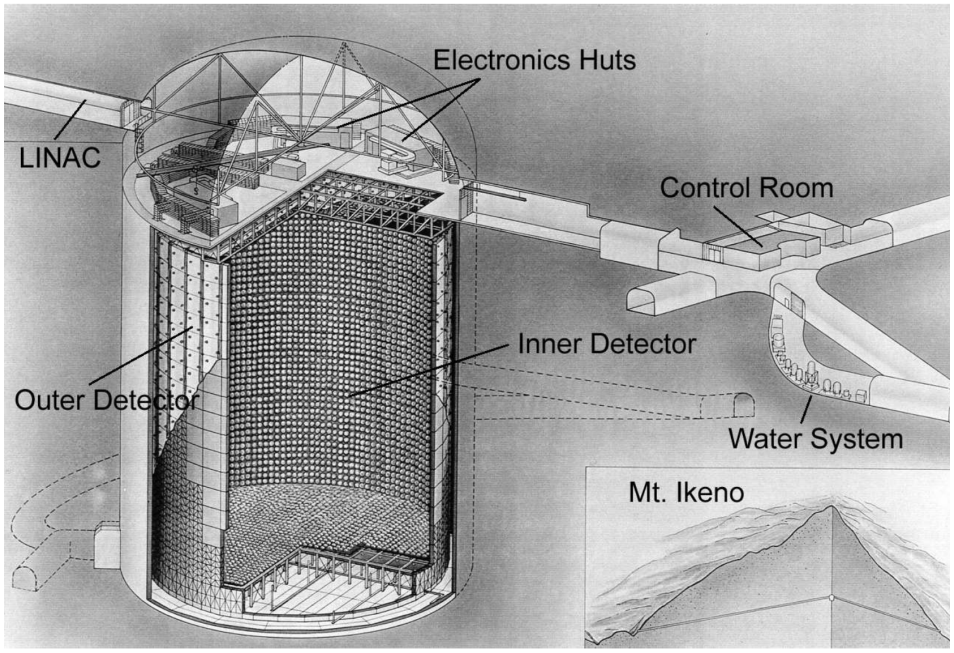

Figure 3.1: Super-Kamiokande (SK) detector [28].

The SK detector has two layer structure of inner detector (ID) containing 11,146 ID PMTs in SK-I, and outer detector (OD) containing 1,885 OD PMTs. ID (OD) PMTs are arrayed on the inward (outward) side of a wall separating these detectors. The ID is a cylindrical structure with a diameter of 33.8 m and a height of 36.2 m filled with 32k tons of the water. The OD, surrounding the ID, contains 18k tons of the water.

The wall can be divided three blocks: top module, bottom module and barrel (side) module. Figure 3.2 shows the modules supporting the ID and the OD. Furthermore, the modules consist of minimum unit of the construction, super module, which contains twelve ID PMTs and two OD PMTs.

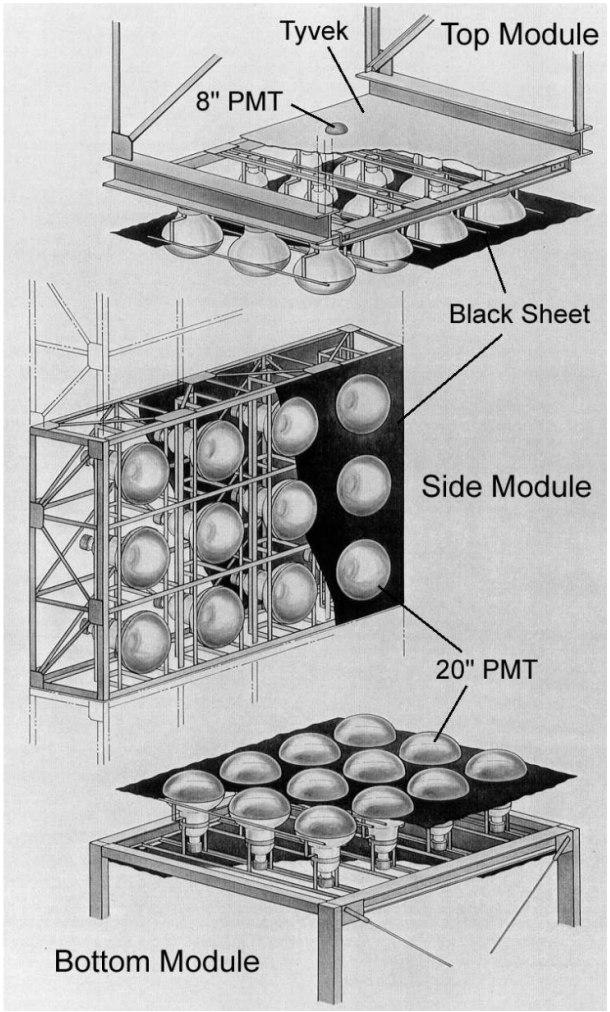

Figure 3.2: Component of the super module: top module (upper), barrel module (middle) and bottom module (lower). Each super module contains twelve ID PMTs and two OD PMTs [28].

The coordinate system of the SK detector is illustrated in the left of Fig. 3.3 [27]. X-axis of the coordinate system is set with phase shift of 220.583 degree against the northward as illustrated in the right of Fig. 3.3 [28]. In the center figure, a solar zenith angle (θ_z) which is the angle of the solar direction (red line) against the X-Y plane of the SK detector when an event occur in the SK detector is illustrated. Then, a zenith angle ($\theta_{z,\mathrm{eve}}$) which is the angle of a reconstruction direction

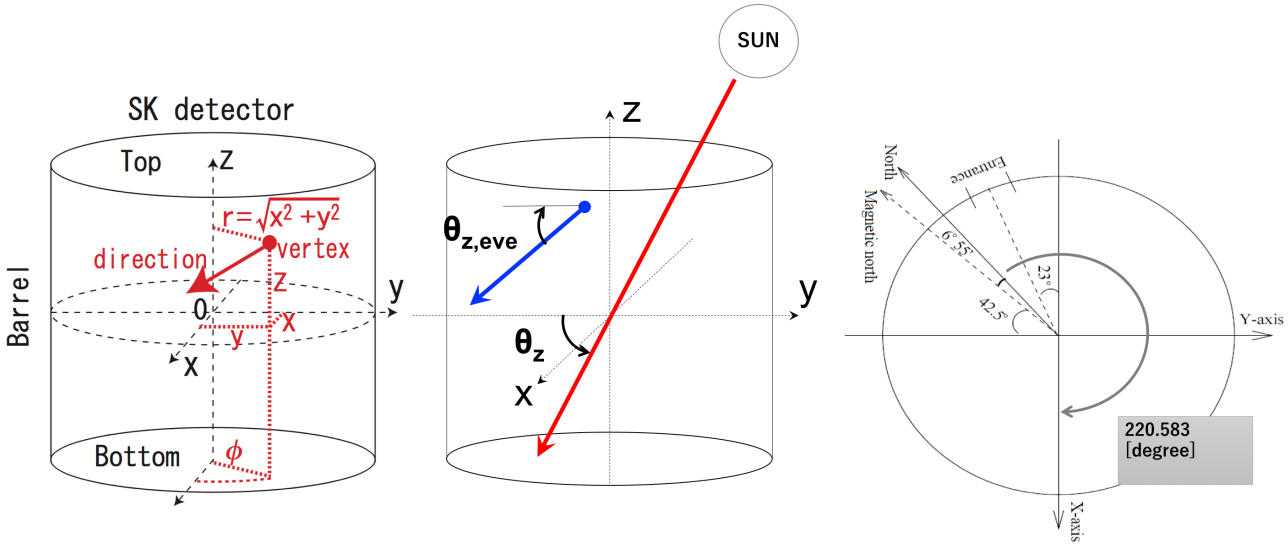

Figure 3.3: Coordinate system of the SK detector (Left: [27], Right: [3]). In the center figure, $\theta_{z,eve}$ shows an angle between the X-Y plane and the solar neutrino events.

(blue line) of an event against the x-y plane is also illustrated.

SK have performed in four phases as shown in Table 3.1. In SK-II, about half of ID PMTs are destroyed by a shock wave accident and the coverage of the SK detector is smaller than that of other phases.

Table 3.1: Experiment phases of SK. A livetime and an energy threshold (electron kinetic energy) described in the table are values used in the solar neutrino analysis.

Phase	SK-I	SK-II	SK-III	SK-IV
Period (Start)	Apr. 1996	Oct. 2002	Jul. 2006	Sep. 2008
Period (End)	Jul. 2001	Oct. 2005	Aug. 2008	May. 2018
Livetime [days]	1496	791	548	2860
ID PMT	11146	5182	11129	11129
OD PMT	1885	1885	1885	1885
PMT coverage [%]	40	19	40	40
Energy threshold [MeV]	4.5	6.5	4.0	3.5

3.1.1 Water and air purification system

Diagram of water flow (only inlet and outlet) in the SK detector (SK-IV) is shown in Fig. 3.4. The water is supplied into the SK detector thorough acrylic pipes from the bottom region of the SK detector and returned to water purification system from the top region. In SK-IV, the water with a flow rate of 60 ton/hour is continuously circulated between the water purification system and the detector. However, a little impurities such as small dusts, bacteria, and radioactivity source are included in the water. The existence of these impurities can be caused the scatter of Cherenkov light.

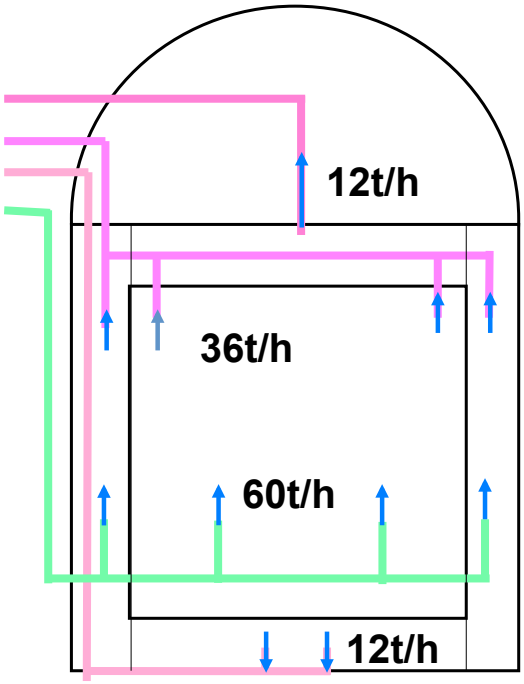

Figure 3.4: Diagram of the water flow of the SK detector in SK-IV shown by the inlet (green) and outlet (purple). The purified water flows from the bottom region of ID. The outlets of the water are installed in the top region of the ID and in both of the top and the bottom region of the OD [29].

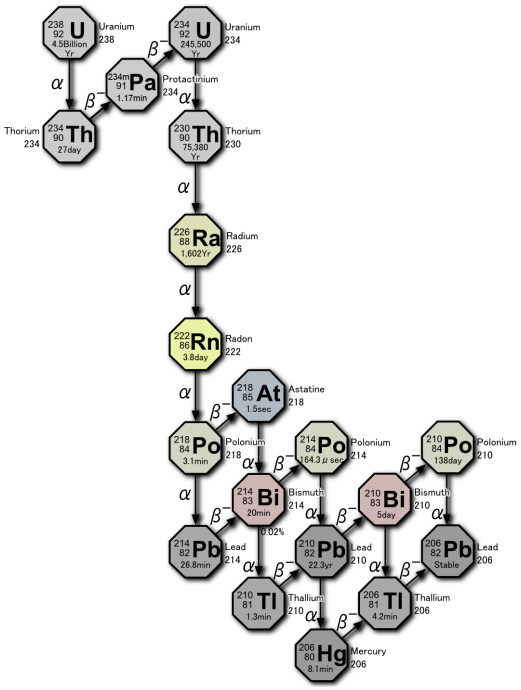

Figure 3.5: Decay chain of uranium series. ^{222}Rn (yellow block) decays to ^{214}Bi and the ^{214}Bi emits electrons through β-decay [30].

Radon(Rn) is a radioactive noble gas element of atomic number 86. It also enters from the structure of the SK detector into the water. ^{222}Rn has a half-life of 3.82 days and successively decays through the decay chain of uranium series as shown in Fig. 3.5. Main background for the solar neutrino analysis is electrons (β-ray) emitted by β-decay of ^{214}Bi in the decay chain. The electron events decayed with Q-value 3.27 MeV dominates the observation of the solar neutrino events in lower energy region. Therefore, reducing radon concentration of the water as much as possible is important for the solar neutrino observation. The output water from the SK detector is cleaned by a water purification system for keeping and improving the detection precision of the SK experiment. The purified water is supplied from the bottom region of the SK detector as shown in Fig. 3.4.

Rn concentration in mine air is higher than that in the outside air because Rn emanated from rock invades into the mine air. Therefore, an air pump supplies fresh air from outside of the mine into the work space. The Rn concentration in the mine air becomes about 200-2500 Bq/m^3 and fluctuates with the seasonal variation as the air flow is changed throughout a year [28].

3.1.2 Inner/outer detector

In the solar neutrino observation, the main purpose of the inner detector (ID) is to detect Cherenkov light emitted from neutrino-electron scattering events. The Cherenkov photons emitted from charged particles traveling in the water are detected by ID PMTs. Information of the amount of charge and hit timing are recorded by front-end electronics to obtain a vertex, a direction and an energy of the event.

The ID PMTs with a diameter of approximately 50 cm (20 inch) in Fig. 3.6 and Fig. 3.7 are installed at intervals of 70.7 cm, and cover approximately 40% on the inside surface of the detector wall. Black sheet shown in Fig. 3.2 made of polyethylene terephthalate covers between the ID PMTs on the inside surface of the module. It suppresses photon reflection and optically separates the detector to the inner and the outer part. A quantum efficiency and a collection efficiency of the ID PMT are about 21% (360 - 400 nm) and 70%, respectively.

The outer detector (OD) is to distinguish between the neutrino events and cosmic-ray muon events. The cosmic-ray muons are background source for observation of the solar neutrino event because the muon causes a spallation in the water. The SK detector locates in underground to guard against the muons, but some muons still remain. Therefore, the muon events are need to be reduced. The muon immediately emits the Cherenkov photons when entering the SK detector as the muon is charged particle. As a result, the Cherenkov photon derived from the muon can be detected by the OD PMTs. On the other hand, the neutrino can not emit the Cherenkov photons until an interaction occurs as neutrino is electrically neutral. In the solar neutrino analysis, we use only the events occurred in the ID. The SK detector distinguishes between the neutrino events and the cosmic-ray muon events by utilizing the respective characteristics.

The OD PMTs with a diameter of approximately 20 cm (8 inch) are installed in the center of the wavelength conversion plate of 60 cm side. White reflection sheet in Fig. 3.2 made of tyvek covers on the outside surface of the wall in order to increase the light collecting efficiency.

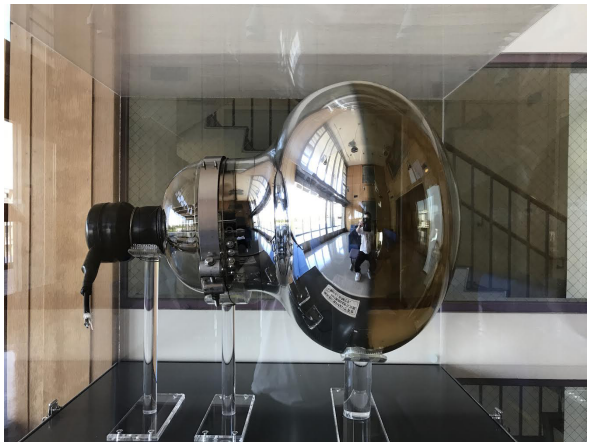

Figure 3.6: 20 inch PMT of the ID displayed on the 3rd floor in Science and Technology Research Building 3, in Rokkodai Campus of Kobe university.

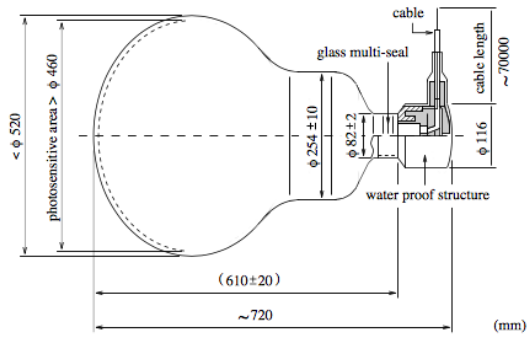

Figure 3.7: Conceptual scheme of 20 inch PMT of the ID [28]

3.1.3 Electronics system

Data acquisition (DAQ) system reads out the signals sent from the ID/OD PMTs. To adjust the arrival timing of the signals due to the different PMT positions, the signal cables are designed as the same length for the ID PMTs. The DAQ system calculates the amount of charge and hit timing information of the detected photons. All hits of each PMT are recorded in the new front-end electronics system from SK-IV [31]. Therefore, a hardware trigger is nothing and only software trigger is applied to reconstructed events for data analysis. Type of the software triggers, the threshold and the trigger rate are shown in Table 3.2. The threshold in the table represents a number of hit ID PMTs which are received photons in the time window of 200 ns. The threshold of the SLE trigger is replaced 34 hits to 31 hits in order to store further more information for the solar neutrino analysis from May of 2015.

Table 3.2: Software triggers related to this analysis of SK-IV. Values of the threshold and the trigger rate in bracket show that by the trigger threshold 31 hits.

Trigger type	Threshold [hits]	Trigger rate [Hz]	Time gate width [μs]
Super Low Energy(SLE)	34 (31)	3.0-3.4 (13.0) k	1.5
Low Energy(LE)	47	40	40
High Energy(HE)	50	10	40
OD trigger	22	-	40

3.2 Event reconstruction

For the solar neutrino analysis, the Cherenkov photons derived from the following elastic scattering reaction are detected.

$$\nu + e^- \rightarrow \nu + e^- \quad (\nu = \nu_e, \nu_\mu, \nu_\tau) \tag{3.1}$$

All flavors of the neutrino-electron elastic scattering are detected by the ID. Low-energy events are selected by using Cherenkov ring pattern. To extract the neutrino events derived from the solar neutrino, a signal extraction method is performed as described in Chapter 7.

The interaction has the small cross section. The recoil electron travels along with a direction close to the neutrino incident direction and emits the Cherenkov photons in the water. The Cherenkov photon has cone-shaped with the Cherenkov angle as described in following equation and hits ID PMTs on the wall.

$$\cos\theta_c = \frac{1}{n\beta} \tag{3.2}$$

n represents a refractive index and $\beta = v_e/c$: c is speed of light ($= 3.0 \times 10^8$ m/s) and v_e is the speed of the recoil electron. An event display of a typical low-energy event is shown in Fig. 3.8. Coloring points in the black area in which the event display represents the ID illustrate hit PMTs. The color difference shows a timing difference of each hit PMT. The solar neutrino analysis reconstructs the vertex, the direction and the energy of the recoil electron by using the timing information, the ring pattern and the number of hit PMTs, respectively. A more detailed explanation for these event reconstructions are given in this section.

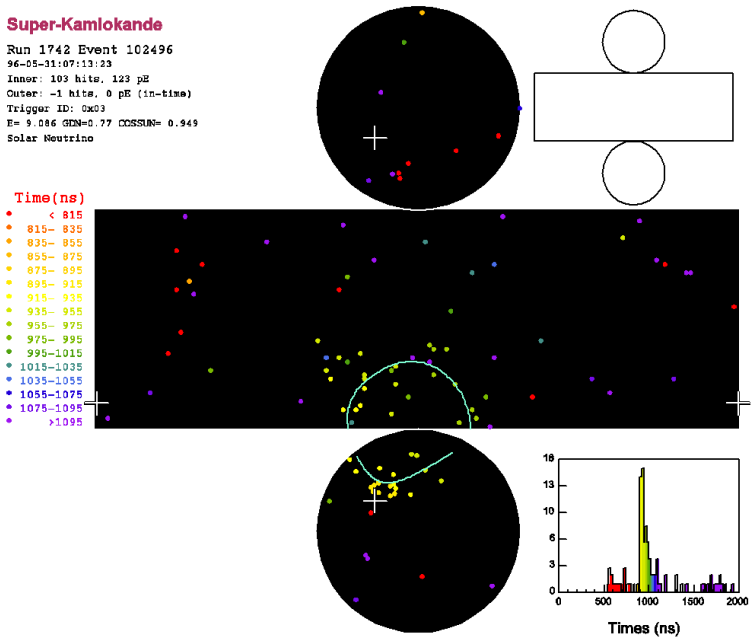

Figure 3.8: Event display of a typical low-energy event

The following event reconstructions and event reconstruction quality parameters are used in both the data analysis and the MC simulation.

3.2.1 Vertex reconstruction

The vertex (position of the interaction) of the neutrino-electron elastic scattering is reconstructed by using timing information (arrival time) when the Cherenkov photon hits to the ID PMT. The travel length of the recoil electron emitting the Cherenkov photon is at most about 5 cm for a 10 MeV electron as shown in Fig. 3.9. On the other hand, the vertex resolution of the SK detector is about 50 cm for a 10 MeV electron as shown in Fig. 3.10. Therefore, the vertex is reconstructed as a punctiform in spite of that the elastic-scattering interaction position and the position emitted Cherenkov photon differ.

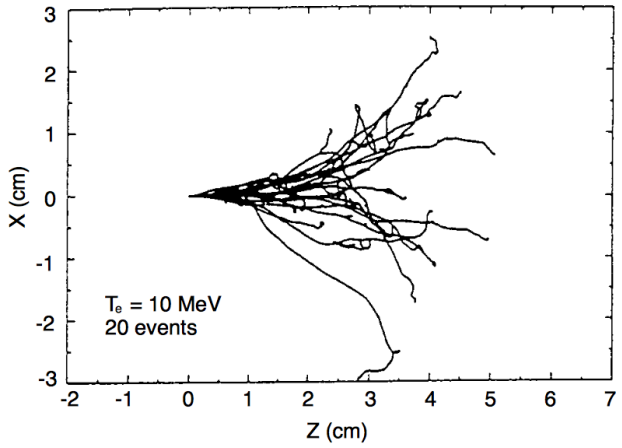

Figure 3.9: The simulated tracks of the recoil electron for 10 MeV electrons estimated by a Monte Carlo simulation. The number of the generated events is 20 events. The maximum length of the recoil electron is about 5 cm [32].

The vertex reconstruction is a maximum likelihood fit based on relative PMT hit timing of Cherenkov light, as follows:

$$\mathcal{L}(\vec{r}, t_0) = \log \prod_{i=1}^{N_{\rm hit}} pdf(\Delta t_i(\vec{r})), \tag{3.3}$$

$$\Delta t_i(\vec{r}) = t_i - tof_i(\vec{r}) - t_0, \tag{3.4}$$

$$t_{{\rm res},i} = t_i - tof_i(\vec{r}) = t_i - \frac{n}{c}\sqrt{(x-x_i)^2 + (y-y_i)^2 + (z-z_i)^2}. \tag{3.5}$$

where $\mathcal{L}(\vec{r}, t_0)$ is a likelihood function of the vector from the interaction vertex to the hit PMT and the time of the interaction (t_0). $N_{\rm hit}$ is the number of hits in an event within 1.3 μs and index of i represents i-th hit PMT receiving the Cherenkov photons on a photoelectric surface of the PMT. $pdf(\Delta t_i(\vec{r}))$ is a probability density function of $\Delta t_i(\vec{r})$. t_i is the arrival time when the PMT receives the Cherenkov photons. The tof_i is a time of flight of the Cherenkov photon from the vertex position to the i-th hit PMT as defined in Eq. 3.5. $t_{{\rm res},i}$ is a residual time of the i-th hit PMT. The residual time is a remained time after subtracting the time of flight of the photon from the arrival time t_i. The variables (x_i, y_i, z_i) represent the coordinates of the i-th hit PMT position as defined in Fig. 3.3. The constant n is the refractive index of water and c is the speed of light in vacuum. t_0 is an average time of the fitted peak time of $t_{{\rm res},i}(\vec{r})$ distribution.

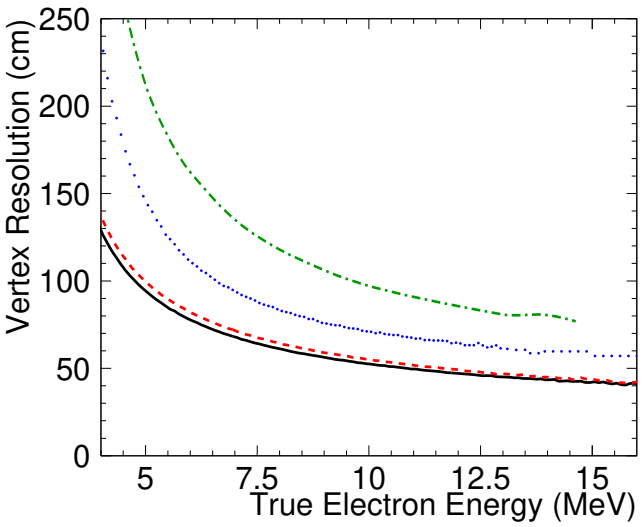

Figure 3.10: Vertex resolution for each SK-phase. The dotted (blue), the dashed-dotted (green), dashed (red), and the solid (black) lines represent for SK-I, II, III, and IV, respectively. The vertex resolution of SK-III (and SK-IV) is improved against SK-I because of the improvement of the vertex reconstruction method [27].

The likelihood function is estimated by the LINAC calibration as shown in Fig. 3.11. The peak of the residual time fit to be maximized the likelihood for each vertex.

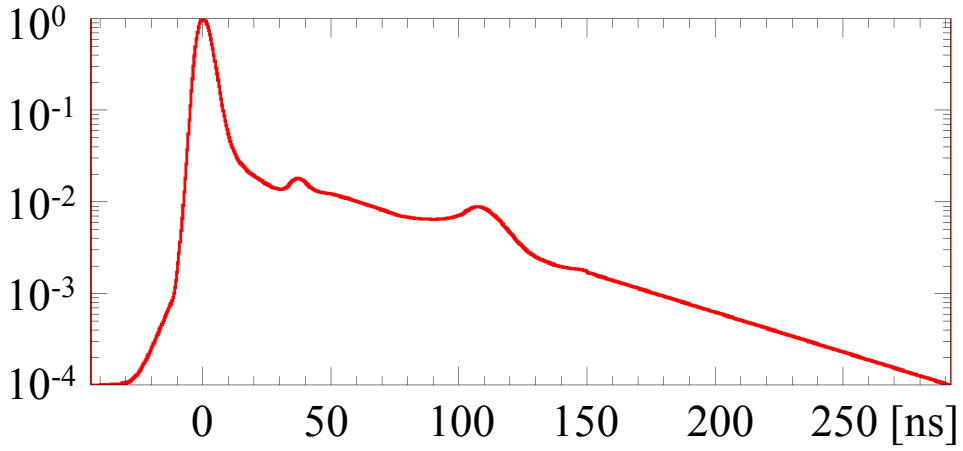

Figure 3.11: Likelihood function for the vertex reconstruction. Two peaks around 35 ns and 110 ns are due to an after pulse of PMT.

3.2.2 Direction reconstruction

The travel direction of charged particle including the recoil electron and any background is reconstructed by ID PMT hit pattern and the reconstructed vertex above. The direction is found by a maximum likelihood by comparing data and Monte Carlo simulation of the Cherenkov ring pattern.

$$\mathcal{L}(\vec{d}) = \sum_{i=1}^{N_{20}} \log(f(E_e, \cos\theta_i))_i \times \frac{\cos\theta_i}{a(\cos\theta_i)} \times Q_i \tag{3.6}$$

Index of i represents i-th hit PMT. N_{20} is a number of hit PMTs within 20 ns time window, Q_i is an amount of charge of individual i-th PMT and θ_i is an incident angle of photon on the surface of i-th hit PMT as illustrated in the left of Fig. 3.14. The function $f(E_e, \cos\theta_i)$ is a likelihood function of the hit pattern shown in Fig. 3.12. $a(\cos\theta_i)$ is a correction factor of a PMT acceptance related to the incident angle at each PMT. The efficiency of the perpendicular direction is bigger than that of the other direction. The correction function is estimated by Ni calibration defined as the following equation shown as Fig. 3.13.

$$a(\cos\theta_{\rm i}) = 0.205 + 0.524\cos\theta_i + 0.390\cos^2\theta_i - 0.132\cos^3\theta_i \tag{3.7}$$

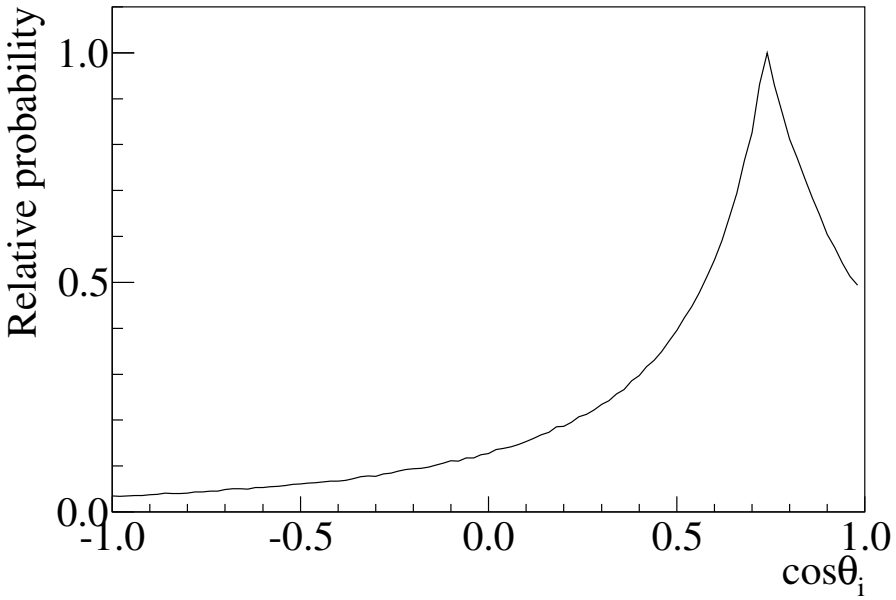

Figure 3.12: Likelihood function for the reconstructed direction of $E_e = 10$ MeV recoil electrons.

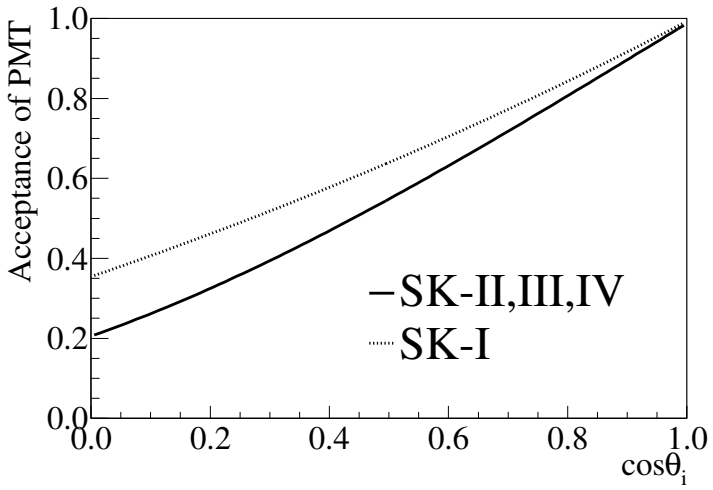

Figure 3.13: Correction factor of a PMT acceptance, $a(\cos\theta_{\rm i})$, related to the incident angle. The acceptance since SK-II gets worse due to an acrylic cover installed to the PMTs in the inner detector to protect from shock wave.

3.2.3 Energy reconstruction

The energy of a recoil electron from the neutrino-electron scattering interaction is reconstructed by the number of hit PMTs. In general, an amount of charge of photoelectron is used for the energy calculation of the photons hitting PMT, but it is not many that the number of photons to reconstruct the energy of the recoil electron by the solar neutrino event. Therefore, the number of hit PMTs within a 50 ns time window (N_{50}) are counted and corrected by several correction parameters, an effective number of hits ($N_{\rm eff}$), as following,

$$N_{\rm eff} = \sum_{i=1}^{N_{50}} \left[(X_i - \epsilon_{\rm dark} + \epsilon_{\rm tail}) \times \frac{N_{\rm total}}{N_{\rm alive}} \times \frac{1}{S(\theta_i, \phi_i)} \times \exp\left(\frac{r_i}{L}\right) \times \frac{1}{QE_i} \right] \tag{3.8}$$

The effective number of hits is calculated when the reconstructed vertex is inside of an inner volume, $r^2 \leq 1690$ cm and $|z| \leq 1810$ cm.

- X_i : Occupancy correction for multiple photon hits

  Most of hit PMTs receive one photo electron basically. However, if the reconstructed vertex of an event is close to the end of the inner volume and the reconstructed direction faces to the wall closest the vertex, the Cherenkov light can not form a conical shape well before reaching the wall/PMTs. In the case of that many Cherenkov photons concentrate to one PMT, the others around the PMT don't receive the photons well. The expected number of the photons hitting to i-th PMT is estimated by the occupancy in the eight PMTs surrounding the i-th PMT. Using the total number of alive PMTs surrounding i-th PMT and itself (N_i=1$\sim$ 9) and the number of hit PMTs in the alive PMTs (n_i), the occupancy correction can be estimated as following.

$$X_i = \begin{cases} \frac{\log(1-\alpha_i)^{-1}}{\alpha_i} & (\alpha_i < 1) \\ 3.0 & (\alpha_i = 1) \end{cases}$$

where $\alpha_i = n_i/N_i$.

- $\epsilon_{\rm dark}$: Dark rate correction factor

$$\epsilon_{\rm dark} = \frac{N_{\rm alive} \times R_{\rm dark} \times 50\,{\rm ns}}{N_{50}} \tag{3.9}$$

$N_{\rm alive}$ is the number of the alive PMTs. $R_{\rm dark}$ is an averaged rate of dark noise (dark rate) of each run. N_{50} is the number of hit PMTs within 50 ns time window. Therefore, this dark rate correction factor represents the expected ratio of the dark noise against the signal within 50 ns time window for each event.

- $\epsilon_{\rm tail}$: Correction factor for a tail of the arrival time
Since the arrival time of photon at hit PMT leaves a trail behind the time window of 50 ns, the effect is corrected by utilizing the number of hit PMTs within the time window of 100 ns.

$$\epsilon_{\rm tail} = \frac{(N_{100} - N_{50}) - \{N_{\rm alive} \times R_{\rm dark} \times (100\,{\rm ns} - 50\,{\rm ns})\}}{N_{50}} \tag{3.10}$$

N_{100} is the number of hit PMTs within 100 ns time window. Braces in the formula represent that the expected number of the dark noise included in the tail part.

- $\dfrac{N_{\rm total}}{N_{\rm alive}}$: Bad channel correction factor
This factor is a correction factor for an unstable or dead PMT channels. $N_{\rm alive} = N_{\rm total} - N_{\rm bad}$. $N_{\rm total}$ is the total number of the ID PMTs (=11,146). $N_{\rm bad}$ is a number of bad ID PMTs.

- $\dfrac{1}{S(\theta_i, \phi_i)}$: Coverage factor for photoelectric surface
$S(\theta_i, \phi_i)$ is the effective area of the photoelectric surface when viewing the i-th hit PMT from θ_i, ϕ_i direction (incident direction of photons) illustrated in the left of Fig. 3.14. When θ_i is large, an asymmetry of the sensitivity in the ϕ_i direction occurs due to the influence of a shadow of the surrounding PMTs as shown in the right of Fig. 3.14.

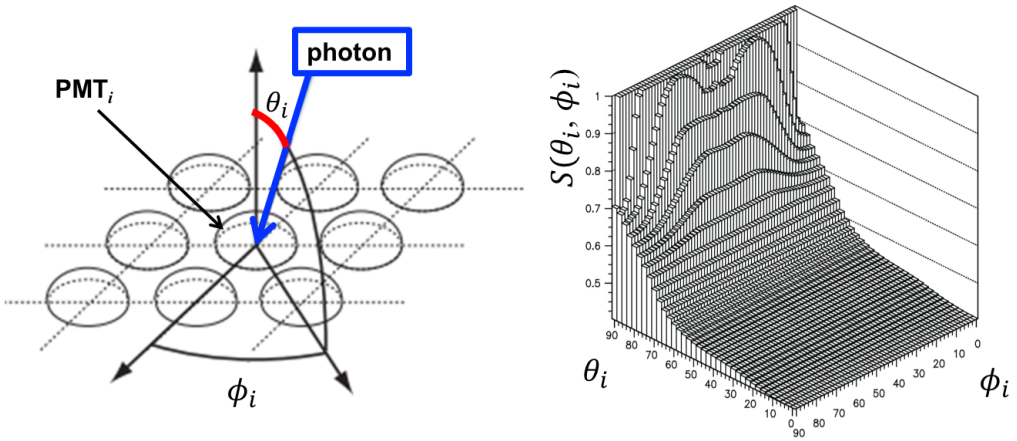

Figure 3.14: Left figure shows a definition of θ_i and ϕ_i [33]. $\theta_i = 0$ when direction in normal to the wall. Right figure shows a definition of $S(\theta_i, \phi_i)$ [34].

- $\exp\left(\frac{r_i}{L}\right)$: Correction by water transparency
  Water transparency denotes the total attenuation length (L[m]) of the water varies from day to day. A more detailed explanation of the water transparency is given later in Section 4.1.1. r_i is a distance from the reconstructed vertex to the i-th hit PMT. For example, if the distance is longer against the water transparency, the effective number of hits is estimated more as the photons are difficult to reach the PMTs.

- $\frac{1}{QE_i}$: Correction by quantum efficiency
  This factor is for correcting the difference of quantum efficiency of each ID PMT.

In this analysis, these factors are also corrected the time variation of PMT gain and dark rate as described in Section 5.2.1. The effective number of hits is converted to total energy of recoil electron by using an empirical model based on the Monte Carlo simulation. The relational expression of them is represented by 4th order polynomial function shown in Fig. 3.15.

$$E_e = \sum_{i=0}^{4} c_i \left(N_{\text{eff}}\right)^i \qquad (N_{\text{eff}} < 248.1) \tag{3.11}$$

$$E_e = \sum_{i=0}^{4} c_i \left(248.1\right)^i + 0.140(N_{\text{eff}} - 248.1) \quad (N_{\text{eff}} \geq 248.1) \tag{3.12}$$

These coefficients are c_0 = 0.966, c_1 = 0.121, c_2 = 8.50×10^{-6}, c_3 = 3.17×10^{-7}, c_4 = -8.57 ×10^{-10}, respectively.

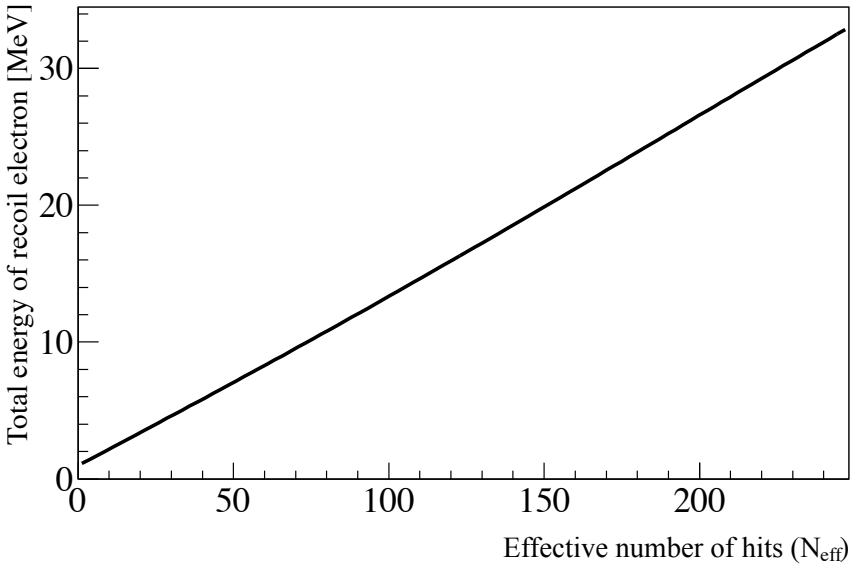

Figure 3.15: The total energy of the recoil electron vs. the effective number of hits.

3.3 Event reconstruction quality

The accuracy of the event reconstruction is evaluated by using some quality parameters. The quality parameters mentioned in this section are applied in the solar neutrino analysis as described in Chapter 6.

3.3.1 Vertex and direction reconstruction goodness

Quality of the reconstructed vertex and direction in the event reconstruction are evaluated using two dimensionless parameters : vertex goodness and direction goodness, respectively. They are calculated in the event reconstruction in Section 3.2, but an event reduction by these parameters is applied to the solar neutrino analysis as described in Chapter 6.

The vertex reconstruction goodness g_V is represented to

$$g_V = \frac{\sum e^{-\frac{1}{2}\left(\frac{\Delta t_i(\vec{r})}{\omega}\right)^2} e^{-\frac{1}{2}\left(\frac{\Delta t_i(\vec{r})}{\sigma}\right)^2}}{\sum e^{-\frac{1}{2}\left(\frac{\Delta t_i(\vec{r})}{\omega}\right)^2}}, \tag{3.13}$$

where $\omega = 60$ ns is PMT timing resolution, $\sigma = 3$ ns is the including the selected hit PMTs, and $\Delta t_i(\vec{r}) = t_i - tof_i(\vec{r}) - t_0$ of the i-th hit PMT. $\vec{r}$ represents a vector from the reconstructed vertex to the hit PMT.

The direction reconstruction goodness g_A is defined as

$$g_A = \frac{1}{2\pi}\left[max\left(\phi_i - \frac{2\pi i}{N}\right) - min\left(\phi_i - \frac{2\pi i}{N}\right)\right], \tag{3.14}$$

where ϕ_i is the azimuthal angle of the i-th hit PMT in the left of Fig. 3.14. The max (min) is represented the deviation for all i.

Both of the two parameters have a range from 0.0 to 1.0. If the vertex reconstruction goodness is $g_V = 1.0$ or if the direction reconstruction goodness $g_A = 0.0$ is better for the reconstruction.

3.3.2 Parameters for external event cut

External gamma-ray from the rock out of the SK detector and the structure of the detectors is one of the background sources in the low-energy region. Therefore, the external event cut is applied by using four parameters, $d_{\rm eff}$, $(P_{\rm wx}, P_{\rm wy}, P_{\rm wz})$, $f_{\rm wall}$, and $\theta_{\rm PMT}$ in the solar neutrino analysis as mentioned in Chapter 6. The parameters are defined as follows and illustrated in Fig. 3.16

- $d_{\rm eff}$: Distance between the reconstructed vertex and the wall along with the opposite reconstructed direction of the recoil electron
- $(P_{\rm wx}, P_{\rm wy}, P_{\rm wz})$: Position on the wall crossing with the parameter $d_{\rm eff}$
- $f_{\rm wall}$: Distance between the reconstructed vertex and the wall along with the reconstructed direction of the recoil electron
- $\theta_{{\rm PMT},i}$: Angle between the reconstructed direction of the recoil electron and the direction from the reconstructed vertex to i-th hit PMT
- $d_{\rm wall}$: Distance from the reconstructed vertex to the ID surface closest to the event

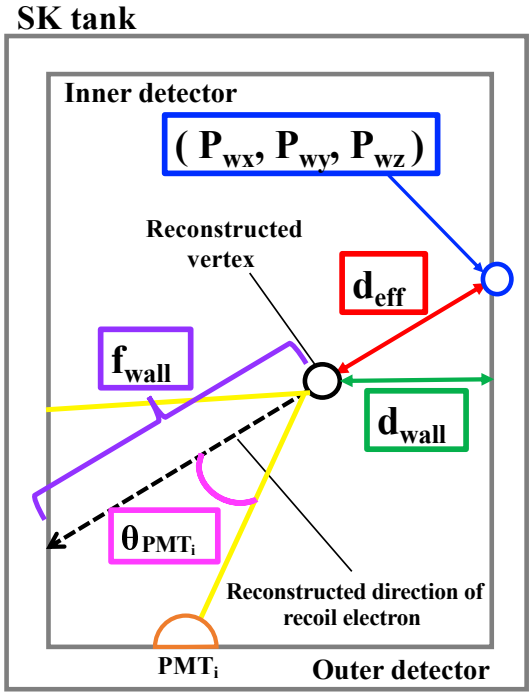

Figure 3.16: Definition of parameters for gamma-ray cut

3.3.3 Multiple scattering goodness

The recoil electrons are affected by multiple coulomb scattering from nucleus and electron in the water. The multiple scattering goodness (MSG), giving a number of the parameter from 0.0 to 1.0, is used for separating solar neutrino signal and their background. The process flow is explained by using Fig. 3.17.

1. Select all combination of the pairs of hit PMTs within 20 ns time window.

2. For pairs of PMTs with two intersection points, the direction from the reconstructed vertex to each of the intersection points is taken as an "event direction".

3. Clusters of the event directions are found by forming vector sums (black arrow in the lower figure) of the event directions (colored arrows in the lower figure) which are within ∼50° of a central event direction (red arrow in the upper figure).

4. Each time an event direction is used in the vector sum it is marked as "passive", and is skipped as the seed for further sums, meaning it will not be the central direction of a ∼50° cluster.

5. Further iterations use the direction of the vector sums to seed new clusters, serving to center the clusters and maximize the sums

6. After a few iterations and maximizing the vector sums, the vector sum with the largest magnitude is kept as a best-fit direction

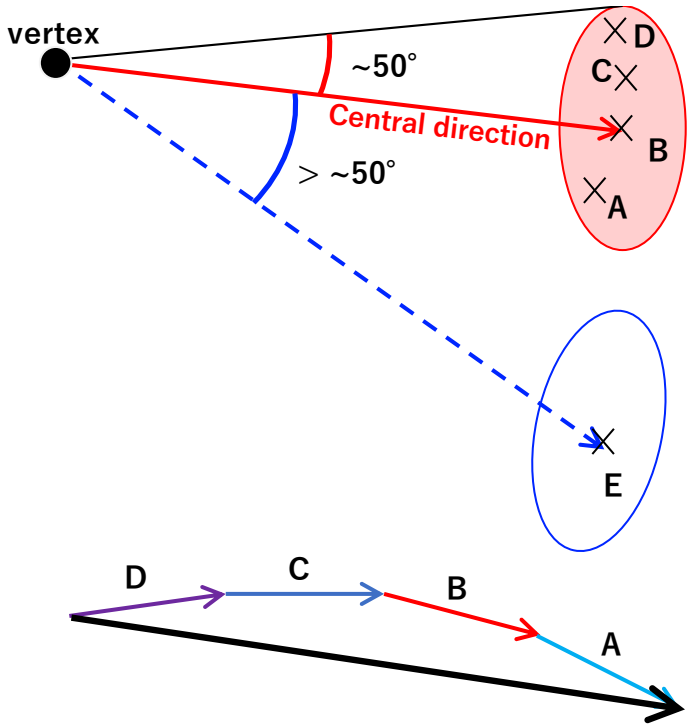

Figure 3.17: Diagram for the calculation of MSG. The cluster in red circle is seeded by direction B, all event directions contained in the cluster are within ∼50° of this direction. Direction E is not a member of the cluster because it is more than ∼50° from the central direction. The cross marks show the intersection of a radius within 42° from hit PMTs.

7. The length of the best-fit direction is correspond to the amount of the MSG (g_{MS}).

The low-energy recoil electrons are induced more multiple scattering and the unit vectors point along with different directions. Then, the length of the best-fit direction, the value of the MSG, becomes a short length. On the other hand, the high-energy recoil electrons scatter less frequently, then the direction of these unit vectors consistent each other and the MSG is higher. If the low energy electrons derived from ^{214}Bi decay and gamma ray are reconstructed, the electrons are affected more multiple scattering and the MSG becomes the low value. In other words, the events which have the same reconstructed energy have the same number of the event directions. Therefore, the magnitude of the MSG corresponds to that of true value of the events, and events away from the true value are removed by using the MSG.

Chapter 4

Monte Carlo simulation

Monte Carlo (MC) simulation reproduces physics events generated in the SK detector. We evaluate the detector performance by the results obtained from the MC simulation. The MC simulation can generate signal events, for example neutrino-electron elastic scattering, then estimate signal probability function as described in Section 7.3. However, the MC simulation can not reproduce background events such as gamma rays and Rn radioactivity source as mentioned in Section 3.1.1. The MC simulation reproduces from the generation of the neutrino event to the information stored to the storage disk. Accordingly, the MC simulated events are also applied the event reconstruction similar to the data analysis described in Section 3.2. The MC simulation based on GEANT3 package [35] is customized for the neutrino analysis in the SK experiment: calibration, response of the SK detector, measured values obtained from other experiments. In this section, the physics parameter generated by the MC simulation related to the solar neutrino events and the evaluation method (calibration) for the detector performance are described.

4.1 Initial setting for the MC simulation

First of all, an initial setting for the MC simulation is done for setting the kinematics of all tracks and the geometry of the SK detector. A list for parameters that change every experimental runs for the MC simulation are read in the initial setting. Physical principle does not basically change for a long time, but the SK detector conditions vary moment by moment due to instability of the SK detector and so on. Since the constantly changing parameters can not be calculated and reflected to the MC simulation, some parameters are calculated in a one-day unit by using actual data. Therefore, the MC generated event is simulated while referring to the parameters.

The following items are the input parameters in the list:

- Seed for random number for generation of the interaction
- Number of the MC generated events
- Corresponding run number
- Quantum efficiency of ID PMTs of SK-IV
- Absolute energy scale correction factor of SK-IV
- Averaged water transparency of the run

- Top bottom asymmetry of the water transparency of the run
- Dark rate of the run
- PMT gain correction of the run

In these parameters, the water transparency, the top-bottom asymmetry, the dark rate and PMT gain correction are estimated by using the real data calculated in a one-day unit. The other parameters use the setting value of each SK phase. The water transparency and the top-bottom asymmetry are explained in the following (sub)sections in detail. The absolute energy scale correction factor corresponds to a collection factor that a photo electron is led to first-dynode of PMT, and is overall normalization factor applied each SK phase. The correction factor is estimated by LINAC calibration for the solar neutrino analysis as will be described in Section 5.3.4. The gain correction is a factor for taking into account of gain increase of ID PMTs as will be explained in Section 5.2.

4.1.1 Water transparency

Water transparency means total attenuation length of the Cherenkov photon by impurities in the water. Intensity of Cherenkov light attenuates exponentially in the water as following formula.

$$I(x) = I_0 \exp\left\{-\frac{x}{L(\lambda)}\right\} \tag{4.1}$$

I_0 is an initial light intensity. $L(\lambda)$ is the water transparency whose time variation is shown in Fig. 4.1.

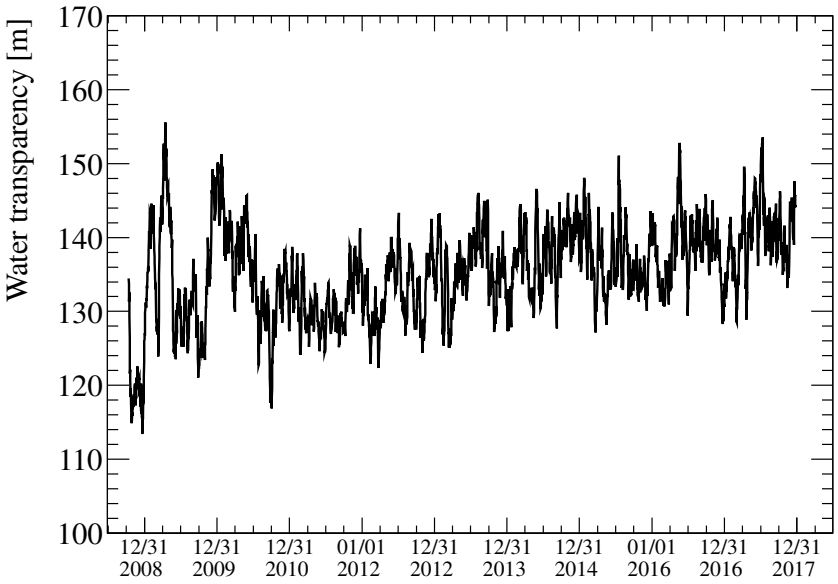

Figure 4.1: Time variation of the water transparency

The water transparency as a function of the wavelength(λ[m]) of the Cherenkov light and is calculated as shown in Eq. 4.2. Then, the water transparency consists of three scattering coefficients related to the wavelength of the light: absorption coefficient (α_{Abs} [1/m]), symmetric coefficient (α_{Sym} [1/m]), and asymmetric coefficient (α_{Asym} [1/m]) as shown in Fig. 4.2.

$$L(\lambda) = \frac{1}{\alpha_{\mathrm{Abs}} + \alpha_{\mathrm{Sym}} + \alpha_{\mathrm{Asym}}} \tag{4.2}$$

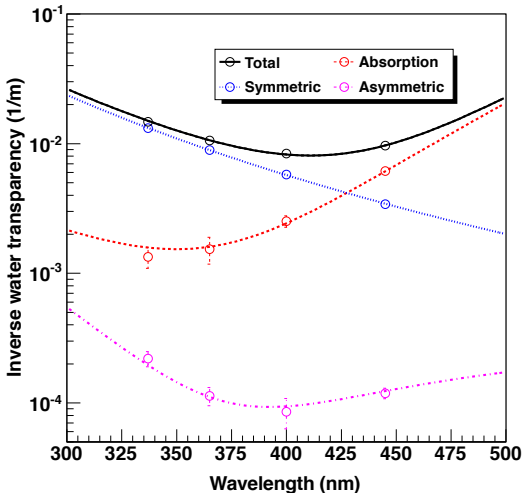

Figure 4.2: Water coefficient function of wavelength of the Cherenkov light. [29].

These parameters are calculated by the data obtained using laser beam [29] and decay electrons, as described below.

Among the cosmic-ray muons which entering into the SK detector, there are muons which decay instead of passing through in the water (stopping muon). The reaction of the muon decay is represented by following equations.

$$\mu^- \rightarrow e^- + \bar{\nu}_e + \nu_\mu \tag{4.3}$$
$$\mu^+ \rightarrow e^+ + \nu_e + \bar{\nu}_\mu \tag{4.4}$$

The energy spectrum of the decay electron has approximately 53 MeV at maximum due to three-body decay of the muons. The electron generated by these reactions is called a decay electron. Using the decay electron, the water transparency is calculated and an energy scale stability are checked. The method to estimate the water transparency from the decay electron event is explained below. The decay electron event observed by the SK detector has a distribution of the effective number of hits as shown in Fig. 4.3. The average value of the distribution of the effective number of hits is used to estimate the energy scale as will be described in Section 5.2.2.

Next, an occupancy ($\overline{q}$(r)) is estimated from the number of the hit and an amount of charge of ID PMTs as shown in Fig. 4.4. The occupancy is calculated by using Eq. 4.5.

$$\overline{q}(r) = \frac{Q_{de}}{N_{\mathrm{eff}}}(r) \tag{4.5}$$

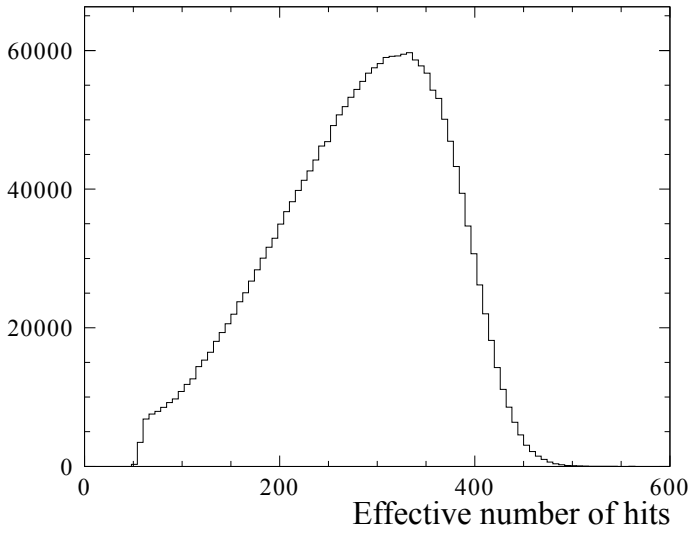

Figure 4.3: The typical distribution of the effective number of hits of the decay electron

Q_{de} is a total amount of the charge of the decay electron, and $N_{\rm eff}$ is the total effective number of hits. The occupancy can be estimated to take the logarithm of the obtained value, and it corresponds to the vertical axis in Fig. 4.4. The distance between the reconstructed vertex of decay electron event and the hit PMT is also calculated for every hit PMT. The distribution of the occupancy is fitted by a linear function in the range from 1200 cm to 3500 cm. In this analysis, a free Y-interception is used in order to estimate the energy scale. The inverse number of the slope of the fitting function corresponds with the water transparency.

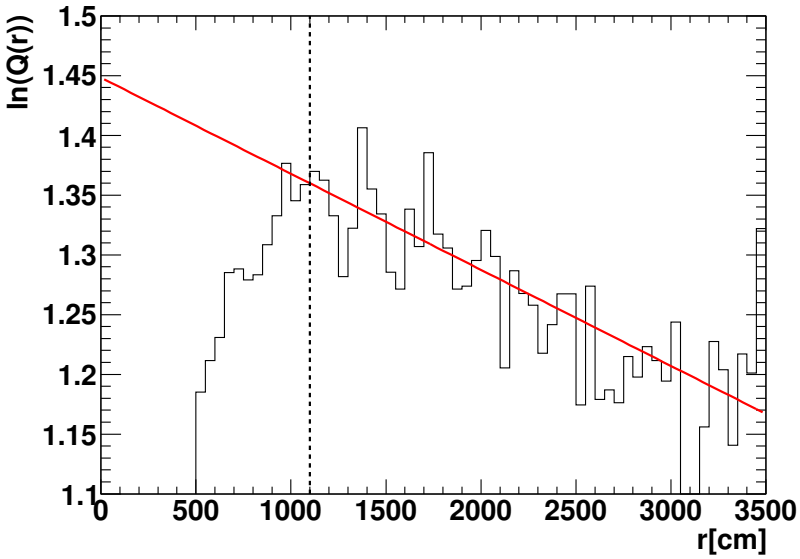

Figure 4.4: The vertical axis corresponds to the occupancy and the horizontal axis is distance between vertex of the decay electron event and the hit PMTs. Red line is the free Y-interception and the dotted line shows the fitting range from 1200 cm to 3500 cm.

4.1.2 Top-bottom asymmetry

Top-bottom asymmetry (TBA) is z-dependence of the water transparency in the SK coordinate system. The water with the low temperature flows into the SK detector from the bottom region and also convects in the region. The water is warmed and risen to the top region and we assumed water quality became worse as the water rises. Figure 4.5 shows the water temperature as a function of z-coordinate. Actually, the temperature is constant due to the convection in $z <$ -1100 cm.

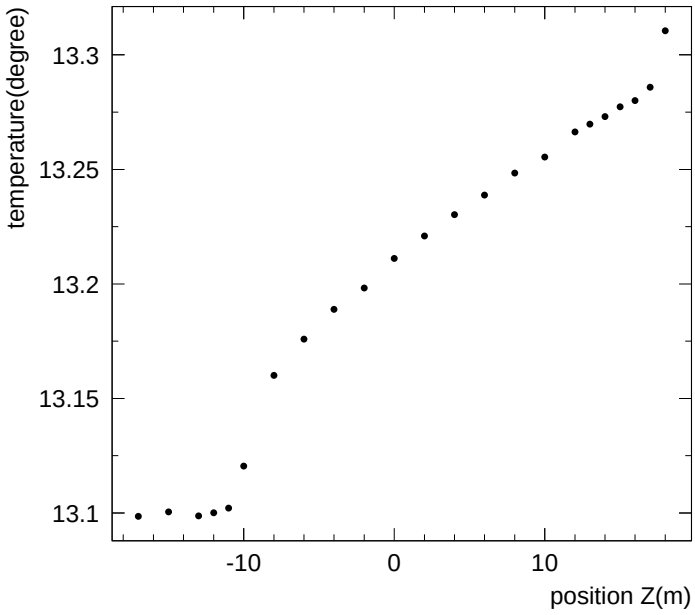

Figure 4.5: Transition of the water temperature in the SK detector [29].

Therefore, we think the water transparency in the bottom region of the SK detector is higher than that of the top region.

The TBA is estimated assuming a constant for $z <$ -1100 cm because the convection exists in the bottom region as shown Fig. 4.5. The TBA is measured and modeled by a Ni-Cf calibration every months as shown in Fig. 4.6. The Ni-Cf calibration is explained briefly as follows and its details are described in [29]. Neutron is emitted from ^{252}Cf at a center in a calibration ball, then γ-ray is emitted from the neutron captured by the Ni source around the Cf source is used for the Ni-Cf calibration. The γ-ray has the energy up to 9 MeV. The water transparency is corrected by including the TBA to α_{Abs} of Eq. 4.2 as follows:

$$\alpha_{\mathrm{Abs}} = \begin{cases} \alpha_{\mathrm{Abs}} \times (1.0 + \beta_{\mathrm{TBA}} z) & (z \geq -1100 \text{ cm}) \\ \alpha_{\mathrm{Abs}} \times (1.0 - 1100\beta_{\mathrm{TBA}}) & (z < -1100 \text{ cm}), \end{cases}$$

where the parameter β_{TBA} shows the value corresponding the TBA estimated by the Ni-Cf calibration. The Ni-Cf calibration is also used for estimating various parameters for SK such as a relative quantum efficiency of PMT, a trigger efficiency and a vertex shift [29].

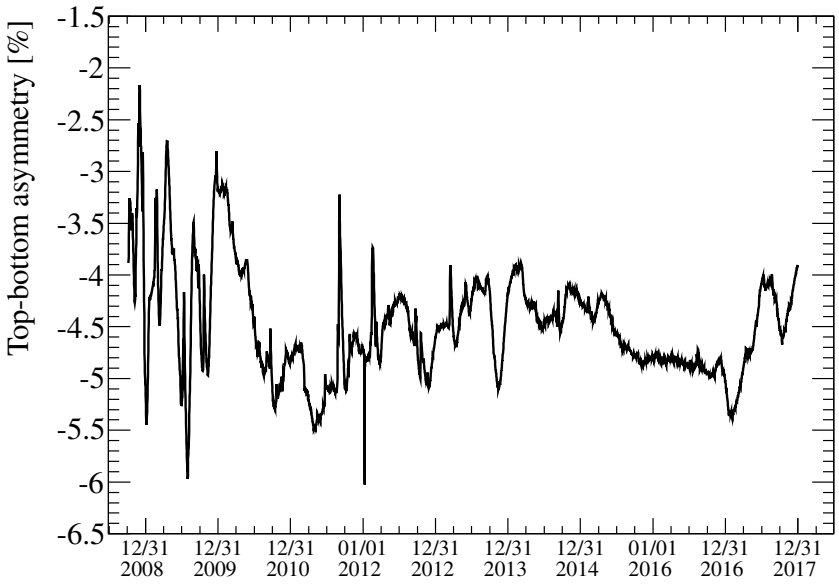

Figure 4.6: Time variation of the top-bottom asymmetry.

4.2 Procedure of generation for the solar neutrino events

In this section, a procedure of the MC simulation for the solar neutrino events is described. Using the MC simulation, we simulate from the generation of the neutrino event to information saved to the storage disk. An event is generated in the following procedure:

1. Generation of particle interaction
2. Tracking of Cherenkov photon
3. Absorption and reflection for the Cherenkov photon by the detector material
4. Response of the SK detector

The MC simulation procedures are performed event by event.

4.2.1 Generation of particle interaction

First of all, ^{8}B solar neutrino event are generated based on Winter spectrum [36] in the MC simulation. Neutrino-electron elastic scattering events coming from the solar direction are generated randomly in the detector volume. Number of MC generated events is set 70 events/min weighted by the actual livetime during SK-IV after the run selection in Section 6.1 for this solar neutrino analysis. The solar direction is also taken from actual livetime weight. The expected spectrum of the ^{8}B solar neutrino considered of the SK detector performance based on the Winter spectrum is shown in Fig. 4.7.

The expected rate is calculated by multiplying the neutrino flux ($\Phi^{^8\mathrm{B}}_{\mathrm{SNO,NC}}$), the number of electrons in ID and the Winter spectrum. $\Phi^{^8\mathrm{B}}_{\mathrm{SNO,NC}}$ is 5.25×10^6 /cm^2/s, which is the neutrino flux

measured by the NC reaction of the SNO experiment as described in Table 4.1. The amount of the flux from the NC reaction corresponds to that assuming no neutrino oscillation.

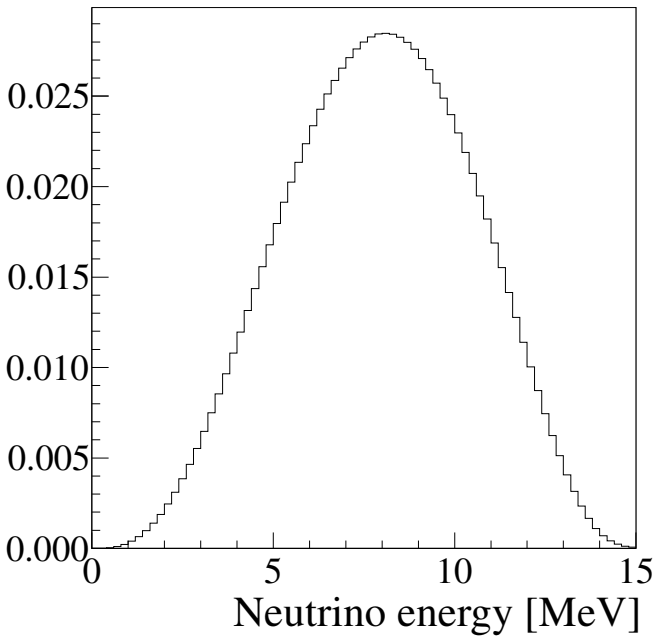

Figure 4.7: The expected spectrum of the ^{8}B solar neutrino detected by the SK detector based on the Winter spectrum.

Table 4.1: Expected event rate.

Neutrino type	Theory		Expected event rate in ID
	Flux [$\times 10^6$ /cm^2/s]	Spectrum	[Events/days]
^{8}B	SNO NC (5.25)	-	294.7
	BP2004 (5.79)	Winter [36]	325.1
hep	BP2004 (7.88)	Bahcall [37]	0.6375

4.2.2 Tracking of Cherenkov photon

In this step, propagation of the Cherenkov photon from generation of the photon to arrival to the PMT (Acrylic cover) or the black sheet on the wall in the water is simulated. Cherenkov radiation is shown in following equation.

$$\frac{d^2N}{dxd\lambda} = \frac{2\pi\alpha}{\lambda^2}\left(1 - \frac{1}{n^2\beta^2}\right) \tag{4.6}$$

The light wavelength is $\lambda > 300$ nm, mean free path of the Cherenkov photon is calculated with the correction parameters. The tracking is simulated as taking into account of the water transparency and the TBA as mentioned in Section 4.1.

4.2.3 Absorption and reflection of the Cherenkov photon by the detector material

An absorption and a reflection due to the photon hits on the detector materials such as the black sheet on the inside wall, the acrylic cover of the PMT, and the PMT itself are simulated. The MC simulation of the ID PMT assumes four layers, water, glass, bialkali and vacuum in the PMT. The black sheet has a characteristic for Lambert reflection which is an ideal diffuse reflection and occurs to reflect all directions uniformity regardless of the incident angle of the photon. The Lambert reflection on the surface of the sheet is simulated in the MC simulation, it occupies approximately 3% of a whole, and assumed the rest 97% are absorbed. The reflection is measured by using a laser beam which is injected to the black sheet. The acrylic cover over the ID PMT is installed to protect the PMT from chain implosion in the SK detector. When the photon enters or exits the acrylic volume, the photon reflects or refracts at the interface between the water and the acrylic cover as shown in Fig. 4.8. Three patterns, the water to the acrylic, the acrylic to the water, and the absorption are considered in the simulation. These responses are measured by using a spectrometer.

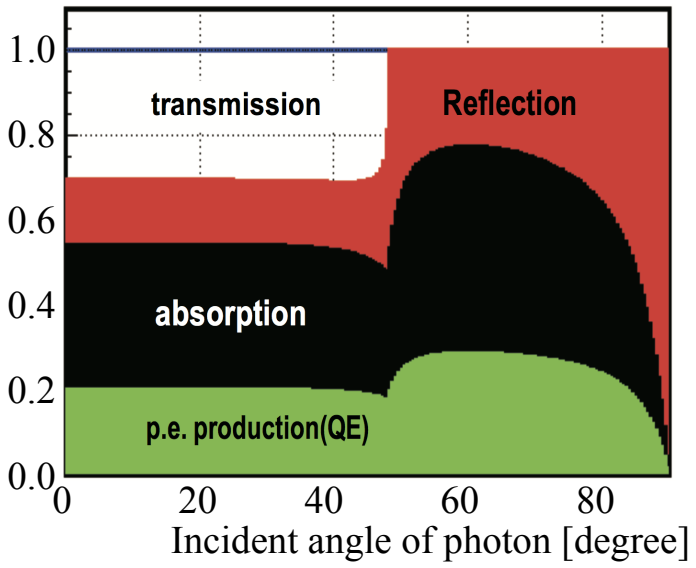

Figure 4.8: Fraction of the reflection, the absorption and the photo electron production on the PMT surface [33]. The horizontal axis shows incident angle of the photon for $\lambda = 420$ nm of the wavelength of an incident photon.

4.2.4 Response of the detector

A generation probability of photo-electrons is calculated after the Cherenkov photon passes through these materials and reaches a photoelectric surface in the PMT. The probability that the Cherenkov photon entering the surface arrives to first dynode is obtained by multiplying the quantum efficiency and an individual quantum efficiency of each PMT, and the correction factor. The individual quantum efficiencies and the correction factor are set in initial setting. Next, the photo-electron reaching to the first dynode is amplified and an amount of charge of the photo-electron is calculated. Then, the total amount of charge in an ADC timing gate is simulated.

Chapter 5

Energy scale calibration

5.1 Purpose of energy scale calibration

In order to precisely measure the solar neutrino oscillation, a high-precision absolute energy scale is required. To discuss the properties of neutrino such as the MSW, the uncertainty due to the absolute energy scale is needed to be reduced. The absolute energy scale corrects the PMT acceptance, the collection efficiency, and the water quality as described in Section 4.1. The absolute energy scale in the low-energy region is determined mainly by electron linear accelerator (LINAC) calibration and deuterium-tritium (DT) calibration. The decay electron is also used for estimating the stability of the energy scale.

5.2 PMT gain and dark rate correction

Gain and dark rate of the ID PMT had fluctuated during the SK-IV as shown in Fig. 5.1 and Fig. 5.2. The fluctuation of the gain and the dark rate are different each production year. The increases are likely to lead an overestimation of the number of hit PMTs because non-significant signals exceed the threshold of the front-end electronics. These variations are taken into account in this solar neutrino analysis.

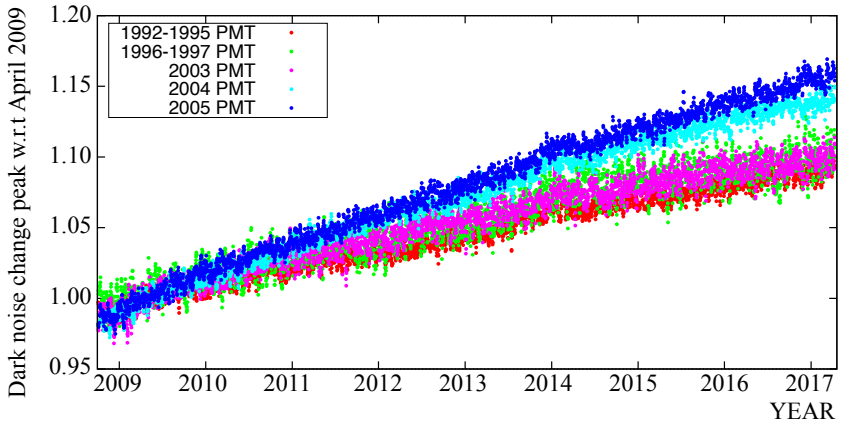

Figure 5.1: PMT gain change of each SK run. The vertical axis shows relative gain change with regards to April of 2009. The increases of the relative gain are different by each production year.

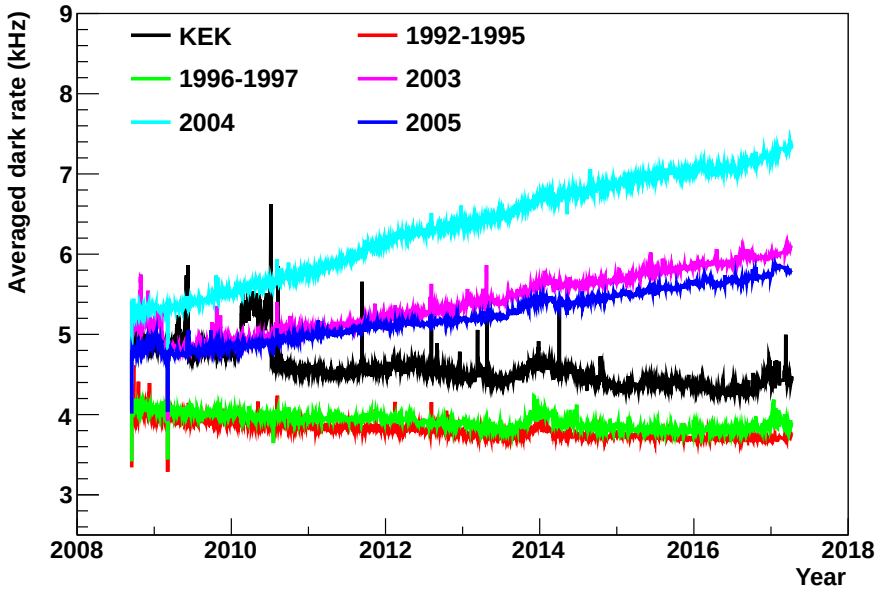

Figure 5.2: Time variation of the dark rate of each SK run. The vertical axis shows the average of the dark rate (kHz) over each SK run. The color variation shows the production year. Black line shows the PMTs used in the K2K experiment and reused in SK.

Actually, the single photo electron distribution is shifted by the gain increase as shown in Fig. 5.3.

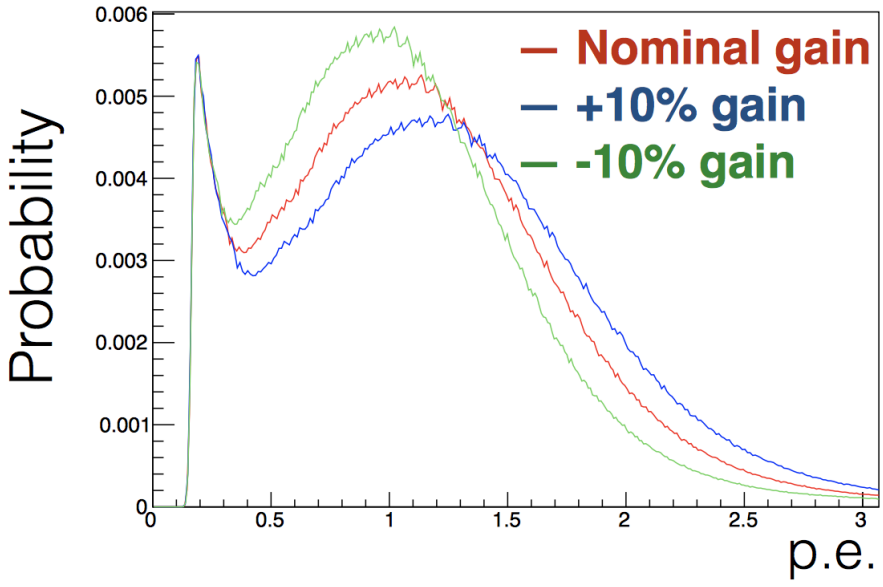

Figure 5.3: The single photo electron distribution. The peak value of the single electron distribution shifts with increasing gain.

Therefore, the time variation of the PMT gain and PMT-by-PMT dark noise are considered

to the calculation for the energy reconstruction. These corrections are applied to both of the data analysis and the MC simulation. In following subsection, the method of implementation to the energy reconstruction is described.

5.2.1 Implementation to the energy reconstruction

The gain correction is incorporated into the energy reconstruction mentioned in Section 3.2.3. The correction are corrected to both the data analysis and the MC simulation through modifying the factor, X_i, ϵ_{dark} and L in the formula for the effective number of hits described in Eq. (3.8).

$$X_i \rightarrow X_{i,c} = \frac{X_i/QE_i}{1 + F_G \times C} \tag{5.1}$$

$$\epsilon_{\rm dark} \rightarrow \epsilon_{dark,c} = \frac{\epsilon_{dark}}{1 + F_G \times C} \tag{5.2}$$

$$L \rightarrow L_c \tag{5.3}$$

C is a gain conversion factor. The gain conversion factor is estimated as following step. First, the increases of the PMT hit rate and the gain are assumed to correlate linearity each other, $F_N = F_G \times C$. $F_G = (G_t - G_0)/G_0$ represents the gain increasing fraction, where G_0 is the relative gain at April 2009 and G_t is the relative gain at the time of the reconstructed event. $F_N = (N_t - N_0)/N_0$ represents the increase of hit rate, where N_0 is the hit rate at April 2009 and N_t is the hit rate at the time of a reconstructed event. The gain conversion factor, $C = 0.226 \pm 0.003$, is obtained by fitting the time variation of Y-intercept described in Section 4.1.1, because the gain increasing also appears in the effective number of hits of the decay electrons. The dark rate also increases each production year of PMTs as shown in Fig. 5.2. Therefore, the PMT-by-PMT dark rate is also incorporated to the energy reconstruction in this analysis. Since the water transparency (L) is calculated by using the number of hit PMTs as described in Section 4.1.1, it is affected by the gain fluctuation.

5.2.2 Result obtained from the corrections

Figure 5.4 (without the gain correction) and Fig. 5.5 (with the gain correction) show a time variation of the effective number of hits of the decay electron. Center points in the figure show the peak value of energy distribution of the decay electron. The energy scale uncertainty becomes stable during the SK-IV period by implementing the gain correction in the detector simulation and the energy reconstruction.

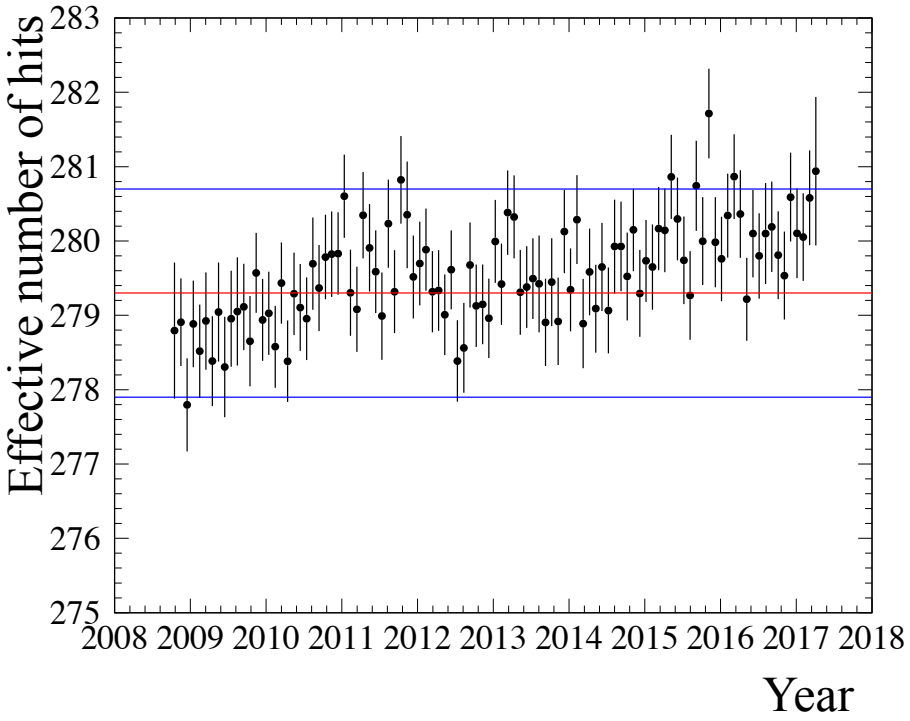

Figure 5.4: Time variation of the effective number of hits of the decay electron without the corrections. Red line is an average of the time variation. Blue line is ± 0.5% to the average.

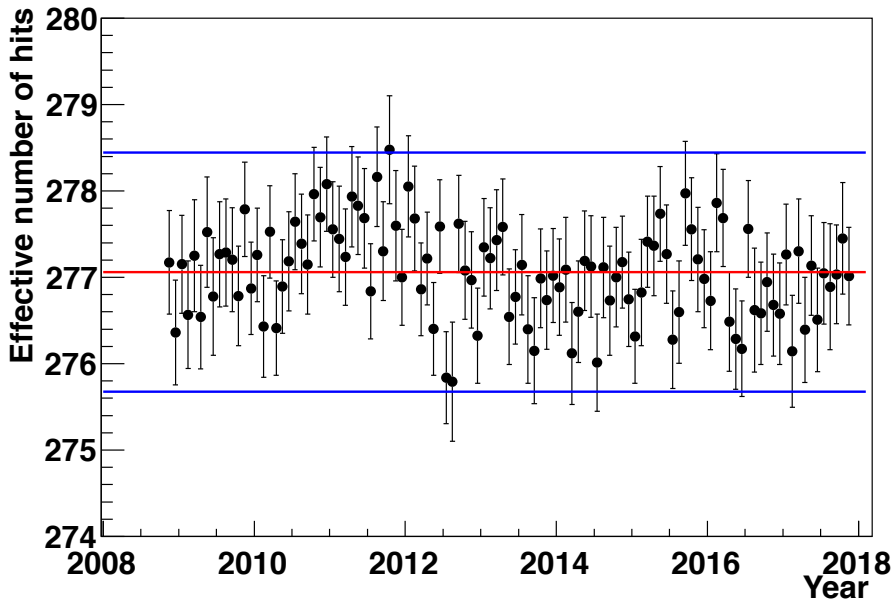

Figure 5.5: Time variation of the effective number of hits of the decay electron with the corrections. Red line is an average of the time variation. Blue line is ± 0.5% to the average.

5.3 LINAC calibration

The absolute energy scale for the solar neutrino analysis is determined by electron linear accelerator (LINAC) calibration. For the energy region of the solar neutrino, the LINAC calibration can provide the energy scale calibration in a high accuracy. The LINAC calibration system can inject single mono-energetic electrons into the SK detector in the downward direction. The LINAC calibration has three advantages in measurement of the absolute energy scale as follows.

1. Generate the single mono-energetic electrons in the energy region of the solar neutrino events and calibrate by using electron-derived Cherenkov lights. Since other calibrations are calibrated by using gamma-ray source, the Cherenkov light created by secondary electron is observed. Therefore, it is impossible to directly know the energy of the electron, and it must be based on the MC simulation.

2. Systematic uncertainties of the vertex resolution and the angular resolution of the SK detector can be estimated since the vertex and the direction of electrons entering the water are well-known as the endcap of the LINAC beam pipe.

3. Systematic uncertainties of the energy scale in the same energy region as solar neutrinos can be also confirmed.

The LINAC calibration of SK-IV is done in 2009, 2010, 2012, 2016 and 2017, but the LINAC data in 2009 is not used in this analysis because water quality was worse in the LINAC period. The LINAC calibration system, calibration for LINAC beam, method of calculation of energy scale and result of the LINAC calibration are described in this section. To determine the energy scale, peak values of the effective number of hits distribution of the LINAC calibration data and the MC simulation are compared using the electrons with the energy of about 4.0 MeV to 19.0 MeV.

5.3.1 LINAC calibration system

The LINAC calibration system consists of mainly the electron gun, the linear accelerator, the beam pipe, the magnet, the beam monitor as illustrated in Fig. 5.6. The reason of that the LINAC is installed in a far place from the SK detector is the LINAC itself becomes a radioactivity (γ-ray) source. Therefore, the LINAC is in a off side of a rock wall and managed as control area for radiation. Flow of the LINAC beam from generation of electrons to reaching into the water is described as follows.

1. The electron gun generates thermo-electrons and shot to the accelerating cavity of the LINAC. However, the LINAC can not fine tuning the energy of electrons and at this point, the electron has a range of energy, and the energy is aligned by electromagnet.

2. To inject one electron par bunch at the endcap of the beam pipe, the number of electrons are adjusted by voltage of the electron gun. If multiple electrons par bunch inject to the SK detector, the events are not used for LINAC analysis because it has an energy distribution with two or more peaks.

3. The electrons are accelerated by high-frequency wave (Microwave) in the accelerating cavity of the LINAC.

4. The mono-momentum electrons are bended and selected by the D1 magnet since the accelerated electrons has spread of momentum at that time.

5. Furthermore, the spread of the momentum is sharpen by collimators in the beam pipe.

6. The electrons are bended by the D2 magnet and the D3 magnet.

7. The electrons are concentrated to the center of the beam pipe by monitoring hit rate at five scintillation counters supported near the endcap and fine tuning by the X-Y magnet. Finally, the electrons are injected into the water of the SK detector through the trigger counter in the endcap of the beam pipe.

The water in the SK detector and the vacuum (10^{-2} Pa) in the beam pipe are separated by the titanium window at the endcap. To get less influences from the multiple scattering and energy loss, the vacuum drawing is done every setup. There are nine measurement points, which correspond to the endcap position of the beam pipe.

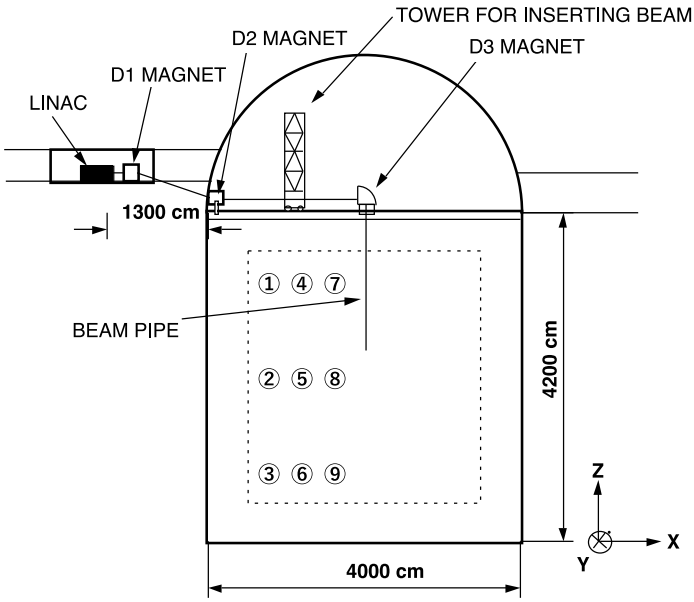

Figure 5.6: Diagram of the LINAC system. Circled numbers in the diagram show the measurement points (corresponding to the endcap position of the beam pipe) [38].

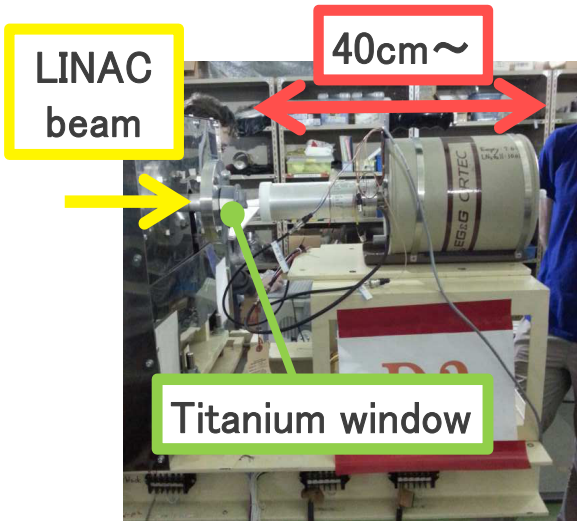

Figure 5.7: Picture of the Ge detector for the LINAC beam calibration around the D3 magnet.

5.3.2 LINAC beam energy calibration

In order to discuss a precise energy scale calibration, LINAC beam energy is measured by the Germanium (Ge) detector, which is a kind of semiconductors. The Ge detector is set at position near the D3 magnet illustrated in Fig. 5.7. As the calibration of the beam energy, the D3 magnet

is turned off because the LINAC beam must be go straight to the Ge detector as illustrated by yellow arrow in Fig. 5.7. For that reason, the around D3 magnet is designed same condition such as the trigger counter and the titanium window at the endcap position of the beam pipe. This measurement of the LINAC beam energy is calibrated just before every LINAC calibration run.

The most advantage for using the semiconductor detector is superior in an energy resolution and a linearity of reactivity. The linearity is checked as shown in the left of Fig. 5.8. This is advantage not only that it is possible to accurately measure the absolute energy scale, but it can be also checked the spread of the beam energy as well. The distributions of the Ge calibration data and the Ge simulation are compared as shown in the right of Fig. 5.8 and its difference is evaluated by the minimum χ^2 method.

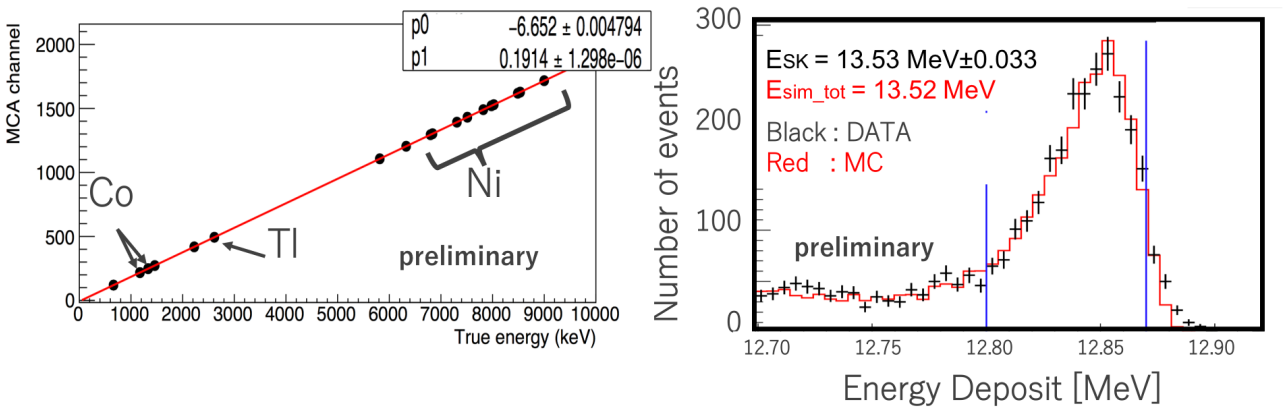

Figure 5.8: (Left) a linearity of the Ge detector calibrated several radioactivity sources. Ni,Tl and Co are used as the gamma ray source to calibrate the Ge detector. Red line shows a fitting function. The data points and the fitting function are good agreement. (Right) typical distributions of the Ge calibration data and the Ge simulation. Black cross shows the number of events with the Ge detector by injecting approximately 13.0 MeV LINAC electron beam. Red line shows an expected distribution by the Ge simulation. Blue line is a fitting range for calculating the value of χ^2. The horizontal axis shows an energy deposit in the Ge detector.

5.3.3 Calibration for Ge detector

To measure the energy scale and the linearity of response of the Ge detector itself, the Ge detector is calibrated by using some γ-ray sources just before every LINAC run. Ni, Cs and Tl are used as the γ-ray source for the calibration. In the LINAC calibration, the Ge detector detects the electron in the LINAC beam but not the γ-ray. Therefore, the calibration for the Ge detector was done by injecting electrons with well-known energy from a β-ray spectrometer to the Ge detector instead of the LINAC beam [38]. Then, the energy loss in the insensitive volume and the light receiving window of the Ge detector was measured. The systematic uncertainty of the absolute energy scale due to the uncertainty on the measurement of the LINAC beam energy is 0.21% [27].

5.3.4 Results of the LINAC calibration

Typical distributions of the reconstructed vertex, angle, energy, effective number of hits obtained from the LINAC calibration are shown in Fig. 5.9. The angular distribution represents an angle between the reconstructed direction and the incident direction (downward) of the LINAC beam. In order to check stability of the LINAC beam, these distribution are checked every LINAC calibration run. The distributions of the LINAC data are agreement with that of the MC simulation in all LINAC period.

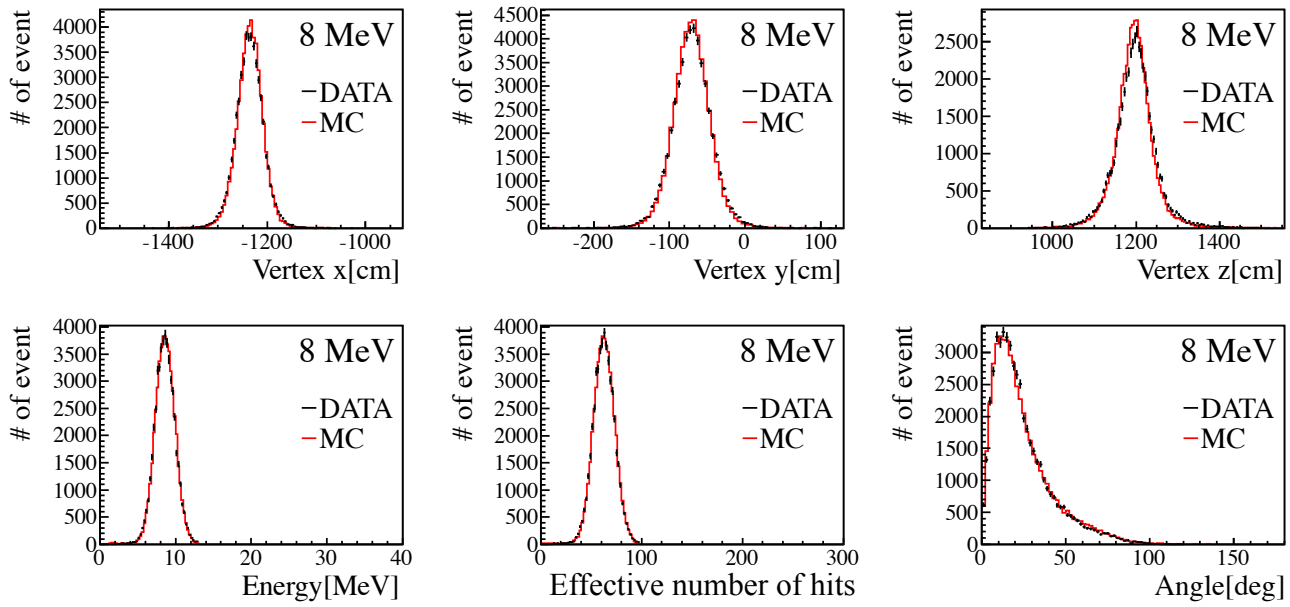

Figure 5.9: Comparison between LINAC data (back) and MC (red) for total energy of 8 MeV of typical distribution.

The analysis conditions for the LINAC calibration of Fig. 5.9 are shown below.
- DATA

1. Calculation of the effective number of hits and the reconstructed energy
2. LINAC trigger event
3. Single electron event

- MC

1. Calculation of the effective number of hits and the reconstructed energy
2. Number of the MC generated events is 500,000 events

Then, the peak values of the effective number of hits distributions of the LINAC data and the MC simulation are compared and the peak value of the MC simulation is adjusted to be agreed with that of the LINAC data by using the absolute energy scale correction factor. Figure 5.10 shows ratio of the effective number of hits of data and MC at each measurement point after tuning

by the the absolute energy scale correction factor. As a result, the correction factor is determined to approximately 0.866 in this analysis.

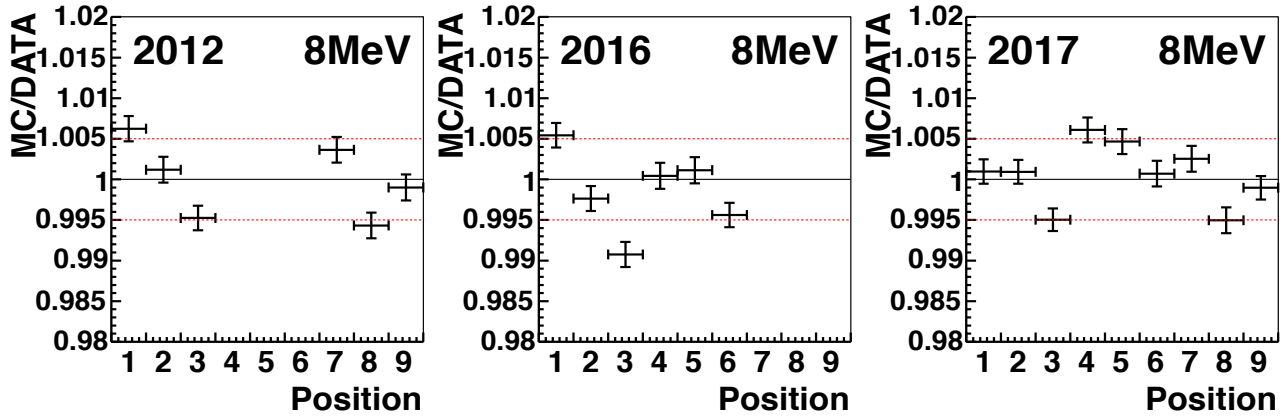

Figure 5.10: Ratio of the LINAC data and the MC simulation of the effective number of hits in 2012, 2016, 2017 at an approximately 8 MeV of the total energy. A vertical axis is MC/DATA of the effective hit and a horizontal axis shows measurement points as illustrated in Fig. 5.6. Red dotted line is ± 0.5% of MC/DATA =1 which corresponds to that peak value of the effective number of hits distribution of the data is consistent with that of the MC simulation.

Next, the systematic uncertainty of the position dependence of the energy scale is estimated from the results. The position dependence includes the systematic uncertainties of the z-direction and the x-direction, but it does not include the systematic uncertainty of y-direction because the LINAC measurement points are in the x-z plane. The mean square values of the energy scale are multiplied by position weights and calculate the root mean square in all position shown in Fig. 5.11. The position weights are determined to 3.726 (1), 4.398 (2), 3.697 (3), 2.199 (4), 2.595 (5), 2.181 (6), 1.151 (7), 1.359 (8), 1.142 (9), and the number in parentheses shows the position number corresponding to the number in Fig. 5.6. The position weight means that effective volume of the LINAC data at each position and is calculated by geometric division of the inner volume. Therefore, the total number of the position weights is approximately 22.5, which is consistent with the fiducial volume (22.5 kton) of the SK detector. This dimensionless parameters denote a fraction of the effective volume of the energy scale measured at each position. The outside position weights (position 1,2,3) are larger than the inside weights consequently since the SK detector has cylindrical shape. As a result, the systematic uncertainty of the position dependence for the energy scale is determined to 0.46%.

An energy resolution and an angular resolution are also estimated by the LINAC calibration. The energy resolution is calculated by dividing 1σ by the peak value of the energy distribution shown in Fig. 5.9 at each LINAC year and each LINAC measurement position. These values are obtained by the Gaussian fit to the energy distribution within 3σ. The results are shown in Fig. 5.12.

The energy resolution function calculated by utilizing electron MC of monochromatic energy, uniform direction and vertex is

$$\sigma(E_e) = (-0.0664 + 0.329\sqrt{E_e} + 0.0422E_e). \tag{5.4}$$

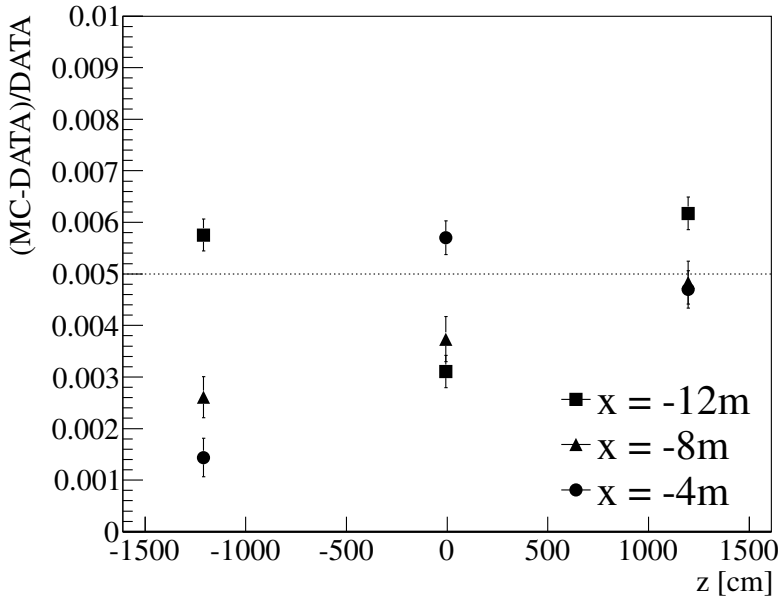

Figure 5.11: Mean square values at each LINAC measurement position.

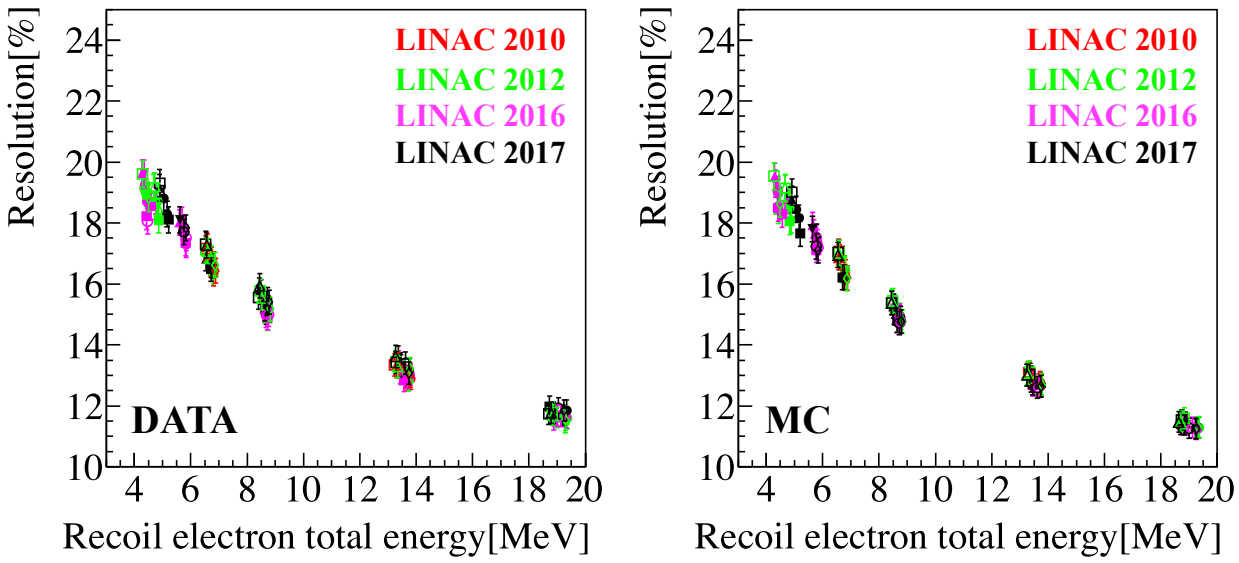

Figure 5.12: Distribution of the energy resolution of (Left) data (Right) MC at each LINAC calibration year.

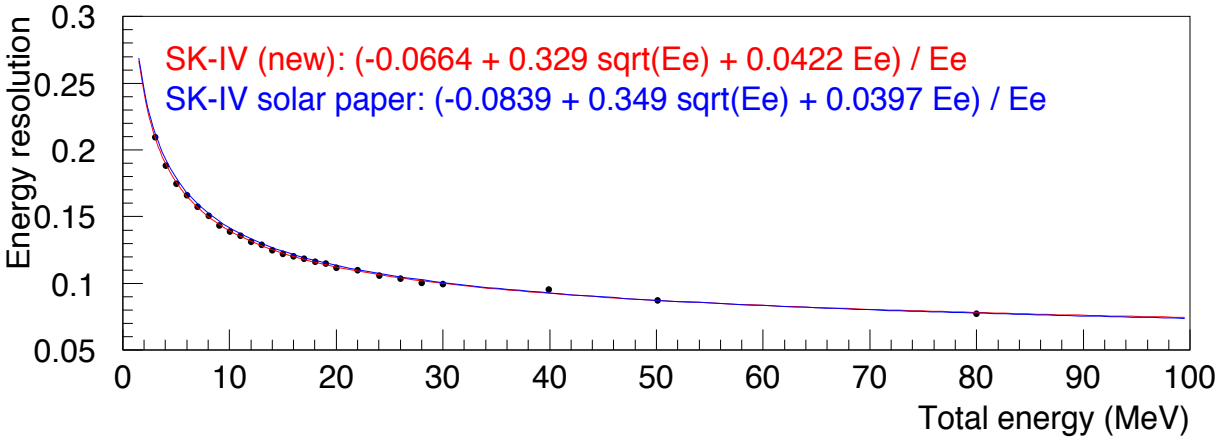

Figure 5.13: Energy resolution function obtained from monochromatic energy electron MC.

The angular resolution is estimated by the following steps:

1. Make the angular distribution of the reconstructed direction relative to z-axis
2. Apply event cut similar to the solar neutrino analysis to the angular distribution.
3. Extract the angle ($\theta_{\rm diff}$), as shown in the left of Fig. 5.14, including 68% of all events. In the angular distribution, it corresponds to the number of events in the left side of the blue dotted line in the right of Fig. 5.14.

As a result, the distribution of the angular resolution of the LINAC calibration are shown in Fig. 5.15 and are used to estimation of the systematic uncertainty of the angular resolution as described in Section 8.1.5.

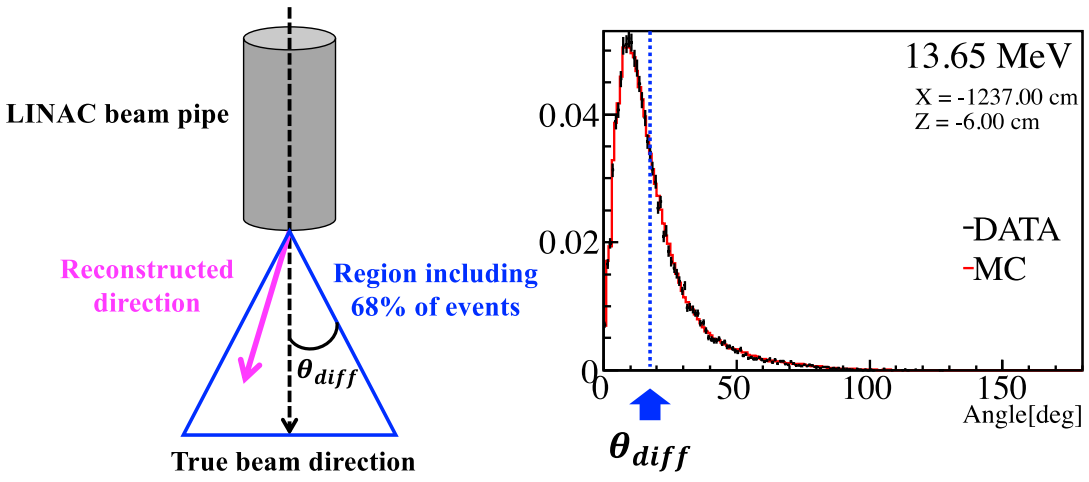

Figure 5.14: (Left) Definition of the angular resolution ($\theta_{\rm diff}$). (Right) Example of the angular distribution for 12 MeV of the LINAC beam energy at a LINAC position (x = -12 m, z = 12 m).

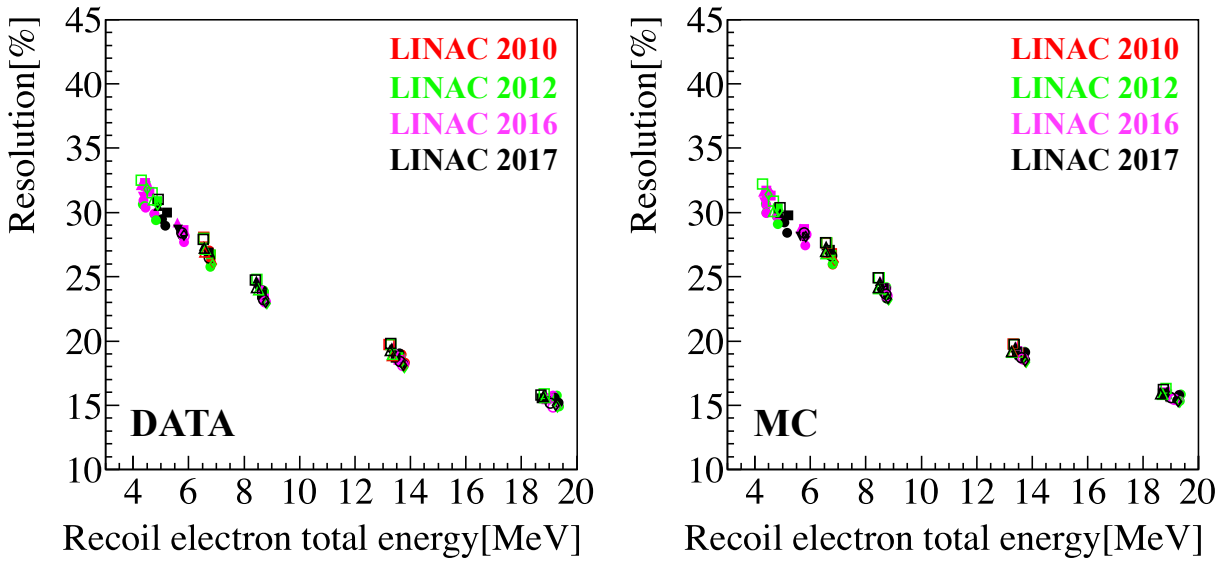

Figure 5.15: Distribution of the angular resolution of (Left) data (Right) MC at each LINAC calibration year.

5.3.5 Systematic uncertainty of the energy scale from the water transparency

The systematic uncertainty of the energy scale due to the uncertainty of the water transparency is estimated by the following steps.

1. Calculate the average of the error of the water transparency (error of slope in Fig. 4.4) during the LINAC period. The average during all LINAC periods (2010, 2012, 2016 and 2017) is 128.858 cm.

2. Add the average value (128.858 cm) to the original water transparency value in the LINAC MC simulation artificially.

3. Calculate the difference of the effective number of hits between original and shifted one.

As a result, the obtained systematic uncertainty from the water transparency is 0.11%.

5.4 DT calibration

A deuterium-tritium (DT) calibration is used for cross-check the absolute energy scale obtained by the LINAC calibration and estimating the systematic uncertainty for the directional dependence of the energy scale [39]. The DT calibration is superior to the LINAC calibration in the following points.

1. The DT calibration can perform frequently of once in three or four months since the DT calibration is not needed a large scale setup against the LINAC calibration. Therefore, the DT calibration can measure the time variation of the energy scale.

2. The DT calibration data of many calibration points in the SK detector can taken. The LINAC calibration has only the measurement points in negative x-axis. However, the DT calibration can measure at all calibration holes. Therefore, the position dependence of the energy scale in the SK detector can be estimated accurately.

3. The directional dependence of systematic uncertainty of the energy scale can be estimated by the DT calibration, but the LINAC calibration is check only the energy scale of downward direction.

Just like the LINAC calibration, electrons with well-known energy are generated by a reaction starting from the DT generator.

5.4.1 Method of the DT calibration

The DT calibration has a reaction generating the calibration source ^{16}N from a deuterium and tritium generator. First, the DT generator yield neutrons with 14.2 MeV through the following reaction.

$$^{3}\mathrm{H} + {}^{2}\mathrm{H} \rightarrow {}^{4}\mathrm{He} + \mathrm{n} \tag{5.5}$$

Secondly, the neutron reacts with oxygen in the water of the SK detector through the following reaction.

$$^{16}\mathrm{O} + \mathrm{n} \rightarrow {}^{16}\mathrm{N} + \mathrm{p} \tag{5.6}$$

The DT generator is operated by a procedure as shown in Fig. 5.16.

In the third, $\gamma + \beta$-ray which are yielded from ^{16}N with a Q-factor of 10.41 MeV are detected by the SK detector. The electron has 4.3 MeV and 10.41 MeV and, its energy is corresponding to the recoil electron from the solar neutrino. The electron are emitted uniformity to radial directions from the DT generator.

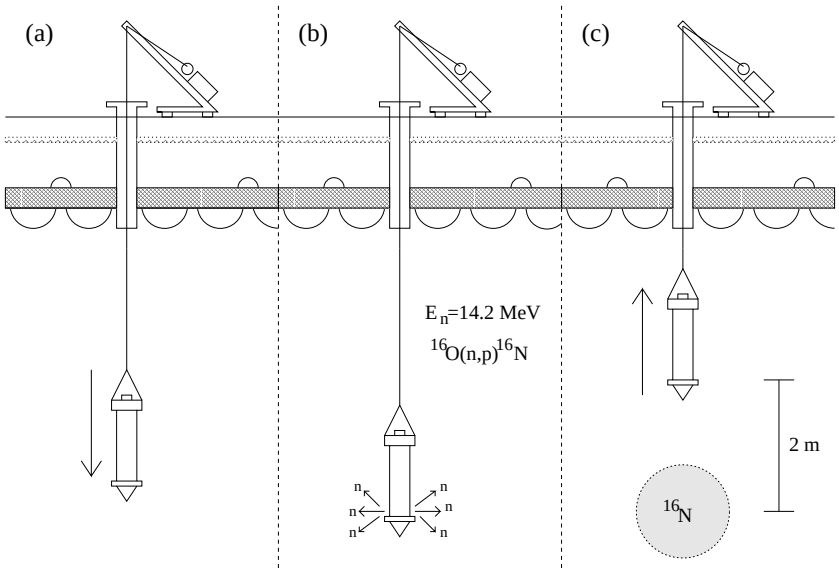

Figure 5.16: Measurement position for the DT calibration [39].

The energy distribution of the calibration data and the MC simulation for the DT calibration is shown in Fig. 5.17.

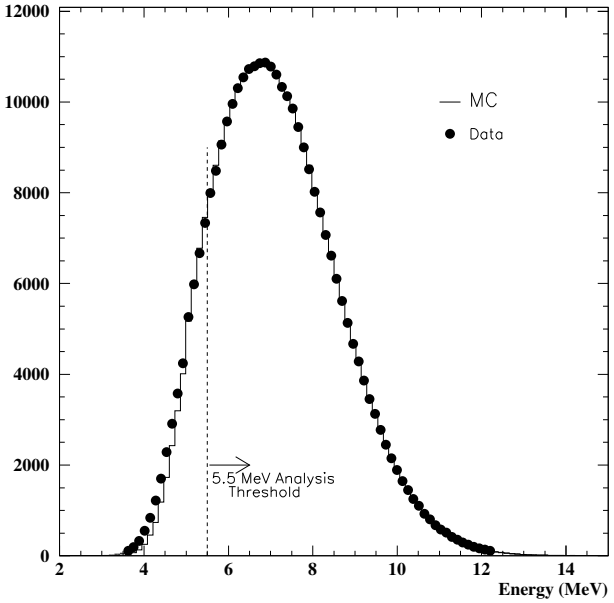

Figure 5.17: The energy distribution of the data and the MC simulation for the DT calibration [39].

5.4.2 Results of the DT calibration

The absolute energy scale correction factor determined by the LINAC calibration is cross-checked by using the results obtained from the method in Section 5.4.1. The correction factor is applied the MC simulation of the DT calibration, and the effective number of hits of the MC simulation are compared with that obtained from a real data of the DT calibration. The energy scale is confirmed that the results are consistent within ±0.5% with respect to the average of the effective number of hits during SK-IV as shown in Fig. 5.18.

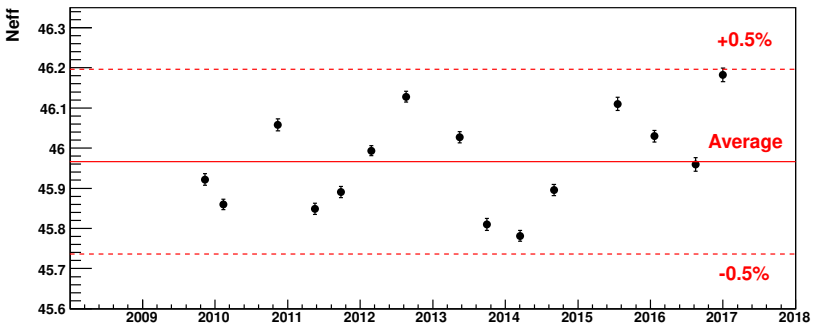

Figure 5.18: Results of the effective number of hits for the DT calibration at the center position of the SK detector during SK-IV.

In order to we can only measure the energy scale to the downward direction by the LINAC calibration, the systematic uncertainty of the directional dependence for the energy scale is estimated by the DT calibration. As a result, the uncertainty is determined to 0.10% as shown in Fig. 5.19.

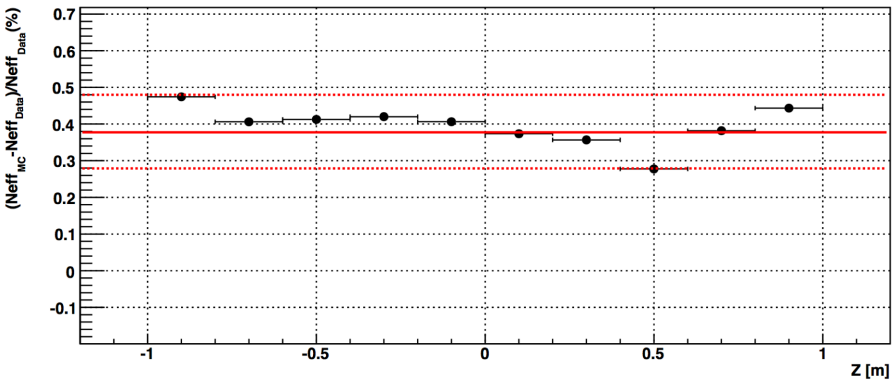

Figure 5.19: The systematic uncertainty of the energy scale measured by the DT calibration at position (x, y, z) = (0, 0 ,+12) m. Red solid line is the average during SK-IV and the dotted lines show the directional uncertainty 0.1%.

5.5 Summary of the systematic uncertainty in the energy scale

Summary of the systematic uncertainties in the energy scale is described in Table 5.1. The total systematic uncertainty calculated by adding these uncertainties in quadrature is 0.53%.

Table 5.1: Summary of the uncertainty of the energy scale in SK-IV

Position Dependence	0.46%
Direction Dependence	0.10%
Water Transparency	0.11%
LINAC Energy	0.21%
Total	0.53%

Chapter 6

Event selection

In this chapter, the process of real data analysis is described. Background events such as noises detected by bad PMTs and muon spallation events are rejected from the real data as mentioned in following.

1. Run selection
2. First reduction
3. Spallation cut
4. Ambient cut
5. External cut
6. Final reduction

It is noted that these reduction cuts are applied to both the data analysis and the MC simulation.

6.1 Run selection

The analytical unit (Run) of SK-IV is consisted of a lot of subruns with an approximately 67 s and has an approximately 24 hour. Data quality requirements called bad run reduction removes problematic runs such as some detector troubles, unstable event rate, test runs and calibration runs which can not be used in the solar neutrino analysis. The following run (subrun) isn't used for the solar analysis because the data quality of the run (subrun) is bad.

- Short run
  The short run which has run time less than 1.5 hour
- HV turn on
  The event rate gradually decreases after HV turn on because the dark rate is higher than that of a normal continuous run. Therefore, the first 200 subruns from the beginning of the run just after HV on are discarded.

- DAQ error
  If a run stops due to a DAQ error, the last 5 subruns of the run are discarded.

- Unstable ID PMT rate
  The event rate above 5 MeV with 2 m of fiducial volume cut is stable by approximately 5 Hz. However, if the event rate is not stable, higher or lower than the rate or has a spike, their unstable subruns are discarded.

- Cluster in the vertex distribution
  The cluster can be sometimes found in the vertex distribution as shown in Fig. 6.1. The cluster is likely to be a flasher, and the run including the cluster is discarded.

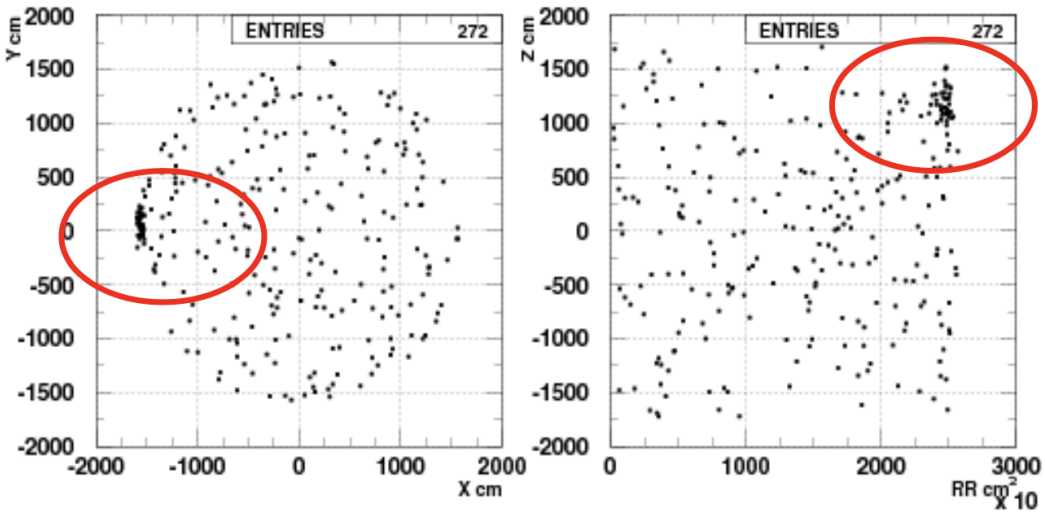

Figure 6.1: Example of the cluster events (red circle). The vertex x-y distribution (Left) and the vertex r^2-z distribution (Right) show the cluster candidate.

- Test run and calibration run
  As the test runs, for example, LED Supernova burst test and calibration runs are removed.

- Bad channel (PMT) cut
  In order to that the ID PMT and the OD PMT of SK have used for a long time, some of them have stopped working (= bad channel). The number of the bad channels ($N_{\rm bad}$) is increased gradually as shown in Fig. 6.2, it is about 140 (200) corresponding to about 1% (10%) of all ID (OD) PMTs at the end of SK-IV. However, $N_{\rm bad}$ sometimes fluctuates each run when DAQ or electronics trouble is happened. Therefore, the run (subrun) which has the bad channels over (monthly average + 36) is discarded.

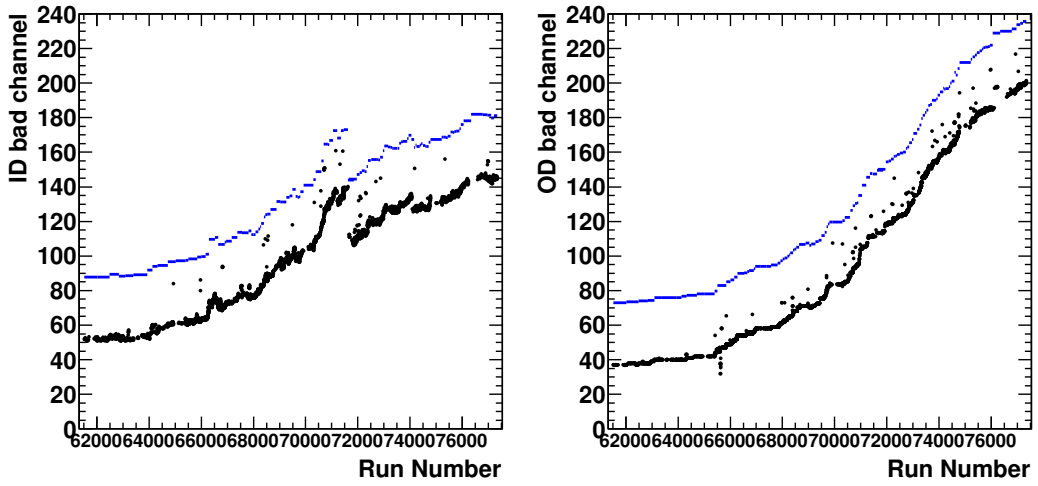

Figure 6.2: Time variation of the number of the bad channels of the ID PMTs (Left) and the OD PMTs (Right) after the bad channel cut. Run which has the bad channels over the cut criteria (blue plot) is discarded.

- Muon rate
  Events in the run selection are defined as the number of ID hit PMTs more than 1000. The rate of muon event should be stable. The run (subrun) which has the muon rate out of a range from 1.047 to 2.847 muon/s as shown in Fig. 6.3 is discarded.

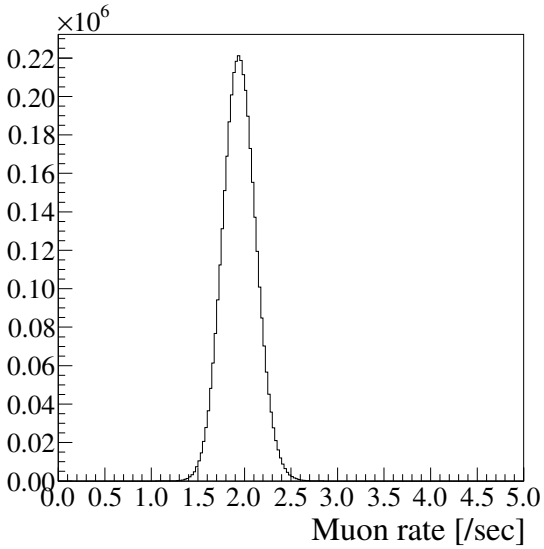

Figure 6.3: Distribution of the muon rate.

As a result of the run selection, the total livetime of the observation period in SK-IV is 2860 days.

6.2 First reduction

First reduction applies loose cuts in order to removing an obviously bad event. The first reduction is done in online whenever the run finishes the data taking because this reduction needs a long processing time.

6.2.1 Trigger requirement

SLE, LE and HE trigger events are used in the solar neutrino analysis, and others are removed. The kind of the trigger is described in Section 3.1.3.

6.2.2 Low-energy event selection

The events satisfying that $N_{\rm hit}$ is less than 400 are selected as the low-energy event. $N_{\rm hit}$ is a number of hit PMTs within 1.3 μs timing width.

6.2.3 Implementation of the event reconstruction

After the trigger cut and the low-energy event selection, as mentions in Section 3.2, the event reconstruction is performed. Then, the event quality parameters for the solar neutrino analysis are also calculated in this step. However, they are calculated by using a temporary water transparency (90 m) and without the gain correction in the realtime process.

6.2.4 SLE reduction

In this step, very loose reduction cuts are applied to the data by using the parameters calculated by the event reconstruction. The meaning of the parameters are mentioned in Section 3.3. The events with $d_{\rm wall} < 100$ cm and $(g_V)^2$ - $(g_A)^2 < 0.1$ are removed in all period, while the events which fulfill the following conditions in each period are removed.

Period: Oct. 2008 - Dec. 2008

- $d_{\rm eff} < 450$ cm (SLE trigger only)
- $E < 3.0$ MeV

Period: Jun. 2009 - Apr. 2015

- $d_{\rm eff} < 400$ cm (SLE trigger only)
- $E < 3.0$ MeV

Period: May 2015 - Dec. 2017

- $(g_V)^2$ - $(g_A)^2 < 0.15$ and
  $\{(E < 4.5$ MeV and $d_{\rm eff} < 700$ cm) or ($E \geq 4.5$ MeV and $d_{\rm eff} < 500$ cm)$\}$ (SLE trigger only)
- $E < 2.5$ MeV

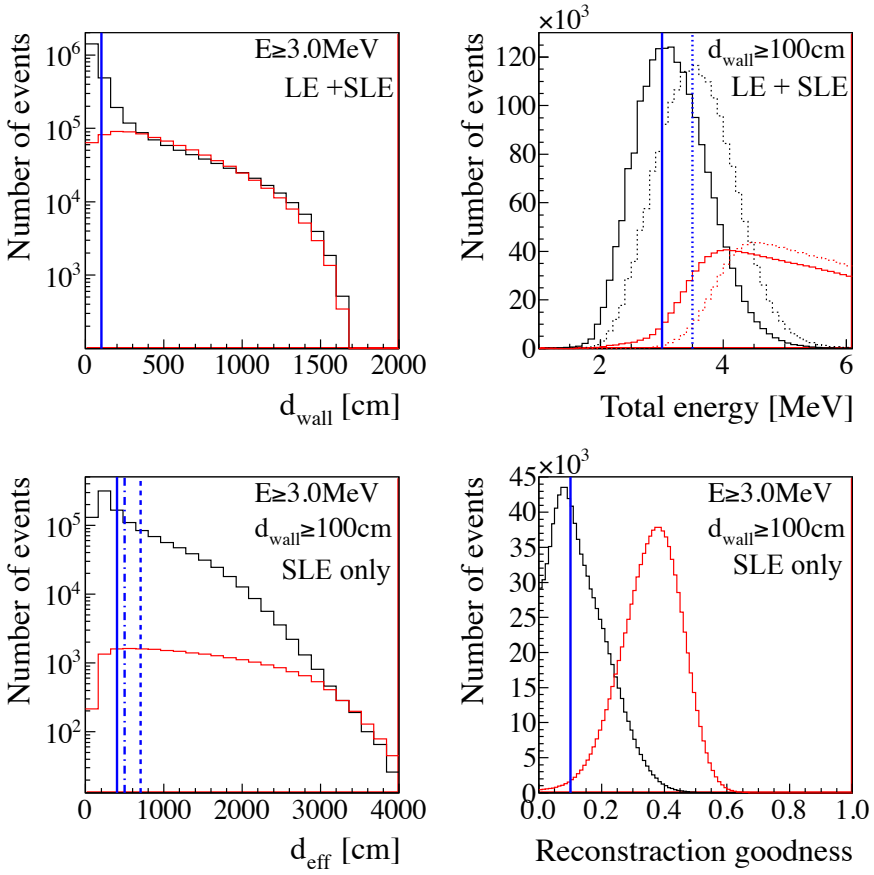

Figure 6.4: Distributions of the d_{eff}, the energy and the reconstruct goodness before the SLE reduction. The blue lines (solid, dotted, dashed, dot-dash) are cut criteria and events in left side of the lines are removed. The solid (dotted) blue line in the top right figure shows the cut criteria for the SLE threshold of the 31 hits (34 hits). The dashed (dot-dash) blue line in the bottom left figure shows the cut criteria for $E \geq 4.5$ MeV ($E < 4.5$ MeV) after May 2015.

The distributions of these parameters before the SLE reduction as shown in Fig. 6.4. The data remaining from the reduction cuts above is saved. After that, the following pre reduction are applied to the data.

6.2.5 OD cut

The events satisfying either of the following conditions are removed.

- The number of hit OD PMTs within the time window from 500 ns to 1300 ns, greater equal 20.
- OD trigger : the number of hit OD PMTs greater than 22 as described in Section 3.1.3.

6.2.6 Flasher cut

Flasher means that an event due to arc discharge on some dynodes in the ID PMT. Then, surrounding ID PMTs are also affected by the light. One of the surrounding PMTs is received

a maximum light quantity in all hit PMTs in an event most of the time. The clusters by strong flasher are found in the vertex distribution as shown in Fig. 6.1. If there are such large cluster, the corresponding whole run is removed in this step. On the other hand, weak flasher events are judged by event-by-event and removed. The flasher events are removed by using the following criteria shown in Fig. 6.5.

- Maximum charge of PMT in the event $\geq$ 50 p.e.
- The number of hit PMTs around the max charge PMT $\geq$ 3

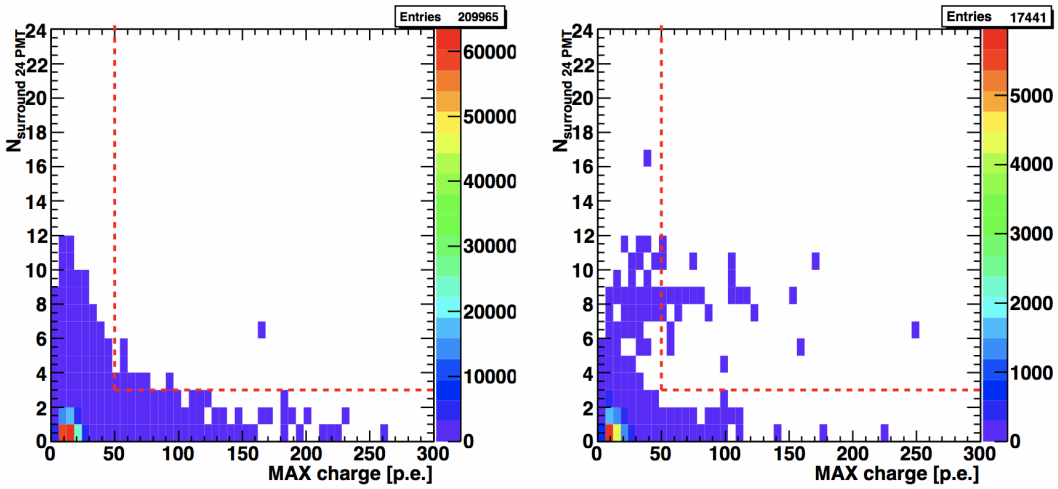

Figure 6.5: Left figure shows a normal run which does not have the flasher. Right figure shows the run with the flasher events. Vertical axis is the number of PMTs around the max charge PMT. Horizontal axis is a maximum charge in an event. Red dotted line shows a cut criteria [33].

6.2.7 Spot cut

There are spots of the reconstructed vertex due to the calibration source/cable and the sensors in the SK detector. These devices include natural radioactivity, and the radioactivity becomes the background in the low-energy region. Therefore, the spot of the sources/cables at the position shown in Table 6.1 are removed. The spot within 2 m radius from the source or within 1 m radius from the sensor is also removed. The positon of the sources and the sensors in 3.5 MeV to 5.0 MeV of kinetic energy is shown in Fig. 6.6.

Table 6.1: Positions of the calibration sources and the sensors

Source	X-position [m]	Y-position [m]	Z-position [m]
Xenon light	353.5	-70.7	0.0
LED light	35.5	-350.0	150.0
TQ ball	-176.8	-70.7	100.0
LED for supernova test	-35.3	353.5	100.0
Water temperature sensor 1	-35.3	1200.0	$>$ -2000.0
Water temperature sensor 2	70.7	-777.7	$>$ -2000.0

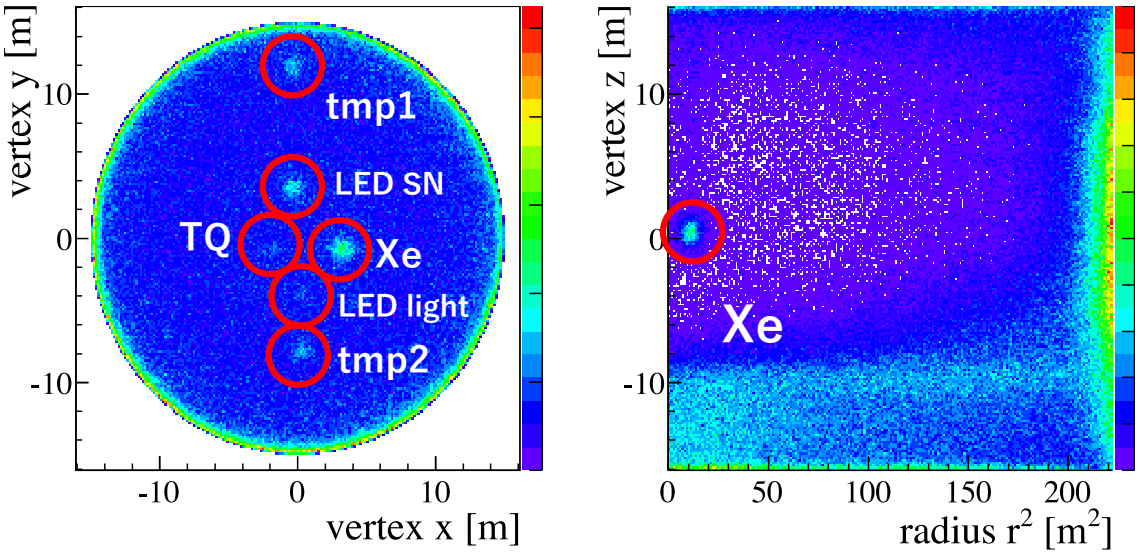

Figure 6.6: Positions of the calibration sources and the sensors in 3.5 MeV to 5.0 MeV of kinetic energy before applying the tight fiducial volume cut before April 12, 2010 because the LED light is not installed from that day on.

6.2.8 Pre-cut

- Loose fiducial volume cut
  Loose fiducial volume cut is applied by using the parameter d_{wall} shown in Fig. 3.16 in this step. The events which have the parameter d_{wall} within 2.0 m are removed.

- Time difference cut
  The events which have time difference within < 50 μs from the previous event are removed in order to remove the events of the decay electrons mainly.

- Energy cut
  The events which have the kinetic energy below 3.5 MeV are removed.

- Loose event quality cut
  The events which have the reconstruction goodness below 0.20 are removed.

- Loose external event cut
  The events which have $d_{\mathrm{eff}} < 450$ cm are removed.

6.3 Spallation cut

Spallation means that the high-energy muon breaks oxygen atoms in the water and generates unstable radioactive isotopes when passing through the SK detector. Furthermore, the spallation generates second hadronic particles such as protons, neutrons and pions, and the hadronic particles also generate unstable radioactive isotopes by the interaction with the oxygen atoms. Therefore, showers of the radioactive isotopes are formed around the muon track. The multiple gamma/beta-rays emitted from the spallation products become the main background for the solar neutrino analysis in the energy region above around 6.0 MeV because the muons are detected with relatively high frequency (about 2 Hz). Table 6.2 shows a list of the possible spallation products, a half-life, decay mode and the kinetic energy of each spallation product.

Table 6.2: List of the spallation products [3]. In the list, the isotope of the spallation, the half-life, the decay mode and the kinetic energy of Q-value for each spallation are represented. The radioactive isotope ^{16}N has the relatively long half-life.

Isotope	$\tau_{\frac{1}{2}}$[s]	Decay mode	Kinetic Energy [MeV]
$^{8}_{2}$He	0.119	β^-	9.67 + 0.98 (γ)
		β^-n	(16 %)
$^{8}_{3}$Li	0.838	β^-	$\sim$13
$^{8}_{5}$B	0.77	β^+	$\sim$13.9
$^{9}_{3}$Li	0.178	β^-	13.6 (50.5 %)
		β^-n	($\sim$50 %)
$^{9}_{6}$C	0.127	β^+p	3 $\sim$ 15
$^{11}_{3}$Li	0.0085	β^-	16 $\sim$ 20 ($\sim$50 %)
		β^-n	$\sim$16 ($\sim$50 %)
$^{11}_{4}$Be	13.8	β^-	11.51 (54.7 %)
			9.41 + 2.1(γ) (31.4 %)
$^{12}_{4}$Be	0.0236	β^-	11.71
$^{12}_{5}$B	0.0202	β^-	13.37
$^{12}_{7}$N	0.0110	β^+	16.32
$^{13}_{5}$B	0.0174	β^-	13.44
$^{13}_{8}$O	0.0086	β^+	13.2,16.7
$^{14}_{5}$B	0.0138	β^-	14.55 + 6.09 (γ)
$^{15}_{6}$C	2.449	β^-	9.77 (36.8%)
			4.47 + 5.30 (γ)
$^{16}_{6}$C	0.747	β^-n	$\sim$4
$^{16}_{7}$N	7.13	β^-	10.42 (28.0%)
			4.29 + 6.13 (γ) (66.2%)

The gamma/beta-rays emitted by the spallation products cause the non-clear Cherenkov ring pattern. In order to distinguish the Cherenkov ring pattern of the elastic scattering electron from that of the spallation background, the likelihood function using the hit pattern of the PMTs hit is adopted. The spallation products are made from through going muons and stopping muons.

6.3.1 Spallation by through going muons

The spallation candidate events derived from the short-lived isotopes are selected with a log likelihood method [27]. The log likelihood in the solar neutrino analysis is defined as follows.

$$\mathcal{L}_{\rm spa} = f(Q_{\rm res}) \times f(\Delta T) \times f(\Delta L) \tag{6.1}$$

- $Q_{\rm res}$: Residual charge

$$Q_{\rm res} = Q - Q_{\rm MIP} \times L_{\rm muon} \tag{6.2}$$

  Q is a sum of the observed charge by ID PMTs and $Q_{\rm MIP}$ is 26.78 p.e/cm for a minimum ionizing particle (MIP). $L_{\rm muon}$ is the muon track length between an entry point of muon on the wall mounted the ID detector and a position of the PMT hitting the muon. The bigger the energy loss of charged particle, the higher the probability for the muon spallation events because the radioactive isotope causing the spallation has short life and locally occurs the hadronic shower. Therefore, if the amount of residual charge at the reconstructed vertex is large, the likelihood of the spallation event is high.

- ΔT: Time difference between the spallation candidate and the muon. If the time difference is short, the likelihood of the spallation event is high.

- ΔL: Distance between the spallation candidate and the muon track. If the distance is short, the likelihood of the spallation event is high.

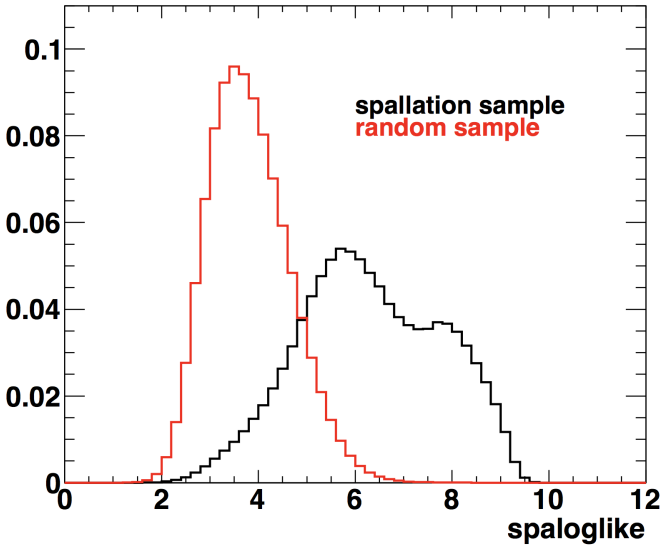

Figure 6.7: A distribution of $\log \mathcal{L}_{\rm spa}$. Black line shows a spallation sample and red line shows a random sample. Blue dashed line shows $\log \mathcal{L}_{\rm spa} = 4.52$, and the events with $\log \mathcal{L}_{\rm spa} > 4.52$ are removed [33].

The likelihood is calculated using these three parameters in the Eq. 6.1 and the events with $\log \mathcal{L}_{\rm spa} > 4.52$ are removed. The spallation sample in Fig. 6.7 is made from the event, which has

ΔT less than 0.1 s and the kinetic energy more than 7.0 MeV. The random sample in Fig. 6.7 is made from the time information which has the kinetic energy less than 4.0 MeV and generated in whole SK detector at random position.

The dead time due to the spallation cut is occurred in the solar neutrino analysis. The dead time has position dependence shown in Fig. 6.8 and described in Eq. 6.3.

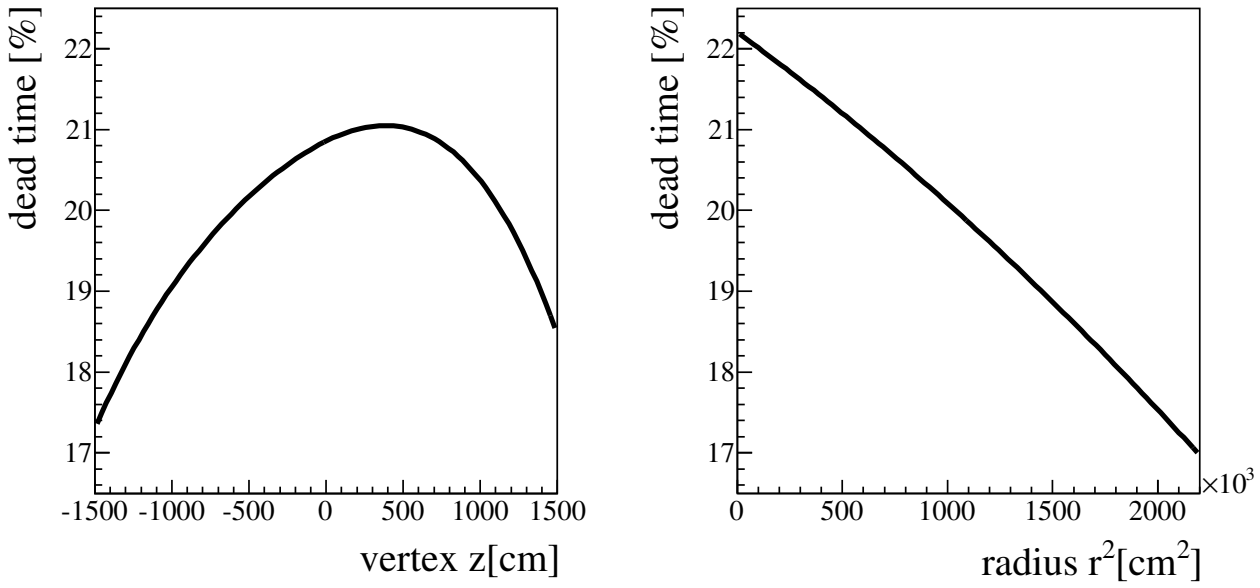

Figure 6.8: The position dependence of the dead time by the spallation cut. (Left) the hight (z) dependence of the SK detector of the dead time. (Right) the radius direction (r^2) dependence of the dead time.

$$\begin{aligned} T_{\mathrm{dead,z}} = 1.0 - (&0.79143 - 0.93206 \times 10^{-5} z + 0.98724 \times 10^{-8} z^2 \\ &+ 0.30075 \times 10^{-11} z^3 + 0.16359 \times 10^{-14} z^4 \\ &- 0.26618 \times 10^{-18} z^5 - 0.63656 \times 10^{-22} z^6)[\%] \\ T_{\mathrm{dead,r^2}} = 1.0 - (&0.77799 + 0.18903 \times 10^{-7} r^2 + 0.22175 \times 10^{-14} r^4)[\%] \end{aligned} \tag{6.3}$$

The total dead time ($\mathrm{T_{dead,spa}}$) of the spallation cut can be estimated using the function of the position dependence and a normalization factor (5.0869) to average dead time as described in Eq. 6.4. The dead time distribution in SK-IV is shown in Fig. 6.9. As the results, about 20% on average of the dead time of the solar neutrino signals is reduced.

$$T_{\mathrm{dead,spa}} = 5.08691 \times T_{\mathrm{dead,z}} \times T_{\mathrm{dead,r^2}} \tag{6.4}$$

6.3.2 ^{16}N from stopping muons

The spallation derived from the long-lived isotope,^{16}N, also occurs in the low-energy region. ^{16}N decay emits the electron of 4.29 MeV and 10.42 MeV, and the gamma ray of 6.13 MeV as

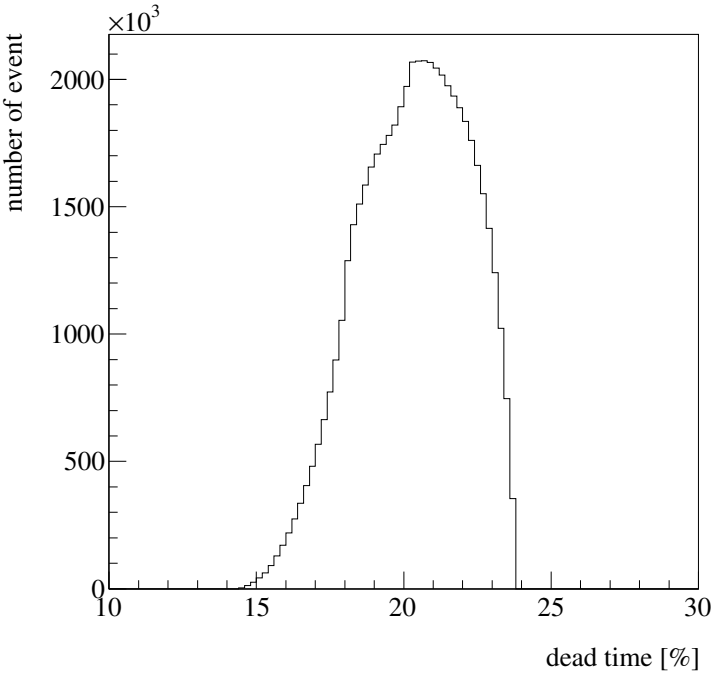

Figure 6.9: The distribution of the dead time due to the spallation cut. The dead time in SK-IV is about 20% on average.

shown in Table 6.2. Therefore, the long-lived spallation becomes one of the background for the solar neutrino analysis through the decay process ^{16}O(n,p)^{16}N in the low-energy region. ^{16}N is also made by the stopping muons as described in Eq. 6.5.

$$\mu + {}^{16}\mathrm{O} \rightarrow {}^{16}\mathrm{N} + \nu_{\mu} \tag{6.5}$$

The spallation of the ^{16}N from the stopping muons can not be removed by using the likelihood described in Section 6.3.1. In order to find these ^{16}N, stopping muons without a decay electron are looked for.

- Total number of charge of the muons < 800 p.e
- Distance of the low-energy event from the end point of the muon track < 350 cm
- Number of hit PMT of the low-energy electron within 50 ns time window(N_{50}) > 50

If all above conditions are met, the event is counted as the number of events resembling a decay electron. Secondly, the long-lived spallation events are selected from the above event candidates.

6.4 Ambient cut

In this step, the following cuts are applied. From this step, we recalculate energy and direction by using the accurate water transparency described in Fig. 4.1.

6.4.1 Tight event quality cut

Tight event quality cut is applied by using the event quality parameters for the vertex and the direction reconstructions described in Section 3.3.1. The events satisfying the following conditions are removed.

$$\begin{cases} (g_V)^2 - (g_A)^2 < 0.29 & (3.5\,\mathrm{MeV} \leq E < 5.0\,\mathrm{MeV}) \\ (g_V)^2 - (g_A)^2 < 0.25 & (5.0\,\mathrm{MeV} \leq E < 7.0\,\mathrm{MeV}) \end{cases}$$

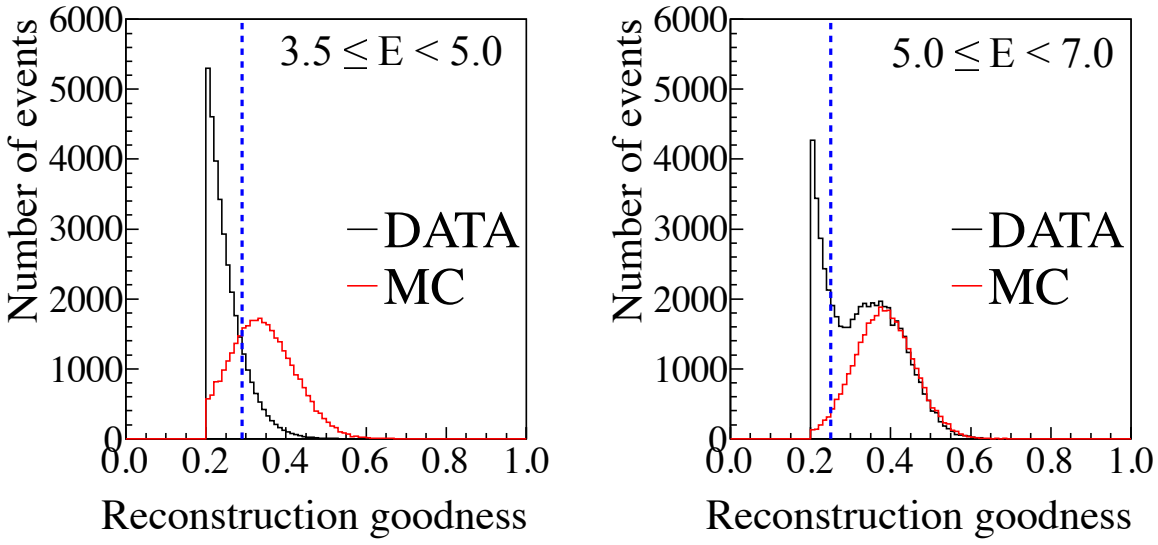

Figure 6.10: Distribution of the event quality parameters for the solar neutrino in the energy range of (Left) 3.5 MeV $\leq E <$ 5.0 MeV and (Right) 5.0 MeV $\leq E <$ 7.0 MeV after the pre-cut. Black line (data), red line (MC) and blue line (cut criteria) are shown in the distribution. The events in the left side from these criteria (blue line) are removed.

6.4.2 Small cluster cut

One of the cluster event is occurred by coincidence of the dark noise and the small clustering hits due to radioactivity from the ID PMT or the detector wall. The cluster size is relatively smaller than that of the flasher event as mentioned in Section 6.2.6 and is bigger than the solar neutrino event at the edge. Therefore, the small cluster events are distinguished by using two parameters r_{02} and N_{20}, and are remove. r_{02} is the radius containing more than 20% of the number of hit PMTs within 20 ns. $N_{20\mathrm{rawT}}$ is the number of hits within 20 ns time window.

For 3.5 MeV $\leq E <$ 4.5 MeV,

$$r02 \times \frac{N_{20\mathrm{rawT}}}{N_{\mathrm{eff}}} < 75.0, r^2 \geq 120\,\mathrm{m}^2 \text{ or } z < -300.0\,\mathrm{cm} \text{ or } z > 1300.0\,\mathrm{cm} \tag{6.6}$$

For 4.5 MeV $\leq E <$ 5.0 MeV,

$$r02 \times \frac{N_{\mathrm{20rawT}}}{N_{\mathrm{eff}}} < 75.0, r^2 \geq 155\,\mathrm{m}^2 \text{ or } z < -750.0\,\mathrm{cm} \tag{6.7}$$

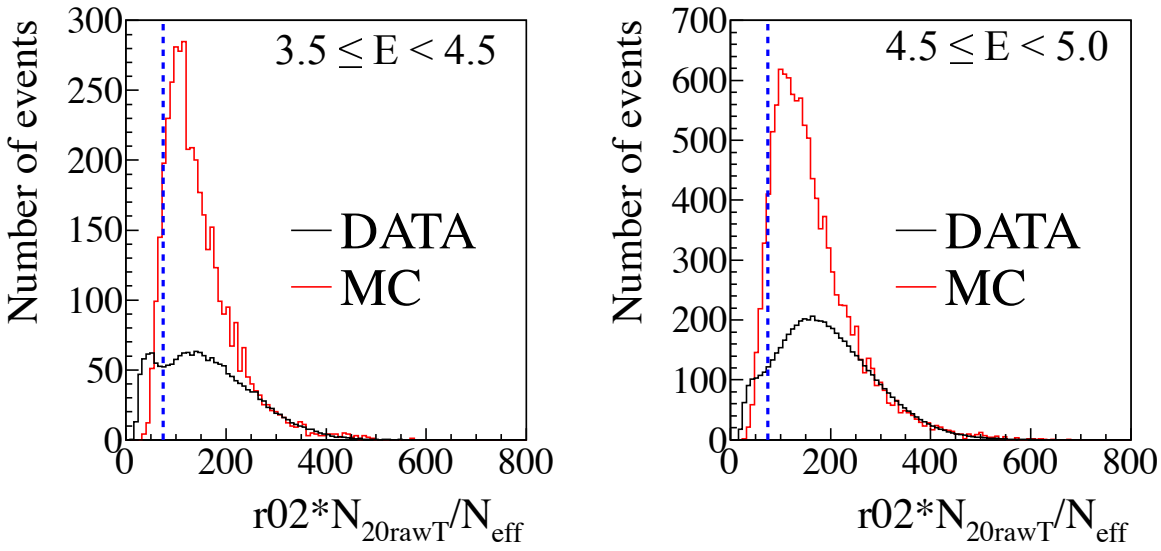

Figure 6.11: Distribution of the small cluster parameter for the solar neutrino in the condition of (Left) Eq. 6.6 and (Right) Eq. 6.7 after the loose fiducial volume cut (2.0 m). Black line (data), red line (MC) and blue line (cut criteria) are shown in the distribution. The events in the left side from these criteria (blue line) are removed.

6.4.3 Hit pattern cut

Since the spallation emits multiple gamma/beta-rays, the Cherenkov ring pattern of the spallation event is differ from that of the recoil electron for the solar neutrino event. Therefore, a likelihood of the hit pattern of the Cherenkov light is estimated in the event reconstruction. The likelihood function for the hit pattern is represented by the following equation.

$$\mathcal{L}_{\mathrm{pattern}}(E, \vec{v}) = \frac{1}{N_{50}} \sum_{i}^{N_{50}} \log(pdf_i(E, \cos\theta_{\mathrm{PMT}}, f_{\mathrm{wall}})) \tag{6.8}$$

The likelihood function is a log likelihood function of the probability density function of energy, $\cos\theta_{\mathrm{PMT}}$ and f_{wall}. N_{50} is the effective number of hits within 50 ns time window. The parameters, θ_{PMT} and f_{wall}, are explained in Section 3.3.2 and illustrated in Fig. 3.16. The probability density function is calculated by the MC simulation. The events are reduced as the background event when the likelihood is matched with the following conditions. The criteria are determined from the distribution of the likelihood as shown in Fig. 6.12.

$$\begin{cases} \mathcal{L}_{\mathrm{pattern}} < -1.88 & (6.0\,\mathrm{MeV} \leq E < 7.5\,\mathrm{MeV}) \\ \mathcal{L}_{\mathrm{pattern}} < -1.86 & (7.5\,\mathrm{MeV} \leq E < 11.5\,\mathrm{MeV}) \\ \mathcal{L}_{\mathrm{pattern}} < -1.95 & (11.5\,\mathrm{MeV} \leq E) \end{cases}$$

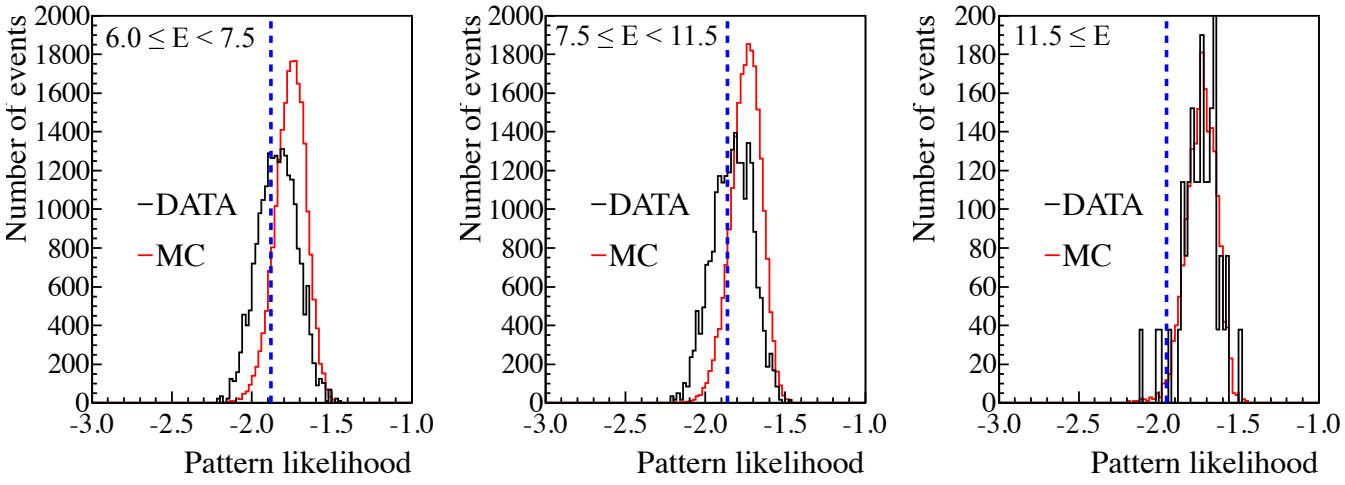

Figure 6.12: The distributions of the hit pattern likelihood function after the spallation cut. The left figure is in 6.0 MeV to 7.5 MeV, the center figure is in 7.5 MeV to 11.5 MeV and the right figure is above 11.5 MeV. Black line represents the distribution for real data and red line represents the distribution for the MC simulation in these figures. Blue dotted line represents cut criteria of the pattern likelihood in each energy region, -1.88, -1.86 -1.95, respectively.

6.5 External event cut

External gamma-ray from the material of the SK detector and the rock outside of the SK detector is one of the background sources in the low-energy region on the solar neutrino analysis. Therefore, the external background distributes close to the SK detector wall basically and is reduced by using the event quality parameters, $d_{\rm eff}$ and $\rm P_{wall}$ as shown in Fig. 3.16. In this step, the tight external cuts are applied to the solar neutrino data as shown in Fig. 6.13. The conditions of the tight external cuts are difference at each energy region and the position on the detector wall as follows.

$$\begin{cases} d_{\rm eff} < 400.0 \text{ cm} & (7.5\,\text{MeV} \leq E\,) \\ d_{\rm eff} < 650.0 \text{ cm} & (5.0\,\text{MeV} \leq E < 7.5\,\text{MeV}) \\ d_{\rm eff} < 1000.0 \text{ cm} & (3.5\,\text{MeV} \leq E < 5.0\,\text{MeV},\ \text{Top region}) \\ d_{\rm eff} < 1300.0 \text{ cm} & (3.5\,\text{MeV} \leq E < 5.0\,\text{MeV},\ \text{Bottom region}) \\ d_{\rm eff} < 1200.0 \text{ cm} & (3.5\,\text{MeV} \leq E < 5.0\,\text{MeV},\ \text{Barrel region}) \end{cases}$$

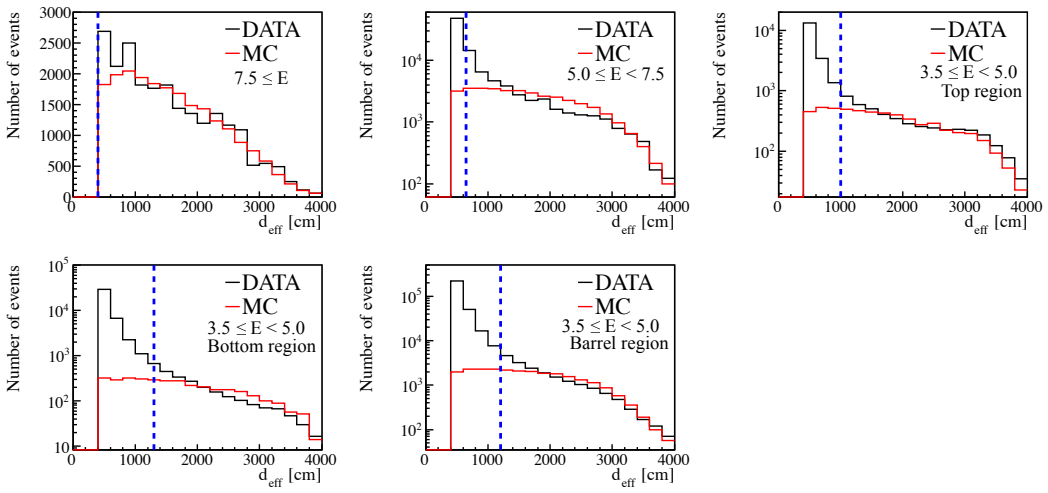

Figure 6.13: The distributions of d_{eff} defined in Fig. 3.16 at each energy region and the position in the detector after the hit pattern cut.

6.6 Final reduction

In the final reduction, tight fiducial volume cut is applied.

6.6.1 Tight fiducial volume cut

Background events still remain near the SK detector wall after the above reductions. Therefore, the tight fiducial volume cut is applied to the data finally in the low-energy region from 3.5 MeV to 5.0 MeV. The criteria line for the tight fiducial volume cut differ by each energy range as shown in Fig. 6.14. The events satisfying the following conditions are removed.

$$r^2 + \frac{150}{11.75^4} \times |z - 4.25|^4 > 150\,\mathrm{m}\,(3.5\,\mathrm{MeV} \leq E < 4.5\,\mathrm{MeV}) \tag{6.9}$$

$$z < -7.5\,\mathrm{m}\,(4.5\,\mathrm{MeV} \leq E < 5.0\,\mathrm{MeV}) \tag{6.10}$$

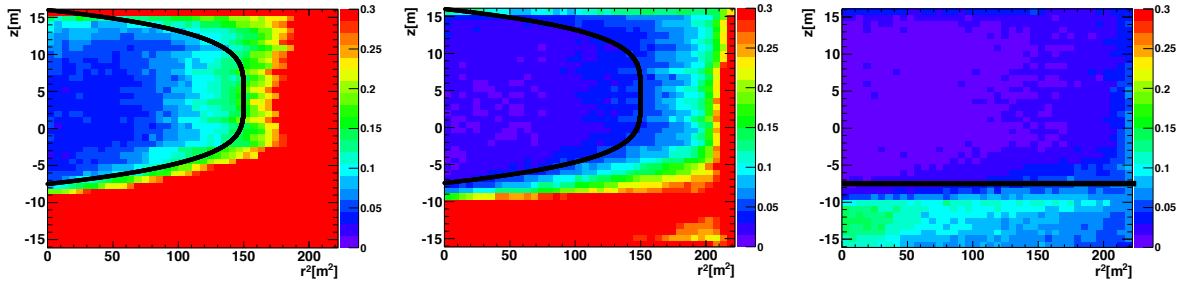

Figure 6.14: The vertex distribution of 3.0-4.5 MeV (Left), 4.0-4.5 MeV (Center), 4.5-5.0 MeV (Right). The events of right side are applied the tight fiducial volume cut (black line) of the left and the center figures and of lower side of the right figure after the external event cut.

After this cut, the final data sample for the solar neutrino analysis is obtained.

6.7 Summary of the reduction step of the solar neutrino analysis

The real data for the solar neutrino analysis is selected by the several reductions above. The every spectrum of each reduction step for this solar neutrino analysis is shown in Fig. 6.15. Table 6.3 shows the number of events after the each data reduction, and Table 6.4 shows the reduction efficiency of the MC simulation.

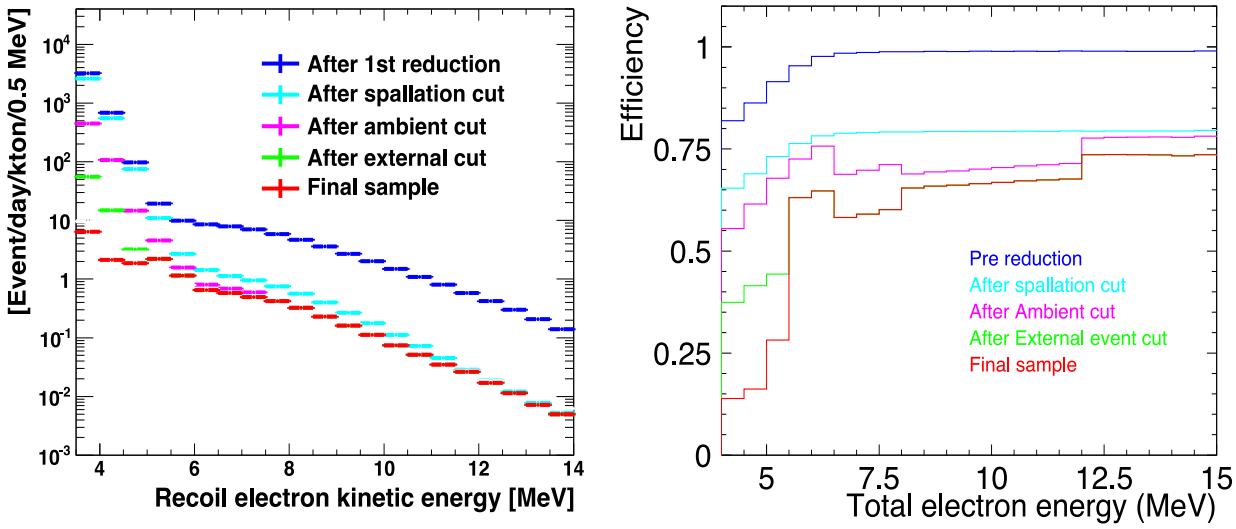

Figure 6.15: (Left) Reduction step for the solar data analysis. (Right) Reduction efficiency for the MC simulation of ^{8}B solar neutrinos.

Table 6.3: Number of events after the data reductions. The total number of events represents in the table after the fiducial volume cut

Index	$3.5 \leq E < 6.0$ MeV		$6.0 \leq E < 19.5$ MeV	
	$\times 10^6$	Reduction ratio[%]	$\times 10^6$	Reduction ratio[%]
Total number of event	261.4	100.0	3.071	100.0
After 1st reduction	259.0	99.08	3.065	99.82
After spallation cut	209.0	79.95	0.3860	12.57
After ambient cut	36.85	14.10	0.2294	7.468
After external cut	49.47	1.892	0.2066	6.727
Final sample	5.196	0.1988	0.2066	6.727

Table 6.4: The reduction efficiency of the MC simulation of ^{8}B solar neutrinos. The total number of the generated MC events before the energy cut is 281.7 $\times 10^6$ events.

Index	$3.5 \leq E < 6.0$ MeV		$6.0 \leq E < 19.5$ MeV	
	$\times 10^6$	Efficiency[%]	$\times 10^6$	Efficiency[%]
Total number of event	41.56	100.0	48.48	100.0
After 1st reduction	36.70	88.30	47.79	98.59
After spallation cut	29.33	70.58	38.29	78.99
After ambient cut	26.50	63.75	34.46	71.09
After external cut	19.02	45.77	30.76	63.45
Final sample	11.91	28.64	29.76	61.39

Figure 6.16 shows the time variation of the event rate after applying all the solar neutrino reduction. The plots for the time variation of the event rates are divided in the energy region: 3.5-4.0 MeV, 4.0-4.5 MeV, 4.5-5.0 MeV, 5.0-19.5 MeV. Each value in these plots is obtained by taking an average during 5 days.

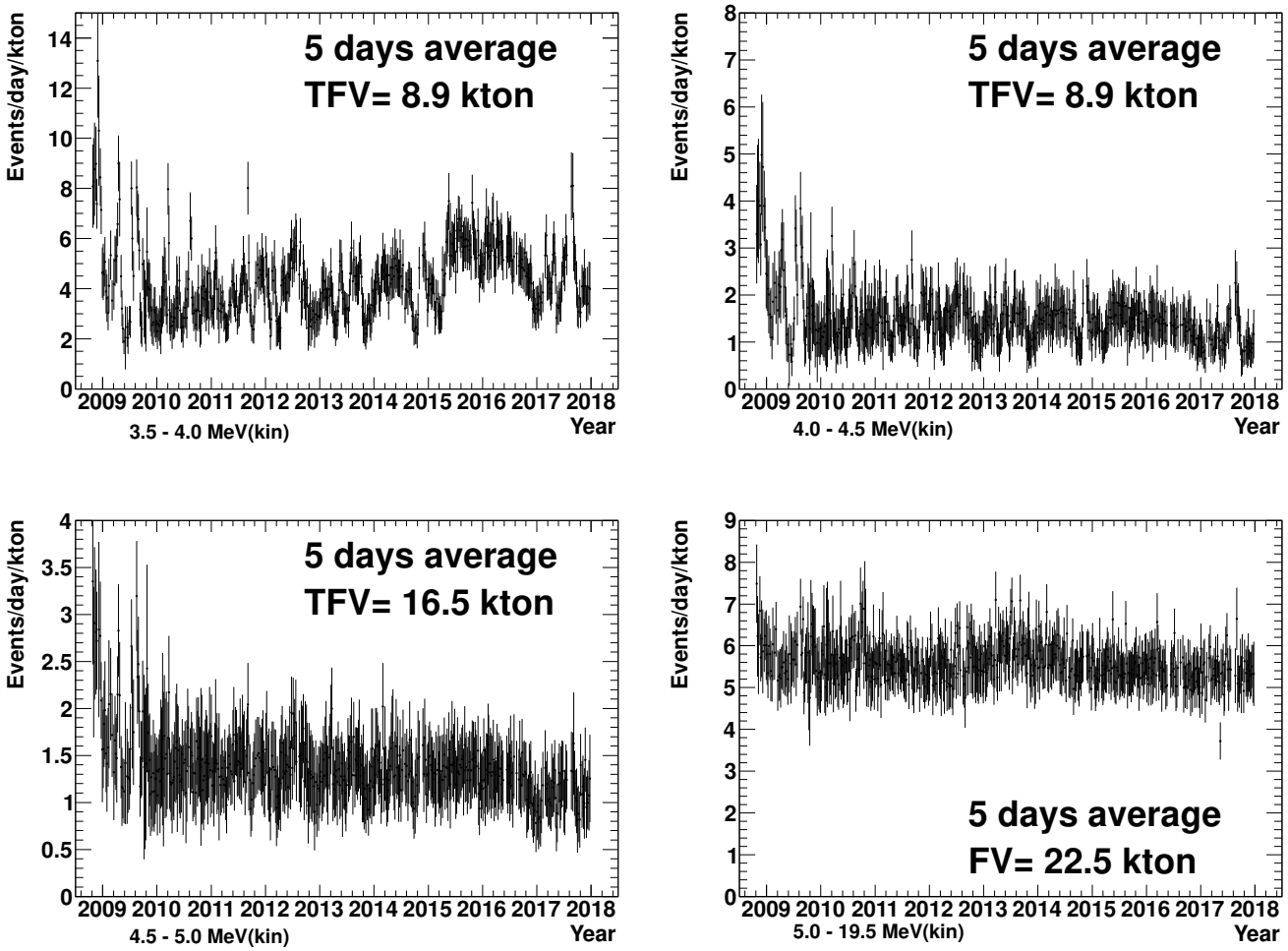

Figure 6.16: The time variation of the event rate of the final data sample in SK-IV

Chapter 7

Signal extraction method

As mentioned in Chapter 4, the MC simulation can not estimate the background in the solar neutrino analysis. A probability density function for the solar neutrino signal is estimated after the events are generated by the MC simulation. On the other hand, although, the event selection is applied to the real data as described in Chapter 6, the final data sample still includes a lot of background. The reason is that the reduction process can't exclude all backgrounds related to the solar neutrino. Mainly Rn and the muon spallation are considered as the remaining backgrounds. The main purpose of this section is to explain the signal extraction for the solar neutrino from the final data sample by using the probability density function.

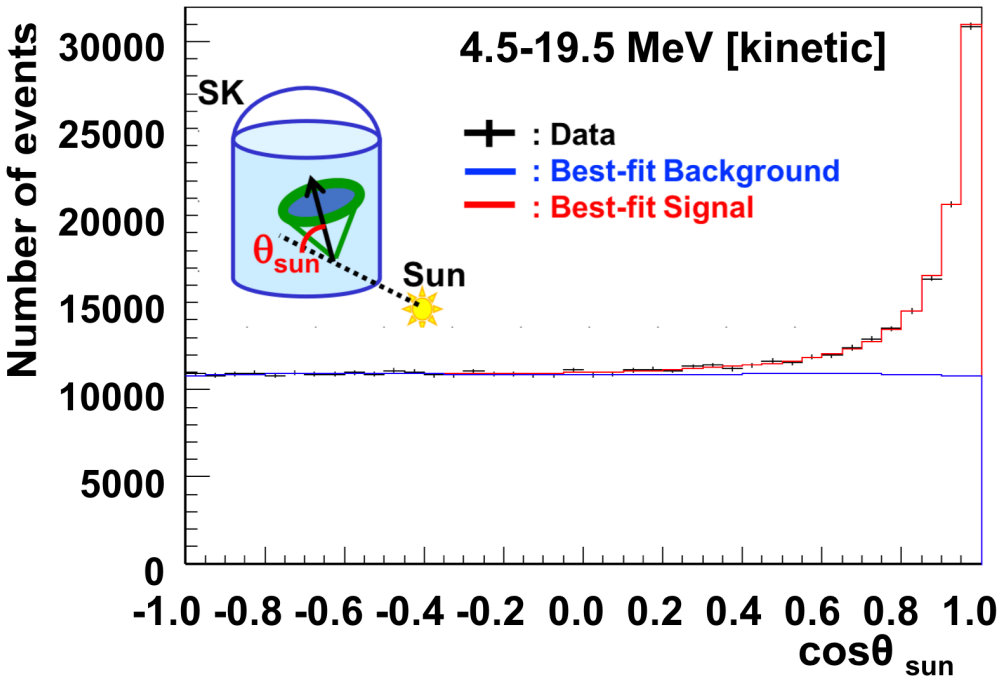

Figure 7.1: The distribution of the $\cos\theta_{\rm sun}$ distribution from 4.5 to 19.5 MeV in total livetime 2860 days.

Figure. 7.1 shows the $\cos\theta_{\rm sun}$ distribution from 4.5 to 19.5 MeV of the kinetic energy of the recoil electron. $\theta_{\rm sun}$ represents the angle between the direction from the Sun and the reconstructed direction as illustrated in the figure. Black cross represents the final data sample, and red line shows the obtained best-fit signal in the figure. The events under the best-fit background (blue line) is the background remaining after the event selection. The traveling direction of the recoil electron interacting with the solar neutrino is correlated with the solar direction. Therefore, smooth peak appears towards $\cos\theta_{\rm sun} = 1.0$ corresponding to the solar direction.

7.1 Signal extraction

Signal and background shape are estimated using the an extended maximum likelihood function fit to the $\cos\theta_{\rm sun}$ distribution is used from 3.5 MeV to 19.5 MeV in kinetic energy. The likelihood function is defined as:

$$\mathcal{L} = \mathrm{e}^{-\left(\sum_i B_i + S\right)} \prod_{i=1}^{N_{\rm bin}} \prod_{j=1}^{N_{{\rm MSG}_i}} \prod_{k=1}^{n_{ij}} \left(B_{ij} \cdot b_{ijk}(E, \theta_{\rm sun}) + S \cdot Y_{ij} \cdot s_{ijk}(E, \theta_{\rm sun})\right) \tag{7.1}$$

- $N_{\rm bin}$: Total number of energy bins
  The kinetic energy from 3.5 MeV to 19.5 MeV is divided into twenty three, $N_{\rm bin} = 23$, and the each width of the energy bin is differ as below.

$$\begin{cases} 0.5\,\mathrm{MeV/bin} & (\ 3.5 \leq E < 13.5\,\mathrm{MeV}) \\ 1.0\,\mathrm{MeV/bin} & (13.5 \leq E < 15.5\,\mathrm{MeV}) \\ 4.0\,\mathrm{MeV/bin} & (15.5 \leq E < 19.5\,\mathrm{MeV}) \end{cases}$$

- $N_{{\rm MSG}_i}$: Total number of MSG bins
  The MSG parameter from 0.0 to 1.0 is divided into three bins of the i-th energy bin, $N_{{\rm MSG}_i} = 3$, and the each width of the MSG bin is differ as below.

$$\begin{cases} 0.00 < \mathrm{g_{MS}} < 0.35 & (E < 7.5\,\mathrm{MeV}) \\ 0.35 < \mathrm{g_{MS}} < 0.45 & (E < 7.5\,\mathrm{MeV}) \\ 0.45 < \mathrm{g_{MS}} < 1.00 & (E < 7.5\,\mathrm{MeV}) \\ 0.00 < \mathrm{g_{MS}} < 1.00 & (E \geq 7.5\,\mathrm{MeV}) \end{cases}$$

- n_i : Total number of events in the i-th energy bin.
- b_{ijk}: The background probability density function for k-th event in j-th MSG bin in i-th energy bin
- s_{ijk}: The signal probability density function for k-th event in j-th MSG bin in i-th energy bin
- Y_{ij} : The fraction of signal events in the i-th energy bin based on the MC simulation.
- B_i: Free parameter corresponding to the number of background events in the i-th energy bin

- S : Free parameter corresponding to the total number of solar neutrino events in all energy bins

The b_{ijk} (Section 7.1), the s_{ijk} (Section 7.2) and the Y_{ij} (Section 7.3) are input parameters of the maximum likelihood function. The free parameters, S and B_i, represent just the number of signal and background, respectively. These parameters are obtained by maximizing the likelihood.

7.2 Background probability density function (b_{ijk})

The probability density function for the background is estimated by using the final data sample. The background shape is not completely flat as shown in Fig. 7.1 because the SK detector is not spherical and has a non uniform background event distribution. It is assumed that the background is not correlated with the solar direction. Therefore, the background angular distribution should only depend on the direction with respect to the detector coordinate system. The background shape PDF is generated by the following steps.

1. Create the solar direction ($\cos\theta_{\rm sun}$) distribution of the final data sample. The distribution is divided by 100 bins from $\cos\theta_{\rm sun}$ = -1 to 1.

2. Calculate background weights depending on the $\cos\theta_{\rm sun}$ at each bin. For example, if a event has a large $\cos\theta_{\rm sun}$, the weight is a small while if it has a small $\cos\theta_{\rm sun}$, the weight closes with 1.

3. Create the zenith angle distribution ($\cos\theta_{z,\rm eve}$) and the azimuthal distribution (ϕ) shown in Fig. 3.3 of the real data at each energy bin as shown in Fig. 7.2.

4. Assign the background weight to both of the distributions event-by-event. The weighted zenith angle distribution and the weighted azimuthal distribution are removed a effect of the solar direction.

5. A polynomial fitting applies to the weighted distributions as shown in Fig. 7.2. Then, a spherical direction distribution for the background shape is generated from the two distributions assuming there are no correlations.

6. Using the polynomial functions, the $\cos\theta_{\rm sun}$ distribution is made event-by-event. Then, the polynomial function fitting to the $\cos\theta_{\rm sun}$ distribution is estimated. The polynomial function is the probability density function for the background shown the blue line in Fig. 7.1. The polynomial functions consisted of ten coefficients are created for each energy bin and MSG bin

$$b_{ijk} = \left(\sum_{k=0}^{8} c_{i,k} \cos^k \theta_{{\rm sun}(i,j)} \right) / c_{i,9} \tag{7.2}$$

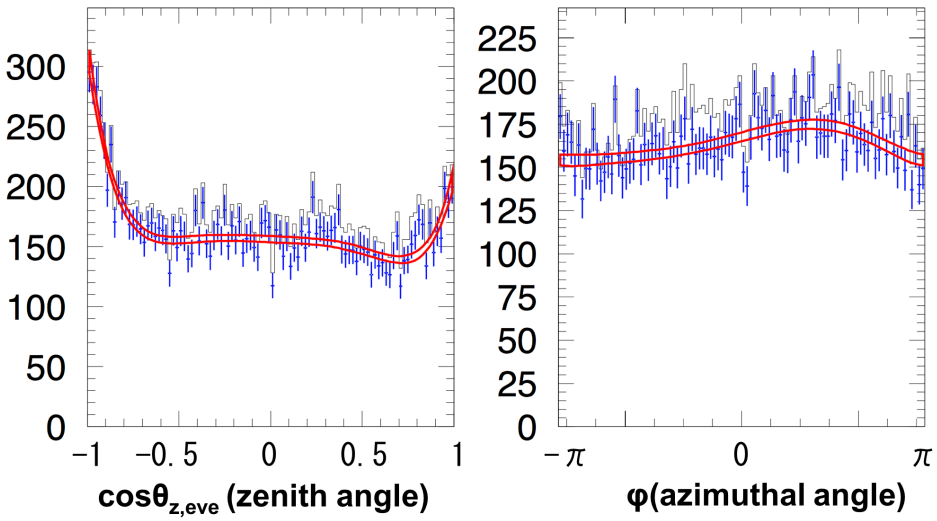

Figure 7.2: The zenith angle distribution ($\cos\theta_{z,\mathrm{eve}}$) and the azimuthal angle distribution (ϕ) in 5.0 MeV to 6.0 MeV. Black line shows the data, blue plots show the re-weighted data and red lines are 1σ band of the polynomial fitting function.

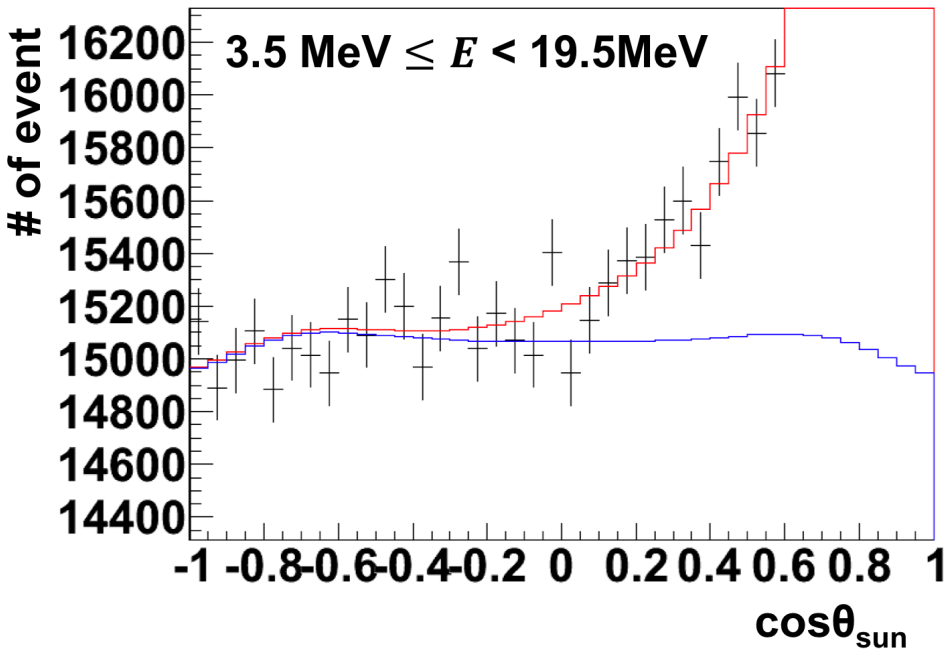

Figure 7.3: The probability density function of background (b_{ijk}). The plots show the data, the blue line shows the background shape probability density function and the red line shows the signal probability density function described in Section 7.3.

7.3 Signal probability density function (s_{ijk})

A probability density function for the signals is obtained by the expected solar neutrino MC events. The function consists of three exponential functions and Gaussian function:

1. Use the reconstructed solar neutrino MC event in Section 4.2.
2. Apply the same reduction cuts as data to the reconstructed solar neutrino MC events, then make solar neutrino MC final sample.
3. Create the solar direction ($\cos\theta_{\rm sun}$) distribution of the final MC sample.
4. The $\cos\theta_{\rm sun}$ distribution is fitted by triple exponential and Gaussian function
5. The result of the fitting is the probability density function of signal consisted of nine coefficients as shown in Fig. 7.4

$$s_{ijk} = \sum_{k=0}^{2} \exp(c_{i,2k} + c_{i,2k+1}\cos\theta_{{\rm sun},ijk}) + c_{i,6}\exp\left(\frac{c_{i,7}-x}{2c_{i,8}}\right)^2 \tag{7.3}$$

This process is also used for estimating the systematic uncertainty of total neutrino flux as will be described in Chapter 8.

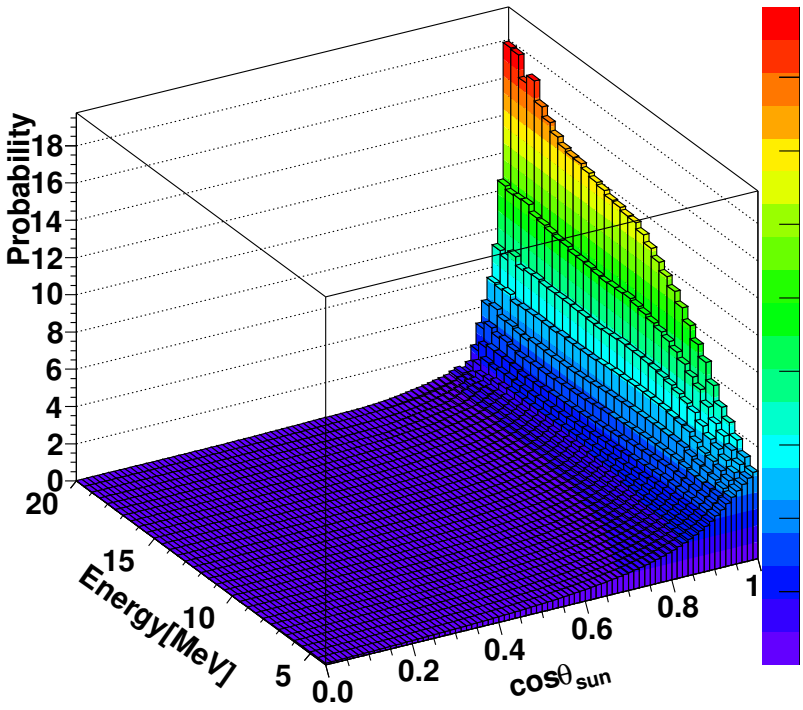

Figure 7.4: The probability density function of the solar neutrino MC angular distribution. The hight shows the probability density in 3.5 - 19.5 MeV energy region and $\cos\theta_{\rm sun}$ is shown in 0.0 to 1.0 in the figure.

7.4 Signal fraction of each energy bin (Y_{ij})

A fraction of the energy of the signal is assigned by using the expected energy spectrum. The expected energy spectrum is obtained from the solar neutrino MC simulation as the results of Section 4.2. The signal fraction (Y_{ij}) of each energy bin is estimated from the energy spectrum shown in Fig. 7.5, which is the energy distribution of the solar neutrino MC final sample. The signal fraction is calculated the number of the signals of each energy bin divided by the total number of the signals.

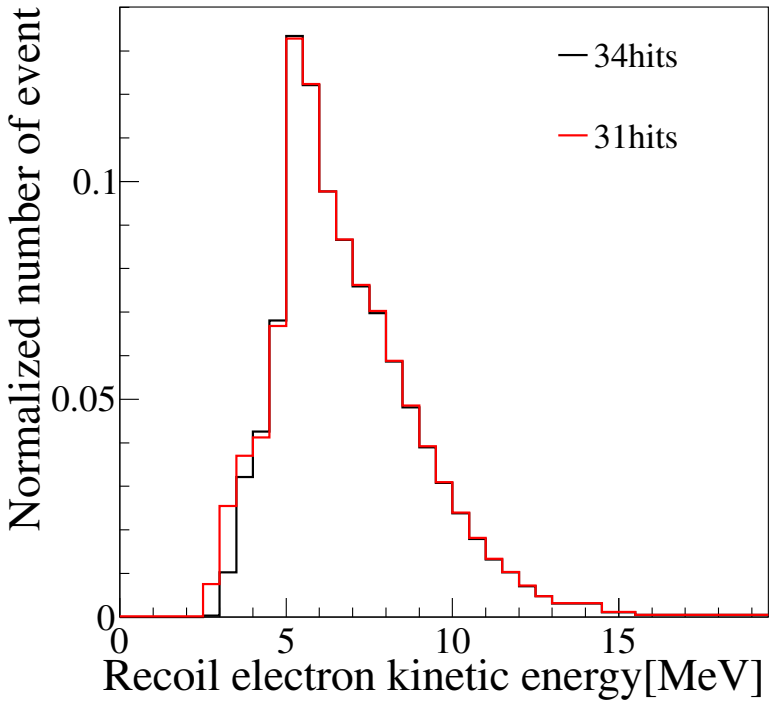

Figure 7.5: The expected energy spectrum for ^{8}B solar neutrino. The vertical axis shows the event rate of the ^{8}B neutrino and the horizontal axis shows the recoil electron kinetic energy. The signal fraction of each energy bin is obtained dividing the event rate of the each bin by total number of event.

Chapter 8

Systematic Uncertainty

In this section, systematic uncertainties on the total neutrino flux and on the energy spectrum of the recoil electron are described. They are mainly classified in two kinds of systematic uncertainties, the energy correlated and the energy uncorrelated. The energy correlated systematic uncertainties are obtained by counting the number of events in the solar neutrino MC simulation with artificially shifted energy scale, energy resolution and ^{8}B solar neutrino energy spectrum.

8.1 Systematic uncertainty on the total neutrino flux

In the first three sections, the energy correlated systematic uncertainties are described. The methods for estimating energy uncorrelated systematic uncertainties from 3.5 MeV to 19.5 MeV are described from Section 8.1.4.

8.1.1 Energy scale

The combined systematic uncertainty in the absolute energy scale is 0.53% in SK-IV as described in Section 5.5. In order to estimate the uncertainty on the total flux, the electron energies are shifted by the uncertainty of the energy scale in the signal extraction.

As a result, the systematic uncertainty of the total flux is estimated $\pm 1.0\%$ in the energy range due to the systematic uncertainty on the energy scale.

8.1.2 Energy resolution

The systematic uncertainty of the total flux in the energy resolution by using the resolution obtained from the LINAC calibration as described in Section 5.3.4. The difference, which corresponds to the uncertainty of the energy resolution, between the resolution of the data and the MC simulation is calculated as shown in Fig. 8.1. The uncertainties are combined in the entire LINAC year at each LINAC energy (blue marker in Fig. 8.1). Next, the combined systematic uncertainties are fitted by a quadratic function described in Eq. 8.1.

$$f = -1.278 + 0.499\,E - 0.014\,E^2 \tag{8.1}$$

E is the recoil electron kinetic energy. The χ^2/d.o.f of the fitting function is 0.36/4 (probability 98.7%). The fitting function is shown as red line in Fig. 8.1. The signal fraction (Y_{ij}) is shifted

by the systematic uncertainty of the energy resolution obtained from the fitting function in the signal extraction. As a result, the systematic uncertainty of the total flux is estimated ±0.1% in the energy range from 3.5 MeV to 19.5 MeV due to the uncertainty on the energy resolution.

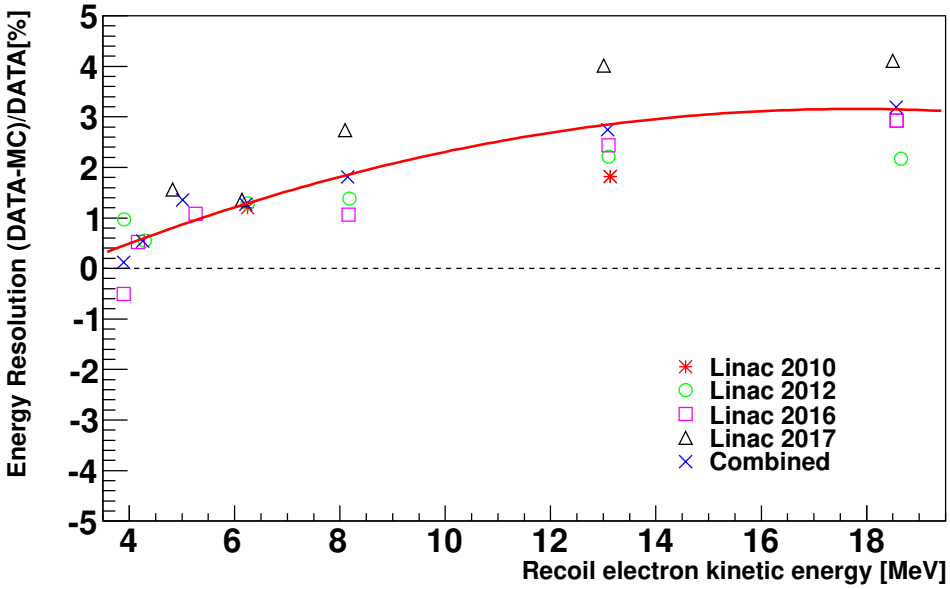

Figure 8.1: The difference of the data and the MC simulation of energy of the LINAC calibration. The energy resolution is calculated by peak value of energy distribution divided by standard deviation. The marker(color) shows the LINAC calibration year. Red line is a fitting quadratic function to the combined uncertainty (blue marker) of energy resolution.

8.1.3 ^{8}B solar neutrino spectrum

The ^{8}B neutrino spectrum is estimated from the α-spectrum measurement at a ground experiment [36]. In the ground experiment, the neutrino energy emitted from the β^+ decay of ^{8}B is estimated by measuring the energy of α-particles. The α-particles are emitted from ^{8}Be* which is a decay production of the ^{8}B reaction as shown in Fig. 2.5. The systematic uncertainty on the ^{8}B neutrino spectrum in the α-measurement is affected to the ^{8}B solar neutrino flux estimation in SK. The systematic uncertainty in the ^{8}B solar neutrino spectrum is calculated by using the signal fraction (Y_{ij}) shifted by the uncertainty of the ^{8}B neutrino spectrum estimated in [36]. The obtained total neutrino flux uncertainty due to the ^{8}B solar neutrino spectrum is ±0.4%.

8.1.4 Trigger efficiency

The systematic uncertainty of the trigger efficiency means the position dependence of the trigger efficiency in the fiducial volume. The uncertainties are estimated by comparing data and the MC simulation of the Ni calibration. There are 9 measurement points, which representative 9 volumes shown in Fig. 8.2 in the tight fiducial volume in the energy region from 3.5 MeV to 5.5 MeV.

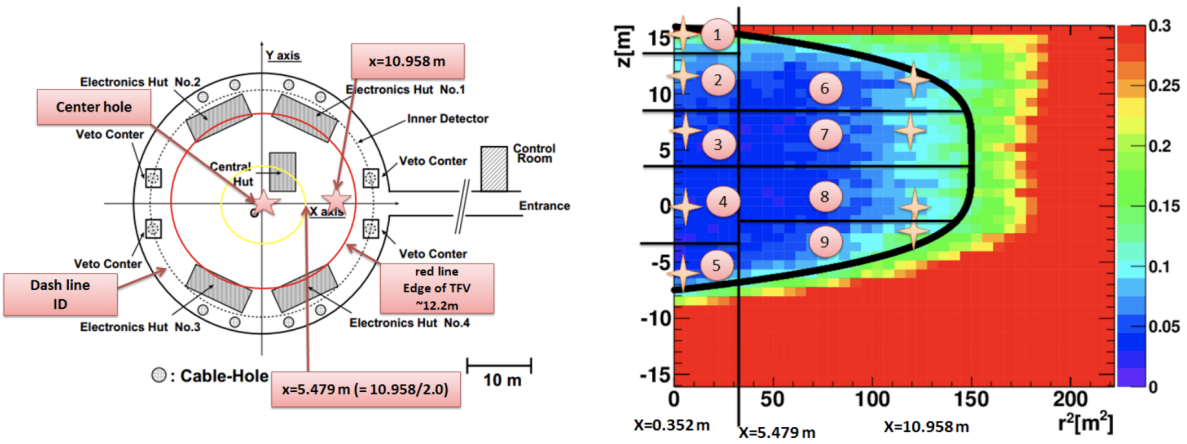

Figure 8.2: Measurement positions for the systematic uncertainty of the trigger efficiency [33].

1. The trigger efficiencies of each volume are estimated by using the following Eq. 8.2.

$$\text{Trigger Efficiency} = \frac{\sum \mathrm{e}_i \mathrm{V}_i}{\sum \mathrm{V}_i} \tag{8.2}$$

   V_i is the i-th (i =1-9) volume shown in Fig. 8.2 and e_i is the trigger efficiency of i-th volume.

2. The trigger efficiencies of the data and the MC simulation calculated in the step.1 are compared. The difference is the systematic uncertainty of the trigger efficiency. The systematic uncertainties of the trigger efficiency of each period for the SLE trigger 31 hits and 34 hits are shown as follows.

   SLE 34 hits (Oct. 2008 - Apr. 2015)

$$\begin{cases} -8.09 \pm 0.32\,\% & (3.5\,\mathrm{MeV} \leq E < 4.0\,\mathrm{MeV}) \\ -1.00 \pm 0.27\,\% & (4.0\,\mathrm{MeV} \leq E < 4.5\,\mathrm{MeV}) \\ 0.00\,\% & (4.5\,\mathrm{MeV} \leq E). \end{cases}$$

   SLE 31 hits (May 2015 - Dec. 2017)

$$\begin{cases} -1.28 \pm 0.26\,\% & (3.5\,\mathrm{MeV} \leq E < 4.0\,\mathrm{MeV}) \\ -0.69 \pm 0.19\,\% & (4.0\,\mathrm{MeV} \leq E < 4.5\,\mathrm{MeV}) \\ 0.00\,\% & (4.5\,\mathrm{MeV} \leq E). \end{cases}$$

3. Correct the event rate of solar neutrino MC (Y_{ij}) and estimate the total flux by the signal extraction in the energy range from 3.5 MeV to 19.5 MeV.

The systematic uncertainty of the energy spectrum on the trigger efficiency estimated by using the uncertainties is

$$\begin{cases} +6.4/-5.6\,\% & (3.5\,\mathrm{MeV} \leq E < 4.0\,\mathrm{MeV}) \\ \pm 0.9\,\% & (4.0\,\mathrm{MeV} \leq E < 4.5\,\mathrm{MeV}) \\ 0.0\,\% & (4.5\,\mathrm{MeV} \leq E). \end{cases}$$

As the trigger efficiency more than 4.5 MeV is 100%, the systematic uncertainty on the trigger efficiency is 0.0%. The systematic uncertainty on the trigger efficiency gives a fluctuation to the livetime. Therefore, we consider the livetime in this estimation. The resulting the systematic uncertainty on the total flux due to the trigger efficiency is ±0.1%.

8.1.5 Angular resolution

The systematic uncertainty in the angular resolution is calculated by using the LINAC data and the MC simulation. The systematic uncertainty is estimated by the following steps:

1. Calculate difference between the data and the MC simulation as described in Section 5.3.4.
2. The systematic uncertainty in the angular resolution is calculated by (data - MC)/data × 100% as shown on the vertical axis in Fig. 8.3.
3. The systematic uncertainties are combined by the sum of square in the entire LINAC year at each LINAC energy (blue marker in Fig. 8.3).
4. Shift artificially the reconstructed direction by the combined systematic uncertainties of the solar neutrino MC events, then remake (s_{ijk}), then redo signal extraction.
5. Compare between the original flux and the shifted flux. The difference is the systematic uncertainty on the total flux in angular resolution.

As a result, the systematic uncertainty on the total flux in the angular resolution is estimated to be ±0.1%.

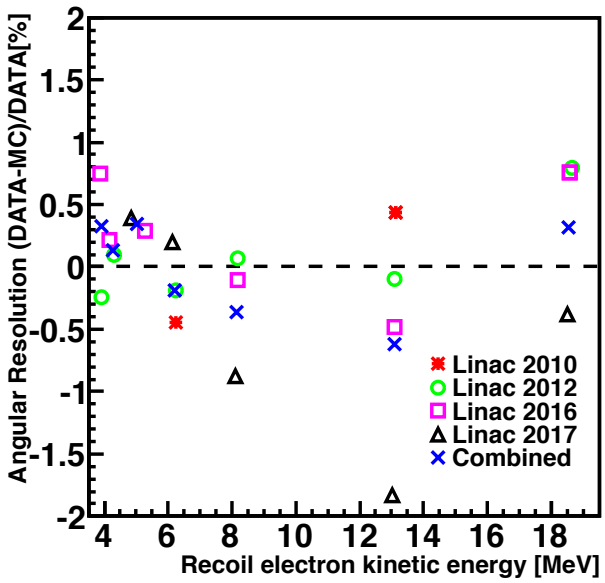

Figure 8.3: The difference of data and the MC simulation of the angular distribution of the LINAC calibration. The marker (color) shows the LINAC calibration year. The systematic uncertainty of the angular resolution between the combined plots (blue) is estimated by interpolation.

8.1.6 Reconstruction goodness

The systematic uncertainty of the event quality is estimated by using the LINAC calibration by the following steps:

1. Count the number of events passing the reduction cuts similar to the solar neutrino analysis, for example, fiducial volume cut and energy cut : $E > 3.5$ MeV and $E < 24.5$ MeV.

2. The systematic uncertainty of the reconstruction goodness cut is estimated by (data - MC)/data $\times$ 100% of the difference of the surviving number of event before and after the event quality cut described in Section 6.4.1 of the goodness distribution in Fig. 8.4.

3. Combined systematic uncertainties at each recoil energy is calculated the sum of square of all LINAC year (blue marker in Fig. 8.5).

4. Correct the event rate of solar neutrino MC (Y_{ij}) and estimate the total flux by the signal extraction in the energy range from 3.5 MeV to 19.5 MeV.

As a result, the combined systematic uncertainty due to reconstruction goodness cut is estimated $\pm$0.5%.

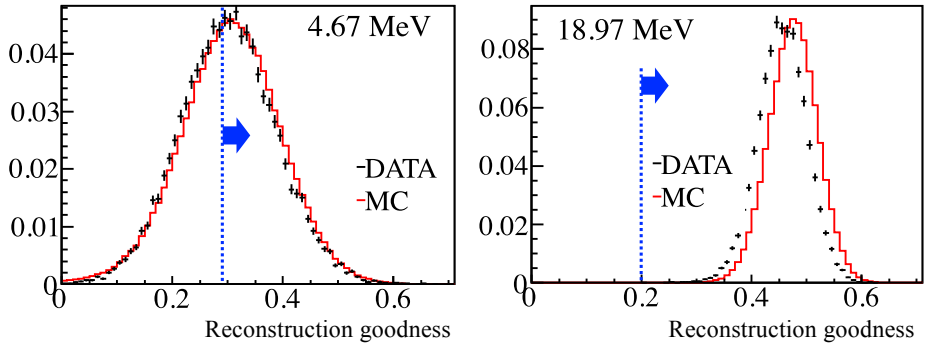

Figure 8.4: The distribution of the data (black line) and the MC simulation (red line) of the reconstruction goodness. The dotted blue lines show the reconstruction goodness cut criteria.

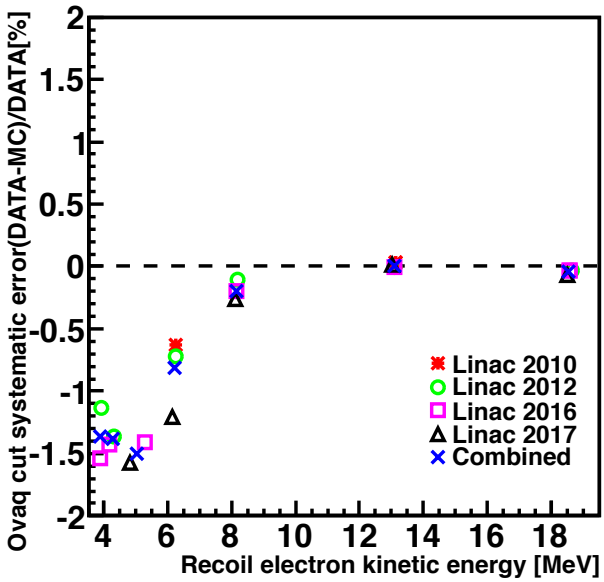

Figure 8.5: The difference of the data and the MC simulation for the reconstruction goodness. The marker (color) shows the LINAC calibration year. The systematic uncertainty of the reconstruction goodness cut between the combined plots (blue) is estimated by interpolation.

8.1.7 Small hit cluster

The systematic uncertainty on the small hit cluster cut described in Section 6.4.2 is estimated using the DT calibration. The small hit cluster occurred by event at the edge as described in Section 6.4.2. Therefore, the uncertainty on total flux due to the small hit cluster is calculated near the detector wall by the DT calibration. As a result, the systematic uncertainty is estimated $\pm 0.4\%$.

8.1.8 Hit pattern

The systematic uncertainty of the hit pattern cut described in Section 6.4.3 is estimated by the LINAC calibration:

1. Count the number of events thought out the reduction cut similar to the solar neutrino analysis, for example, fiducial volume cut and energy cut : $E > 3.5$ MeV and $E < 24.5$ MeV.

2. The uncertainty of the hit pattern cut is calculated by (data - MC)/data $\times$ 100% of the difference of the surviving number of event before and after reduction cut of the pattern likelihood distribution in Fig. 8.6.

3. Combined systematic uncertainty at each recoil energy is calculated the sum of square of all LINAC year (blue marker in Fig. 8.7) .

4. Correct the event rate of solar neutrino MC (Y_{ij})and estimate the total flux by the signal extraction in the energy range from 3.5 MeV to 19.5 MeV.

As a result, he combined systematic uncertainty due to the hit pattern cut is estimated $\pm 0.4\%$.

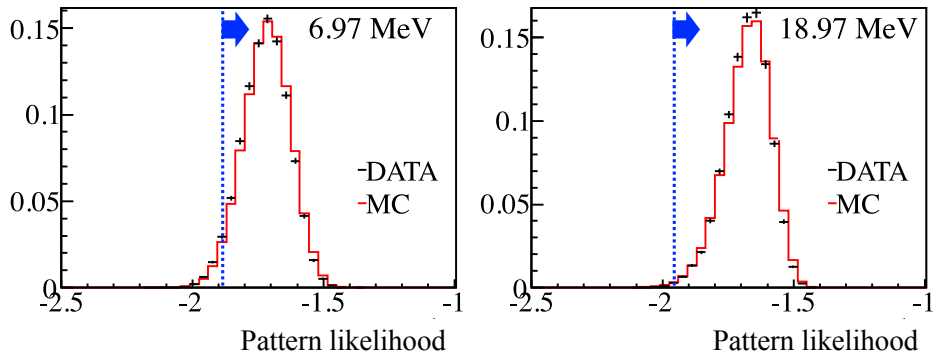

Figure 8.6: The distribution of the data (black line) and the MC simulation (red line) of the hit pattern likelihood. The dotted blue lines show the hit pattern cut criteria.

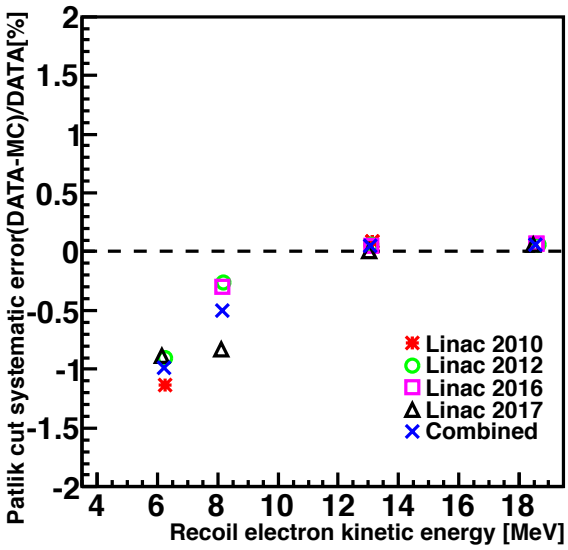

Figure 8.7: The difference of the data and the MC simulation for the hit pattern. The marker (color) shows the LINAC calibration year. The systematic uncertainty of the hit pattern cut between the combined plots (blue) is estimated by interpolation.

8.1.9 External event cut

The systematic uncertainty from the external event cut is estimated by using the parameter d_{eff} illustrated in Fig. 3.16. The details of the external event cut are described in Section 6.5. First, the reconstructed vertex and direction are artificially shifted in the solar neutrino MC simulation (Fig. 8.8) since d_{eff} depends on the reconstructed vertex and direction. The amount of the artificially shift of the reconstructed direction is the systematic uncertainty in the angular resolution. Then, the amount of the artificially shift of the reconstructed vertex is the systematic uncertainty from vertex shift as explained in Section 8.1.10. The number of events in the fiducial volume before and after the artificial shift are counted and compared (Fig. 8.9). The systematic uncertainty on the total flux due to the external event cut is estimated $\pm 0.1\%$.

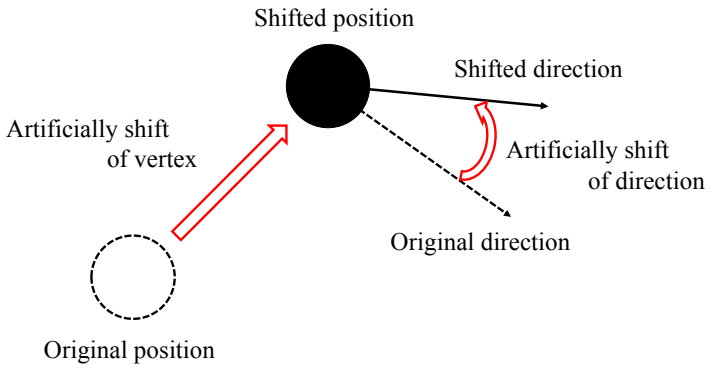

Figure 8.8: Figure of method for shifting the vertex and the direction.

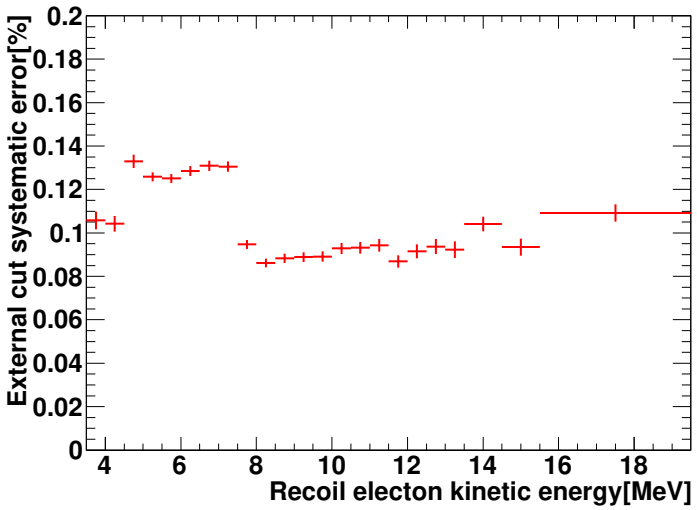

Figure 8.9: The systematic uncertainty of the external event cut.

8.1.10 Vertex shift

Actually, there is the small difference between the reconstructed vertex position and an elastic scattering position within the vertex resolution. It is named vertex shift. The vertex shift is estimated by using the Ni calibration [29]. The systematic uncertainty on the total flux due to the vertex shift which could move events in or out of the fiducial volume is +0.2%/0.0% by the following step:

1. Calculate the vertex shifts at each position by the Ni-Cf calibration
2. Count the number of the events in the fiducial volume
3. Shift the reconstructed z + 0.7 cm (when z > 0 m) or the reconstructed z - 2.7 cm (when z < 0 m) or the radius direction 1.78 cm.
4. Count the number of event remaining in the fiducial volume, and comparing number of events before and after artificially shift are shown in Fig. 8.10.

8.1.11 Background shape

The background probability function is made from the zenith angle distribution and the azimuthal angle distribution. The function assuming the flat azimuthal angle distribution is made, and the systematic uncertainty is estimated by comparing with the total flux from the original function. The systematic uncertainty on total flux in the background shape is ±0.1%.

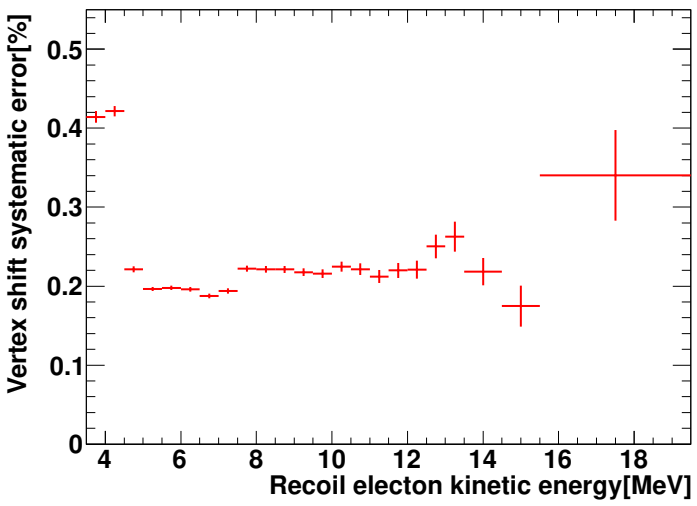

Figure 8.10: The systematic uncertainty of the vertex shift.

8.1.12 Multiple scattering goodness

The LINAC calibration data and the LINAC MC simulation of the MSG distribution are matched by applying a scaling factor to the LINAC MC simulation.

1. Calculate the peak value of the MSG distribution of LINAC data and the MC simulation by the gaussian fitting as shown in Fig. 8.11. First, the mean and RMS of the MSG distribution are extracted, and then estimated by gaussian fit in the range from (mean - RMS) to (mean + RMS).

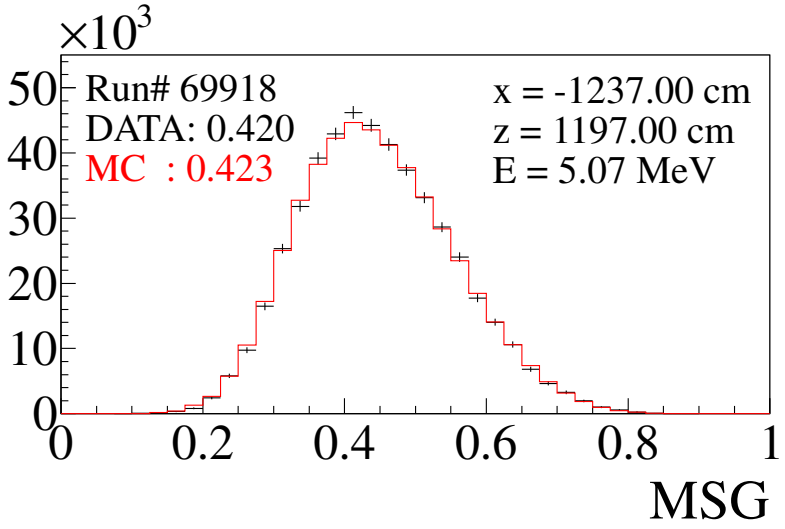

Figure 8.11: The MSG distribution of LINAC data and the MC simulation.

2. Compare the peak value between the data and the MC simulation as shown in Fig. 8.12.

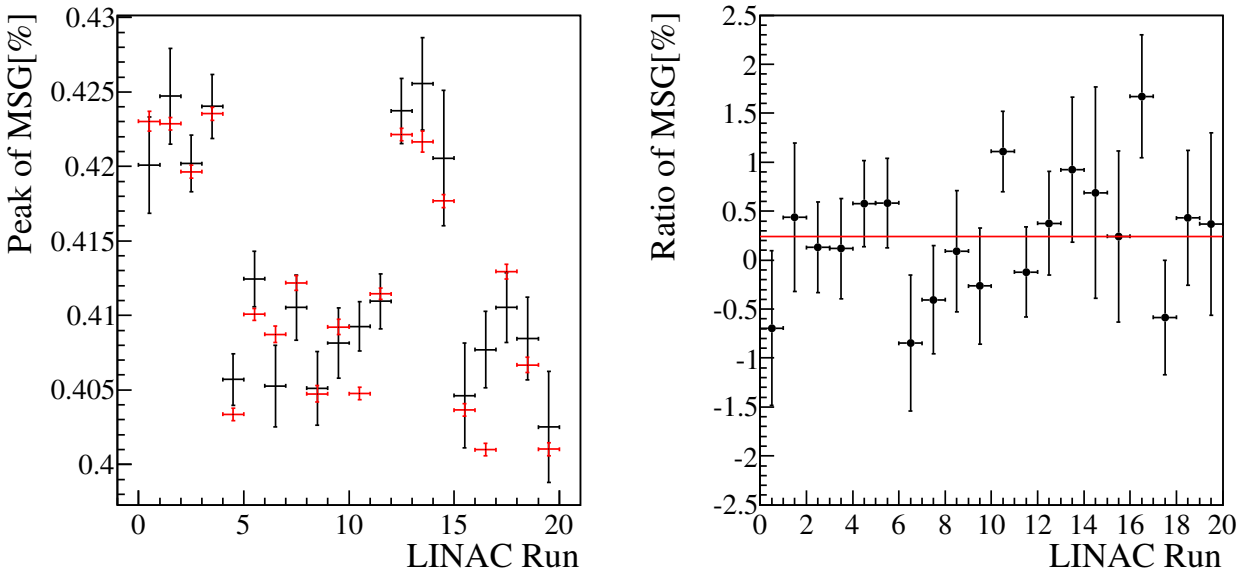

Figure 8.12: (Left) The peak values of the MSG distribution of LINAC data and the MC simulation for around 4 MeV. (Right) The ratio of peak values of the data and MC ((DATA-MC)/MC× 100[%]). Red line show the average of the peak ratios.

3. Correct the event rate of solar neutrino MC (Y_{ij}) and estimate the total flux by the signal extraction in the energy range from 3.5 MeV to 19.5 MeV. The systematic uncertainty on total flux from the MSG is ± 0.4%.

8.1.13 Livetime

As described in Section 6.1, the analytical unit (run) for SK is consisted of a lot of subruns. The run selection is performed every run or subrun as mentioned in Section 6.1. However, for example, there are timing gaps about 67 s when switching day to night in a subrun. The systematic uncertainty of the total flux on the livetime loss occurred by the gap is ±0.1%.

8.1.14 Cross section

The systematic uncertainty of the cross section of the neutrino-electron elastic scattering for the solar neutrino is estimated in Ref. [40]. In the paper, the $\pm 1\sigma$ theoretical uncertainty in parameters of radioactive correction is estimated. Therefore, the systematic uncertainty of the total flux due to the cross section estimated by using the expected recoil electron spectrum with the uncertainty.

8.1.15 Summary of systematic uncertainty on total solar neutrino flux

Summary of the systematic uncertainty on the total solar neutrino flux is shown in Table 8.1. The total systematic uncertainty of SK-IV is ±1.6% by adding the systematic uncertainties of each components in quadrature.

Table 8.1: Summary of the systematic uncertainty on the total solar neutrino flux for each SK phase including that of SK-I [3], SK-II [41] and SK-III [42]

	SK-I	SK-II	SK-III	SK-IV
Threshold (MeV)	4.49	6.49	3.99	3.49
Trigger Efficiency	0.4%	0.5%	0.5%	0.1%
Angular Resolution	1.2%	3.0%	0.7%	0.1%
Reconstruction Goodness	$^{+1.9}_{-1.3}$%	3.0%	0.4%	0.5%
Hit Pattern	0.8%	–	0.3%	0.4%
Small Hit Cluster	–	–	0.5%	$^{+0.5}_{-0.4}$%
External Event Cut	0.5%	1.0%	0.3%	0.1%
Vertex Shift	1.3%	1.1%	0.5%	0.2%
Second Vertex Fit	0.5%	1.0%	0.5%	–
Background Shape	0.1%	0.4%	0.1%	0.1%
Multiple Scattering Goodness	–	0.4%	0.4%	0.4%
Livetime	0.1%	0.1%	0.1%	0.1%
Spallation Cut	0.2%	0.4%	0.2%	0.2%
Signal Extraction	0.7%	0.7%	0.7%	0.7%
Cross Section	0.5%	0.5%	0.5%	0.5%
Subtotal	2.8%	4.8%	1.6%	1.3%
Energy Scale	1.6%	$^{+4.2}_{-3.9}$%	1.2%	1.0%
Energy Resolution	0.3%	0.3%	0.2%	0.1%
^{8}B Spectrum	$^{+1.1}_{-1.0}$%	1.9%	$^{+0.3}_{-0.4}$%	$^{+0.4}_{-0.3}$%
Total	$^{+3.5}_{-3.2}$%	$^{+6.7}_{-6.4}$%	2.2%	1.6%

As a result, the total systematic uncertainty of the total solar neutrino flux is improved from 1.7% [27] to 1.6%. It is due to that the uncertainty of the energy scale is improved. The reason would be considered that the data statistics is increased in the low energy region by changing the SLE trigger threshold from 34 hits to 31 hits.

8.2 Systematic uncertainty on energy spectrum

The systematic uncertainties on the energy spectrum are calculated by using the same methods at each energy bin.

8.2.1 Energy-correlated systematic uncertainty on energy spectrum

The energy-correlated uncertainties are consisted of the energy scale, the energy resolution and the ^{8}B solar neutrino spectrum. The distributions of the energy correlated systematic uncertainties on the energy spectrum is shown in Fig. 8.13.

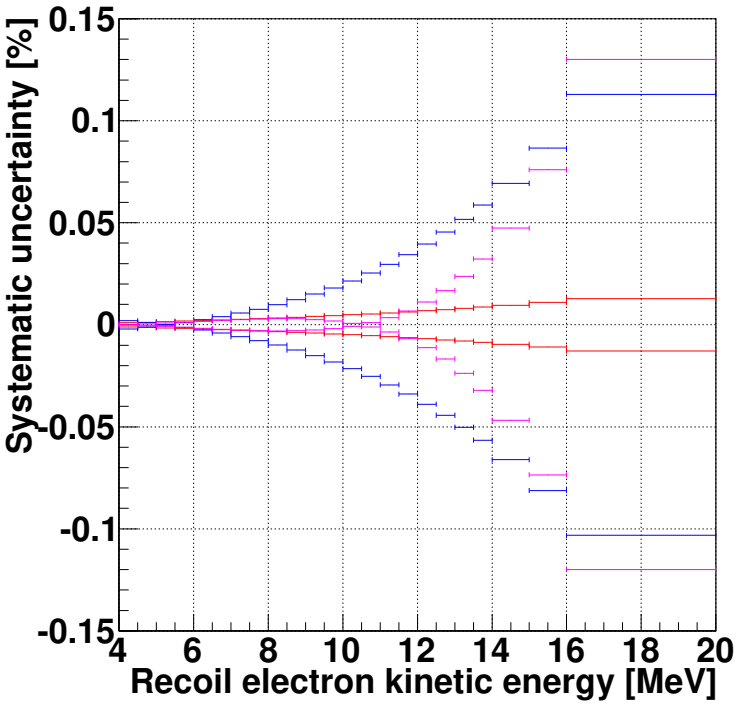

Figure 8.13: Energy correlated systematic uncertainty of the energy spectrum. The distribution corresponds to the gray area in Fig. 9.5. The blue line, the purple line and the red line correspond to the systematic uncertainty of the energy scale, energy resolution and ^{8}B spectrum, respectively.

8.2.2 Energy uncorrelated systematic uncertainty on energy spectrum

The energy uncorrelated systematic uncertainties on the energy spectrum are summarized in Table 8.2. The systematic uncertainties correspond to the red error bar in Fig. 9.5. The systematic uncertainty on the trigger efficiency in only 3.5 MeV to 5.0 MeV of the kinetic energy shows in Fig. 9.5 because the trigger efficiency in the energy range is not 100%. The systematic uncertainty on the Hit pattern cut is estimated above 6.0 MeV of the kinetic energy because the cut is applied in the only energy range.

Table 8.2: Energy-uncorrelated systematic uncertainties of the energy spectrum.

Energy (MeV)	3.49-3.99	3.99-4.49	4.49-4.99	4.99-5.49	5.49-5.99	5.99-6.49	6.49-6.99	6.99-7.49	7.49-19.5
Trigger Efficiency	$^{+6.4}_{-5.6}$%	±0.9%	-	-	-	-	-	-	-
Reconstruction Goodness	±1.4%	$^{+1.5}_{-1.4}$%	$^{+1.4}_{-1.3}$%	±1.1%	$^{+0.4}_{-0.8}$%	±0.6%	±0.5%	±0.3%	±0.1%
Hit Pattern	-	-	-	-	-	$^{+0.9}_{-0.8}$%	±0.7%	±0.6%	±0.3%
External Event Cut	±0.1%	±0.1%	±0.1%	±0.1%	±0.1%	±0.1%	±0.1%	±0.1%	±0.1%
Vertex Shift	±0.4%	±0.4%	±0.2%	±0.2%	±0.2%	±0.2%	±0.2%	±0.2%	±0.2%
Background Shape	±2.9%	±1.0%	±0.8%	±0.2%	±0.1%	±0.1%	±0.1%	±0.1%	±0.1%
Signal Extraction	±2.1%	±2.1%	±2.1%	±0.7%	±0.7%	±0.7%	±0.7%	±0.7%	±0.7%
Cross Section	±0.2%	±0.2%	±0.2%	±0.2%	±0.2%	±0.2%	±0.2%	±0.2%	±0.2%
MSG	±0.5%	±0.4%	±0.4%	±0.4%	±0.4%	±1.1%	±1.1%	±1.1%	-
Total	$^{+7.5}_{-6.8}$%	$^{+2.8}_{-2.9}$%	$^{+2.7}_{-2.6}$%	±1.2%	$^{+1.0}_{-1.2}$%	±1.7%	±1.6%	±1.5%	±0.8%

Chapter 9

Results from solar neutrino analysis

First of all, results of the solar neutrino measurement in SK are described. After that, I will discuss by including other solar neutrino experiments.

9.1 Total number of the solar neutrino event

^{8}B solar neutrino event rate measured by the SK detector in SK-IV is shown in Fig. 9.1. In this analysis, we use dataset of the total livetime 2860 days in SK-IV from Oct. 2008 to Dec. 2017 and in the energy range from 3.5 MeV to 19.5 MeV of the electron kinetic energy. Total number of the solar neutrino signal is extracted from the $\cos\theta_{\rm sun}$ distribution as mentioned in Chapter 7.

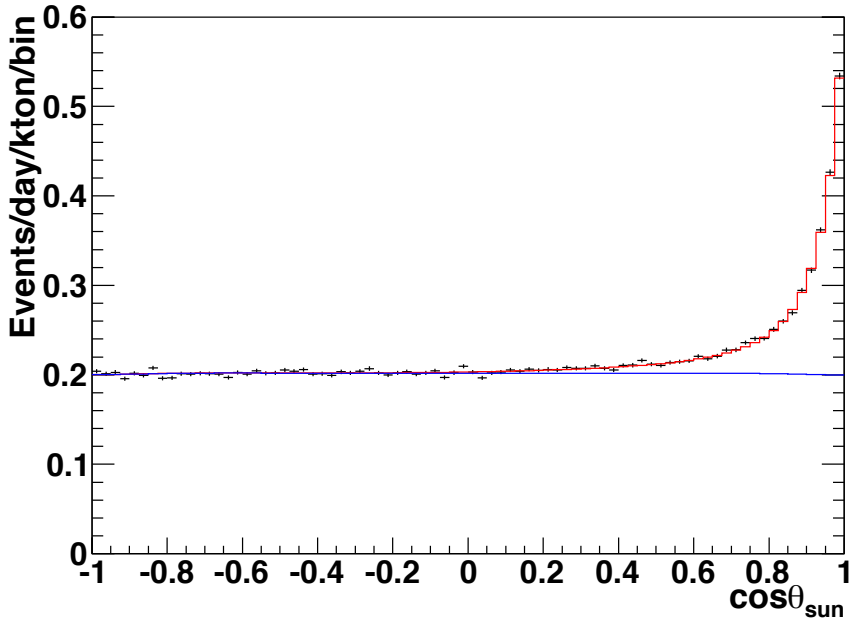

Figure 9.1: Angle distribution of the event rate during SK-IV from 3.5 MeV to 19.5 MeV. Red line shows the best-fit of the signal distribution and blue line shows the best-fit of the background distribution.

The observed number of solar neutrino events in SK-IV:

$$N_{\rm obs} = S = 55,810 \pm 360\,({\rm stat.}) \pm 543\,({\rm syst.}) \tag{9.1}$$

$N_{\rm obs}$ is the number of the solar neutrino events observed by SK detector. It corresponds to the free parameter (S) of the likelihood function for the signal extraction (Eq. 7.1). The observed number of the events isn't included an eccentricity correction, which will be explained in Section 9.2.

9.2 ^{8}B solar neutrino flux in SK

9.2.1 ^{8}B solar neutrino flux

The ^{8}B solar neutrino flux corresponding to the observed number of events (Eq. 9.1) is explained in this section. The neutrino flux is calculated by using the following equation and by assuming no neutrino oscillation.

$$\begin{aligned} N_{\rm expected}[\,/22.5\,{\rm kton}] = & \\ & \left\{ \sum_{\rm MC=^8B,hep} \frac{N_{\rm MC,final}(E_{\rm low}, E_{\rm high})\,[\,/22.5\,{\rm kton}]}{N_{\rm MC,generated}\,[\,/32.5\,{\rm kton}]} \times R_{\rm MC,expected}\,[\,/{\rm day}/32.5\,{\rm kton}] \right\} \\ & \times L(\cos\theta_{z,{\rm low}}, \cos\theta_{z,{\rm high}})\,[{\rm days}] \times e_{\rm orbit} \end{aligned} \tag{9.2}$$

$N_{\rm expected}$ is the number of the solar neutrino events expected from the MC simulation without neutrino oscillation. $N_{\rm MC,generated}$ (MC = ^{8}B or hep) is the total number of all the generated MC events without any cut in the ID (32.5 kton). $N_{\rm MC,final}$ is the number of MC events remaining after all the reductions within the specified energy region in the fiducial volume (final sample in the right of Fig. 6.15). L is livetime between $\cos\theta_{z,{\rm low}}$ and $\cos\theta_{z,{\rm high}}$ in Fig. 3.3. For example, the day/night analysis in Section 9.3 uses different $\cos\theta_z$ regions. $R_{\rm MC,expected}$ is a solar neutrino event rate expected to occur in the ID of SK and is shown in Table 4.1. In this analysis, expected event rates from SNO NC ^{8}B flux (294.7 events/day) and BP2004 hep flux (0.6375 events/day) are used. The eccentricity correction ($e_{\rm orbit}$) is the orbit correction between the Earth and the Sun. Since the distance between the Earth and the Sun ($d_{\rm sun-earth}$[A.U.]) has an annual modulation, the observed solar neutrino flux is expected to vary with the annual modulation by a factor of $1/d^2_{\rm sun-earth}$. Therefore, as the eccentricity correction, livetime averaged $e_{\rm orbit}$ ($= d^2_{\rm sun-earth}$) is multiplied in Eq. 9.2.

The total neutrino flux during SK-IV, in 3.5 MeV - 19.5 MeV, is calculated using the number of observed signal ($N_{\rm obs}$) taking into account of the eccentricity correction ($e_{\rm orbit} = 1.0015$).

$$\text{DATA/MC} = N_{\rm obs}/N_{\rm expect} = 0.437 \pm 0.003\,({\rm stat.}) \pm 0.007\,({\rm syst.}) \tag{9.3}$$

In this analysis, because the hep neutrino flux is so small as to be ignorable as compared with the ^{8}B flux, we consider only ^{8}B solar neutrinos. The ^{8}B solar neutrino flux is obtained by multiplying the DATA/MC by SNO NC flux ($\Phi^{^8B}_{\rm SNO,NC} = 5.25 \times 10^6$ /cm^2/s) in Table. 4.1 as follows.

$$\Phi_{^8\mathrm{B}}(\mathrm{SK-IV}) = (2.295 \pm 0.015\,(\mathrm{stat.}) \pm 0.037\,(\mathrm{syst.})) \times 10^6/\mathrm{cm}^2/\mathrm{sec} \tag{9.4}$$

Table 9.1 is a summary of the total neutrino flux at each SK phase and combined flux taken quadratic sum of those fluxes of all SK phases. The total solar neutrino fluxes consistent in whole SK phases within the total uncertainty as shown in Fig. 9.2.

Table 9.1: Summary of the total neutrino flux at each SK phase. Energy threshold shows the kinetic energy of recoil electrons. The neutrino fluxes of the phases except for that of SK-IV are referred to [27].

Phase	Energy region [MeV]	Livetime [days]	^{8}B neutrino Flux [$\times 10^6/\mathrm{cm}^2/\mathrm{s}$]
SK-I	4.5-19.5	1496	$2.380 \pm 0.024(\mathrm{stat.})\ ^{+0.084}_{-0.076}$ (syst.)
SK-II	6.5-19.5	791	$2.41 \pm 0.05(\mathrm{stat.})\ ^{+0.16}_{-0.15}$ (syst.)
SK-III	4.0-19.5	548	$2.404 \pm 0.039(\mathrm{stat.}) \pm 0.053(\mathrm{syst.})$
SK-IV	3.5-19.5	2860	$2.295 \pm 0.015(\mathrm{stat.}) \pm 0.037(\mathrm{syst.})$

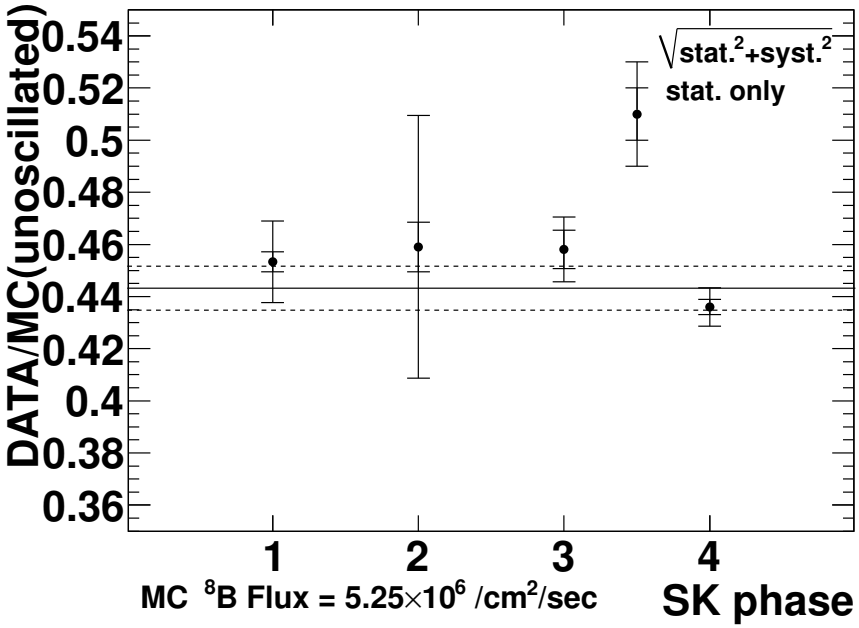

Figure 9.2: The DATA/MC (unoscillated) at each SK phase. The solid line shows the averaged value and the dashed lines shows the 1σ error from the average. The ^{8}B solar neutrino flux is obtained by multiplying the DATA/MC by SNO NC flux ($\Phi^{^8B}_{\mathrm{SNO,NC}} = 5.25 \times 10^6/\mathrm{cm}^2/\mathrm{s}$).

The combined solar neutrino flux from all the SK phases is

$$\Phi_{^8\mathrm{B}}(\mathrm{SK}) = (2.33 \pm 0.04(\mathrm{stat.} + \mathrm{syst.})) \times 10^6/\mathrm{cm}^2/\mathrm{s}. \tag{9.5}$$

The combined neutrino flux is included the data measured by SK for the total live time 5695 days.

9.2.2 Yearly time variation of solar neutrino flux

The Sun spot number modulates with 11 year cycle. We study possible modulation of the solar neutrino flux as shown in Fig. 9.3. Here, since the systematic errors of yearly averaged flux can be assumed to be same as the total flux uncertainty, yearly averaged neutrino flux values are used. For the first time, the neutrino flux from SK data covers both Solar cycle 23 and 24. χ^2 between the SK data points and a constant (averaged) flux is 21.57 at $d.o.f = 21$, then the probability between these distributions is 41.4%. SK solar rate measurement are consistent with a constant solar neutrino flux emitted by the Sun.

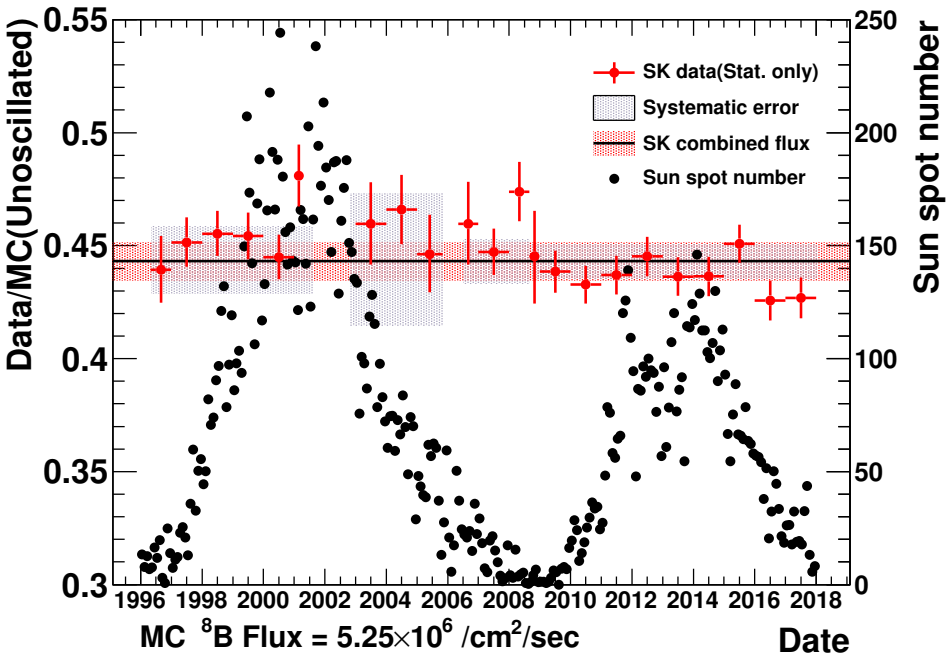

Figure 9.3: The time variation study of the solar neutrino flux of SK. Black points show the Sun spot numbers observed by [43]. The last four SK data points (red cross) are increased from previous paper [27]. The Solar cycle 23 is around from 1996 to 2007, and the Solar cycle 24 is around from 2008 to 2018.

9.3 Day/Night asymmetry

Day/Night asymmetry means that an asymmetry of the neutrino flux during daytime and nighttime. It is a key to find the Earth matter effect of the solar neutrino oscillation. In this thesis, the asymmetry is obtained from the previous paper [27]. In that dataset, the data in daytime of 797 days and in nighttime of 866 days were used. There are two types for estimating day/night asymmetry, a straightforward test and amplitude fit method. In order to be amplitude

fit, the likelihood function described of Eq. 7.1 is modified. In this section, the brief results from the previous paper [27] are explained.

9.3.1 Straightforward test

The straightforward test is an estimation by using the neutrino flux in daytime and nighttime [27].

$$A_{\rm DN} = \frac{\phi_{\rm day} - \phi_{\rm night}}{(\phi_{\rm day} + \phi_{\rm night})/2} \tag{9.6}$$

$\phi_{\rm day}(\phi_{\rm night})$ is defined as the neutrino flux during daytime [$\cos\theta_{\rm z} \leq 0$] (nighttime [$\cos\theta_{\rm z} > 0$]). θ_z is the solar zenith angle illustrated in Fig. 3.3.

9.3.2 Amplitude fit method

The day/night amplitude fit method adopts a maximum likelihood fit to the amplitude of the time variation of the solar neutrino flux [44].

$$A_{\rm DN}^{\rm fit} = A_{\rm DN} \times (\alpha \pm \sigma_\alpha) \tag{9.7}$$

Here, α, a day/night scaling factor, is one of free parameters for maximization of the likelihood in Eq. 9.9. σ_α is a statistical error of the parameter α. A_i represents the expected day-night asymmetry depending on the oscillation parameter at i-th energy bin.

$$A_i = \frac{r_{i,\rm day} - r_{i,\rm night}}{(r_{i,\rm day} + r_{i,\rm night})/2} \tag{9.8}$$

The $\rm r_{i,day(night)}$ show the day (night) rate at i-th energy bin, respectively. The free parameters, B_i, S and α, are determined by maximization of the likelihood function describe in Eq. 9.9.

$$\mathcal{L}_{\rm time} = {\rm e}^{-(\sum_i B_i + S)} \prod_{i=1}^{N_{\rm bin}} \prod_{j=1}^{N_{\rm MSG_i}} \prod_{k=1}^{n_{ij}} (B_i \cdot b_{ijk} + S \cdot Y_{ij} \cdot s_{ijk} \times z_i(\alpha, t)) \tag{9.9}$$

The modified maximum likelihood for day/night asymmetry includes the time dependence of the solar zenith angle $z_i(\alpha, t)$ in the signal component of Eq. 7.1.

$$z_i(\alpha, t) = \frac{1 + \alpha((1+\alpha_i) r_i(t)/r_i^{\rm av} - 1)}{1 + \alpha \times \alpha_i} \tag{9.10}$$

$$\alpha_i = \frac{1}{2} A_i \times \frac{1}{2} L_{\rm DN} \tag{9.11}$$

$$L_{\rm DN} = \frac{L_{\rm D} - L_{\rm N}}{(L_{\rm D} + L_{\rm N})/2} \tag{9.12}$$

The $\rm r_i^{av}$ show the total averaged rate at i-th energy bin. α_i is an effective asymmetry parameter estimated from the day/night asymmetry livetime (L_{DN}) at i-th energy bin. L_D is livetime in day and L_N is livetime in night.

9.3.3 SK day/night asymmetry results

Results of the day/night asymmetry for SK-IV in kinetic energy 4.5 MeV to 19.5 MeV is described in this section as shown in Fig. 9.4. The day/night asymmetry of the total livetime 1664 days, livetime of day 797 days and livetime of night 866 days in SK-IV is estimated. The systematic uncertainty of the day/night asymmetry are estimated by [27].

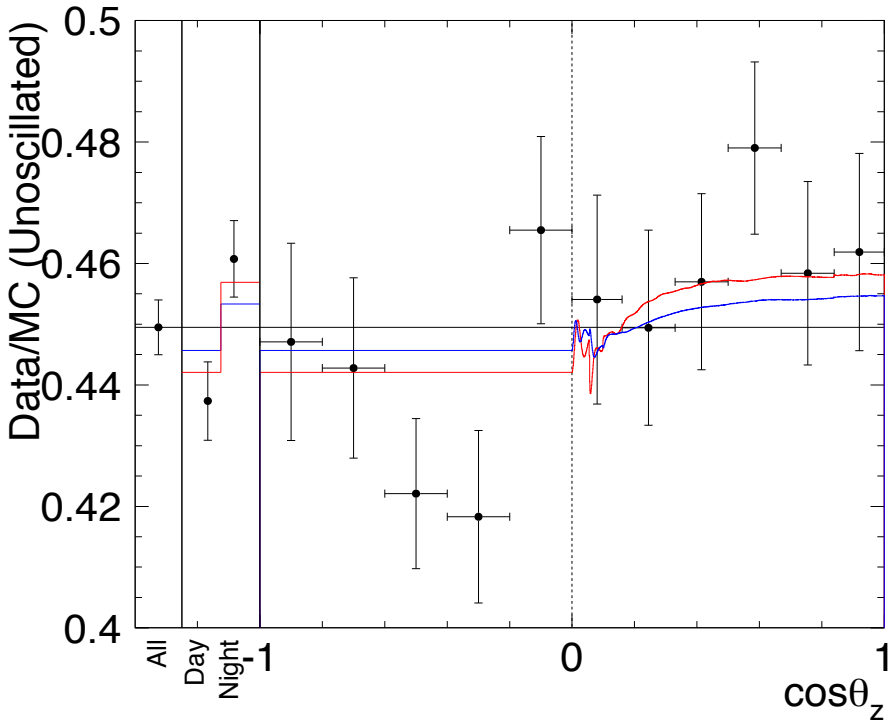

Figure 9.4: The zenith angle distribution of Data/SSM in energy range from 4.5 MeV to 19.5 MeV. Red (blue) lines show predictions of the solar neutrino data (solar neutrino data + KamLAND) best-fit oscillation parameters. The error bars show only the statistical uncertainty [27].

The day/night asymmetry measured by the straightforward method of SK-IV is

$$A_{\mathrm{DN}} = (-4.9 \pm 1.8\,(\mathrm{stat.}) \pm 1.4\,(\mathrm{syst.}))\%. \tag{9.13}$$

The day/night amplitude fit measured by SK-IV is

$$A_{\mathrm{DN}}^{\mathrm{fit,SK-IV}} = (-3.3 \pm 1.5\,(\mathrm{stat.}) \pm 0.6\,(\mathrm{syst.}))\%. \tag{9.14}$$

The combined day/night asymmetry of all SK phase is

$$A_{\mathrm{DN}}^{\mathrm{fit,SK}} = (-3.3 \pm 1.0\,(\mathrm{stat.}) \pm 0.5\,(\mathrm{syst.}))\%. \tag{9.15}$$

These results mean SK observed more neutrinos in the night time. It is an indication of the MSW effect in the Earth. However, the significance level is not so large, and it is 2.9 σ from the combined amplitude fitting result of SK.

9.4 Energy spectrum

For calculation of the energy spectrum, the flux estimated by using Eq. 9.2 and Eq. 9.3 in the range from E_{low} to E_{high} at each energy bin is used. The energy spectrum of the recoil electron in SK-IV 2860 days is shown in Fig. 9.5. The energy range from 3.5 MeV to 19.5 MeV in kinetic energy is divided into 23 energy bins.

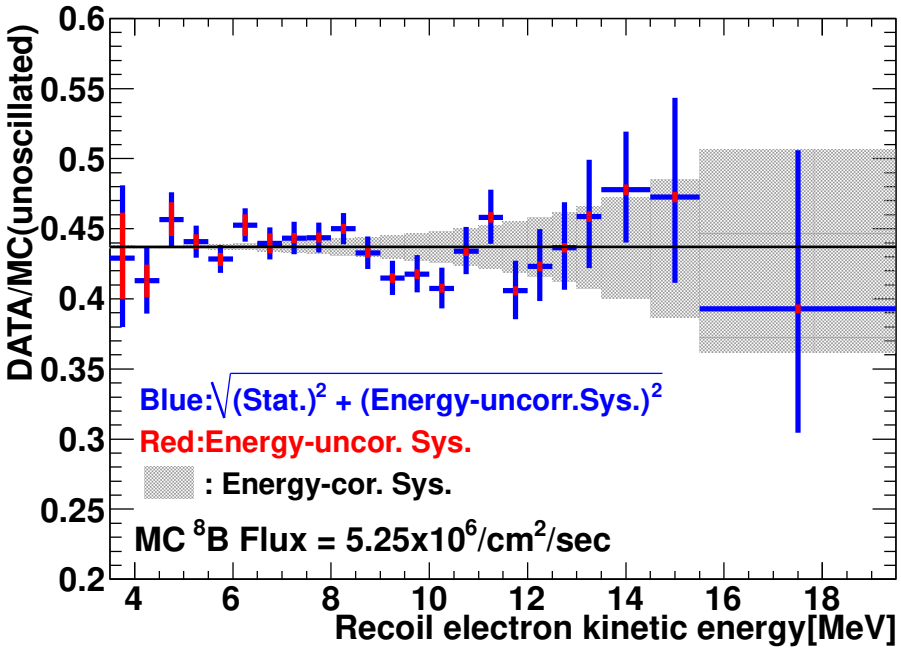

Figure 9.5: The energy spectrum in SK-IV phase. The vertical axis shows the ratio of the observed neutrino flux to the expected unoscillated flux by the solar neutrino MC simulation. The black line shows the averaged value of DATA/MC.

9.5 Oscillation analysis

In this section, we carried out neutrino oscillation among three flavor neutrinos under constraint of $\sin^2\theta_{13} = 0.0219 \pm 0.0014$ [27,45]. Here, definition of variables for energy are E_e means true recoil electron total energy and E shows observed recoil electron total energy.

9.5.1 Calculation of electron neutrino survival probability

We estimate the electron neutrino survival probability of the solar neutrinos. The electron neutrino survival probability (p_e) in vacuum corresponds to Eq. 2.9 with α = electron, but matter effect must be also considered. As a first step, a table of mass eigenstate of a neutrino after oscillation in the Sun is created since it takes very long time. As the vacuum oscillation from the Sun to the Earth, the oscillation calculation is done at each $L_{lm}/20$ step in Eq. 2.6. In the matter oscillation in the Earth, in order to consider the matter effect when the solar neutrinos propagate through the Earth, the zenith angle bin in the night are finely divided. The cosine of zenith angle ($\cos\theta_z$) are divided into 1001 bins (z_j, $j = 1 \sim 1001$, day = 1 bin, night =1000 bins). The calculation in the vacuum and in the Earth is done for each observed electron energy (E) and solar direction ($z_j = \cos\theta_z$), then taking phase average of vacuum oscillation, then $p_e(E, z_j, \theta_{12}, \theta_{13}, \Delta m^2_{21})$ is obtained.

9.5.2 Expected event rate assuming the oscillation

Expected event rate in the SK detector assuming the oscillation is calculated using the electron neutrino survival probability estimated in Section 9.5.1.

$$r^{\mathrm{MC}}(E, z_j, \theta_{12}, \theta_{13}, \Delta m^2_{21}) = \Phi_{\mathrm{MC}} \int_{E_e} dE_e \int_{E_\nu} dE_\nu \phi_{\mathrm{MC}}(E_\nu) dE_e R(E_e, E) \left(p_e \frac{d\sigma_{\nu_e}}{dE_e} + (1 - p_e) \frac{d\sigma_{\nu_{\mu/\tau}}}{dE_e} \right) \tag{9.16}$$

$$\Phi_{\mathrm{MC}} = \frac{N_{\mathrm{MC,final}}}{N_{\mathrm{MC,generated}}} \times R_{\mathrm{MC,expected}} \times e_{\mathrm{orbit}} \tag{9.17}$$

$R(E_e, E)$ is the detector response function defined by

$$R(E_e, E) = \frac{1}{\sqrt{2\pi}\sigma(E_e)} \exp\left\{ -\frac{(E - E_e)^2}{2\sigma(E_e)^2} \right\} \tag{9.18}$$

$\sigma(E_e)$ is the energy resolution function described in Eq. 5.4. $\frac{d\sigma_{\nu_e}}{dE_e}$ ($\frac{d\sigma_{\nu_{\mu/\tau}}}{dE_e}$) is a differential cross section of elastic scattering of a electron (muon/tau) neutrino and an electron. $\phi_{\mathrm{MC}}(E_\nu)$ (MC = ^{8}B or hep) represents normalized solar neutrino energy spectrum. Φ_{MC} is the expected event rate of ^{8}B (hep) in SK, similar as Eq. 9.2.

Next, the expected event rate of ^{8}B and hep neutrino with averaged Earth matter effect are estimated. $B^{\mathrm{osc}}(E, \theta_{12}, \theta_{13}, \Delta m^2_{21})$ ($H^{\mathrm{osc}}(E, \theta_{12}, \theta_{13}, \Delta m^2_{21})$) is the expected rate of ^{8}B (hep) neutrino events after averaging the Earth matter effect, and it is calculated as follows.

$$B^{\rm osc}(E,\theta_{12},\theta_{13},\Delta m^2_{21}) = \sum_{j=1}^{1001} \frac{L(z_j)}{L_{\rm total}} \times r^{\rm {}^8B}(E,z_j,\theta_{12},\theta_{13},\Delta m^2_{21}) \tag{9.19}$$

$$H^{\rm osc}(E,\theta_{12},\theta_{13},\Delta m^2_{21}) = \sum_{j=1}^{1001} \frac{L(z_j)}{L_{\rm total}} \times r^{\rm hep}(E,z_j,\theta_{12},\theta_{13},\Delta m^2_{21}) \tag{9.20}$$

$r^{\rm {}^8B(hep)}(E,z_j,\theta_{12},\theta_{13},\Delta m^2_{21})$ shows the expected rate of the ^{8}B(hep) neutrino at j-th z bin. $L_{\rm total}$ is the total livetime (SK-IV: 2860 days) and $L(z_j)$ is the livetime at j-th z bin. Then, Eq.s 9.19 and 9.20 are integrated over each i-th observed electron energy spectrum bin.

$$B^{\rm osc}_i(\theta_{12},\theta_{13},\Delta m^2_{21}) = \int_{E_{low,i}}^{E_{high,i}} B^{\rm osc}(E,\theta_{12},\theta_{13},\Delta m^2_{21})dE \tag{9.21}$$

$$H^{\rm osc}_i(\theta_{12},\theta_{13},\Delta m^2_{21}) = \int_{E_{low,i}}^{E_{high,i}} H^{\rm osc}(E,\theta_{12},\theta_{13},\Delta m^2_{21})dE \tag{9.22}$$

$B^{\rm osc}_i$ ($H^{\rm osc}_i$) are the expected rate of ^{8}B (hep) neutrino events with the neutrino oscillation at i-th energy bin. $E_{high,i}$ ($E_{low,i}$) is high (low) boundary of i-th energy bin of the energy spectrum.

In the case without the neutrino oscillation, the expected rate of ^{8}B (hep) neutrino events is calculated as $p_e = 1$ in Eq. 9.16. The unoscillated expected rate of ^{8}B (hep) neutrino at i-th energy bin is written as B_i (H_i) in the next Section.

9.5.3 Spectrum shape fitting

Taking into account of energy spectrum distortion effect, observed solar neutrino rates on the energy spectrum are compared with the predicted event rates at each energy bin, and then the χ^2 formula is defined by the following equation in a SK phase.

$$\chi^2_{\rm spec}(\beta,\eta,\theta_{12},\theta_{13},\Delta m^2_{21}) = \sum_i \frac{(d_i - (\beta b_i(\theta_{12},\theta_{13},\Delta m^2_{21}) + \eta h_i(\theta_{12},\theta_{13},\Delta m^2_{21})))^2}{\sigma^2_{i,\rm stat}} \tag{9.23}$$

The index i shows i-th energy bin of the energy spectrum, β and η are free parameters which are determined by minimization of χ^2, d_i is ratio of observed data to the unoscillated MC prediction without neutrino oscillation, $\sigma_{i,\rm stat.}$ is the statistical error of observed data, and $b_i(h_i)$ is the ratio of the expected ^{8}B (hep) rate with oscillation to the unoscillated MC rate as follows.

$$d_i = \frac{D_i}{B_i + H_i} \tag{9.24}$$

$$b_i = \frac{B^{\rm osc}_i(\theta_{12},\theta_{13},\Delta m^2_{21})}{B_i + H_i} \tag{9.25}$$

$$h_i = \frac{H^{\rm osc}_i(\theta_{12},\theta_{13},\Delta m^2_{21})}{B_i + H_i} \tag{9.26}$$

D_i is the observed rate of the solar neutrino events and d_i corresponds to the DATA/MC in Fig. 9.5.

The energy correlated systematic uncertainties of the energy scale, the energy resolution and the ^{8}B spectrum described in Chapter 8 are considered by adding those terms related to the uncertainties to Eq. 9.23.

$$\begin{aligned}
\chi^2_{\mathrm{spec},p} &= \sum_i \frac{(d_i - (\beta b_i + \eta h_i) \times f(E_i, \tau, \epsilon_p, \rho_p))^2}{\sigma^2_{i,stat}} + \tau^2 + \epsilon_p^2 + \rho_p^2 && (9.27)\\
f(E_i, \tau, \epsilon_p, \rho_p) &= f_B(E_i, \tau) f_S(E_i, \epsilon_p) f_R(E_i, \rho_p) && (9.28)\\
f_x(E_i, x) &= \frac{1}{1 + x\varepsilon_{x^\pm}(E_i)},\ (x = \tau, \epsilon_p, \rho_p) && (9.29)
\end{aligned}$$

$f(E_i, \tau, \epsilon_p, \rho_p)$ is an energy-correlated spectral distortion factor, and τ, ϵ_p and ρ_p are dimensionless parameters to scale the uncertainties ($\varepsilon_{x^\pm}(E_i)$ as shown in Fig. 8.13) and changed until the minimum χ^2 obtained. τ is a constrained nuisance parameter of the ^{8}B spectrum, ϵ_p is the parameter of the energy scale and ρ_p is the parameter of the energy resolution at each SK phase p. Moreover, Eq. 9.27 is constrained by the solar neutrino flux as follows.

$$\chi^2_{\mathrm{spec},p} = \sum_i \frac{(d_i - (\beta b_i + \eta h_i) \times f(E_i, \tau, \epsilon_p, \rho_p))^2}{\sigma^2_{i,\mathrm{stat.}}} + \tau^2 + \epsilon_p^2 + \rho_p^2 + \Phi \quad (9.30)$$

$$\Phi = \left(\frac{\beta - 1}{\sigma_{\Phi^{^8\mathrm{B}}}}\right)^2 + \left(\frac{\eta - 1}{\sigma_{\Phi^{\mathrm{hep}}}}\right)^2 \quad (9.31)$$

Φ represents the flux constraint parameter for β and η, and these errors are substituted as $\sigma_{\Phi^{^8\mathrm{B}}} = 0.040$, $\sigma_{\Phi^{\mathrm{hep}}} = 2.0$. The free parameter β is restricted by the results from the NC reaction of the SNO experiment $(5.25 \pm 0.20) \times 10^6/\mathrm{cm}^2/\mathrm{s}$ and η is restricted weakly around the SSM hep neutrino flux as $(8\ \pm 16) \times 10^3\ /\mathrm{cm}^2/\mathrm{s}$.

Up to here, $\beta^p_{\mathrm{min}}\ (\theta_{12}, \theta_{13}, \Delta m^2_{21})$ and $\eta^p_{\mathrm{min}}\ (\theta_{12}, \theta_{13}, \Delta m^2_{21})$ are calculated by minimizing with Eq. 9.30 at each SK phase.

Then, the remaining energy uncorrelated systematic uncertainties are taken into account as below.

$$\begin{aligned}
\chi^2_{p,\alpha_p}(\beta, \eta, \tau, \epsilon_p, \rho_p, \theta_{12}, \theta_{13}, \Delta m^2_{21}) = &\sum_i \frac{(d_i - (\beta^p_{\mathrm{min}} b_i + \eta^p_{\mathrm{min}} h_i) \times f(E_i, \tau, \epsilon_p, \rho_p))^2}{\sigma^2_{i,\mathrm{stat.}}}\\
&+ \alpha_p \cdot (\beta - \beta^p_{\mathrm{min}}, \eta - \eta^p_{\mathrm{min}}) \cdot \mathbf{C}_p \cdot \begin{pmatrix} \beta - \beta^p_{\mathrm{min}} \\ \eta - \eta^p_{\mathrm{min}} \end{pmatrix} \quad (9.32)\\
\mathbf{C}_p = &\sum_i^{N_{\mathrm{bin},p}} \begin{pmatrix} \frac{b_i^2}{\sigma_i^2} & \frac{b_i h_i}{\sigma_i^2} \\ \frac{b_i h_i}{\sigma_i^2} & \frac{h_i^2}{\sigma_i^2} \end{pmatrix}
\end{aligned}$$

σ_i is combined statistical-energy uncorrelated systematic uncertainties. $\mathbf{C}_p$ is 2×2 curvature matrix to introduce the energy uncorrelated systematic uncertainties in Table 8.2. $\sigma_{p,\mathrm{syst.}}$ is the energy uncorrelated systematic uncertainties for the total neutrino flux of the subtotal uncertainty described in Table. 8.1. To consider $\sigma_{p,\mathrm{syst.}}$, we use the following α_p.

$$\alpha_p = \frac{\sigma^2_{p,\mathrm{stat.}}}{\sigma^2_{p,\mathrm{stat.}} + \sigma^2_{p,\mathrm{syst.}}} \tag{9.33}$$

For example,

$$\sigma_{p=4,\mathrm{stat.}} = \frac{0.015}{5.25} = 0.0029, \sigma_{p=4,\mathrm{syst.}} = 0.013 \times \frac{2.295}{5.25} = 0.0057, \mathrm{then}\, \alpha_{p=4} = 0.21 \tag{9.34}$$

$N_{\mathrm{bin},p}$ is the total number of energy bins of each SK phase p.

Finally, the spectrum fitting of the combined over SK phases is calculated by minimizing the following equation at an oscillation parameter set.

$$\chi^2_{\mathrm{spec,SK}}(\theta_{12}, \theta_{13}, \Delta m^2_{21}) = \min_{\tau,\epsilon,\rho,\beta,\eta} \left(\sum_{p=1}^{4} \chi^2_{p,\alpha_p} + \tau^2 + \sum_{p=1}^{4} (\epsilon_p^2 + \rho_p^2) + \Phi \right) \tag{9.35}$$

This $\chi^2_{\mathrm{spec,SK}}$ is used as the chi-square from energy spectrum distortion.

9.5.4 Time variation fitting

Taking into account of a matter effect in the Earth, the time variation (solar zenith angle dependence) of the event rate is considered by modified maximum likelihood function for the signal extraction described in Eq. 7.1.

$$\mathcal{L}_{\mathrm{time}} = \mathrm{e}^{-(\sum_i B_i + S)} \prod_{i=1}^{N_{\mathrm{bin}}} \prod_{j=1}^{N_{\mathrm{MSG_i}}} \prod_{k=1}^{n_{ij}} \left(B_i \cdot b_{ijk} + S \cdot Y_{ij} \cdot s_{ijk} \times \frac{r_i(\cos\theta_z)}{r_i^{\mathrm{ave}}} \right) \tag{9.36}$$

$r_i(\cos\theta_z)$ shows the expected solar neutrino event rate as a function of $\cos\theta_z$ in the i-th energy bin, and r_i^{ave} shows the average of the event rate over all the zenith angle bins. Next, the difference between the original $\mathcal{L}$ in Eq. 7.1 and the $\mathcal{L}_{\mathrm{time}}$ is calculated as described in Eq. 9.37.

$$\chi^2_{\mathrm{time}} = -2(\log\mathcal{L}_{\mathrm{time}} - \log\mathcal{L}) \tag{9.37}$$

This χ^2_{time} is used as the chi-square from day/night asymmetry.

9.5.5 Oscillation results by SK

Finally, χ^2_{SK} is calculated by summation of Eq. 9.35 and Eq. 9.37.

$$\chi^2_{\mathrm{SK}} = \chi^2_{\mathrm{spec,SK}} + \chi^2_{\mathrm{time}} \tag{9.38}$$

χ^2_{SK} is calculate every oscillation parameter set (θ_{12}, θ_{13}, Δm^2_{21}) and determined uniquely when θ_{12}, θ_{13}, Δm^2_{21} are shifted. Next, χ^2_{SK} map is made and the set of (θ_{12}, θ_{13}, Δm^2_{21}) which has the smallest χ^2_{SK} becomes the best-fit for the oscillation parameters. The allowed region of the oscillation parameters estimated by using a general $\Delta\chi^2$ method from the χ^2_{SK} minimum point.

The results of the best-fit neutrino oscillation parameters from SK are

$$\sin^2\theta_{12,\mathrm{SK}} = 0.332^{+0.027}_{-0.022} \tag{9.39}$$

$$\Delta m^2_{21,\mathrm{SK}} = (4.73^{+1.35}_{-0.80}) \times 10^{-5}[\mathrm{eV}^2] \tag{9.40}$$

and are shown in Fig. 9.6.

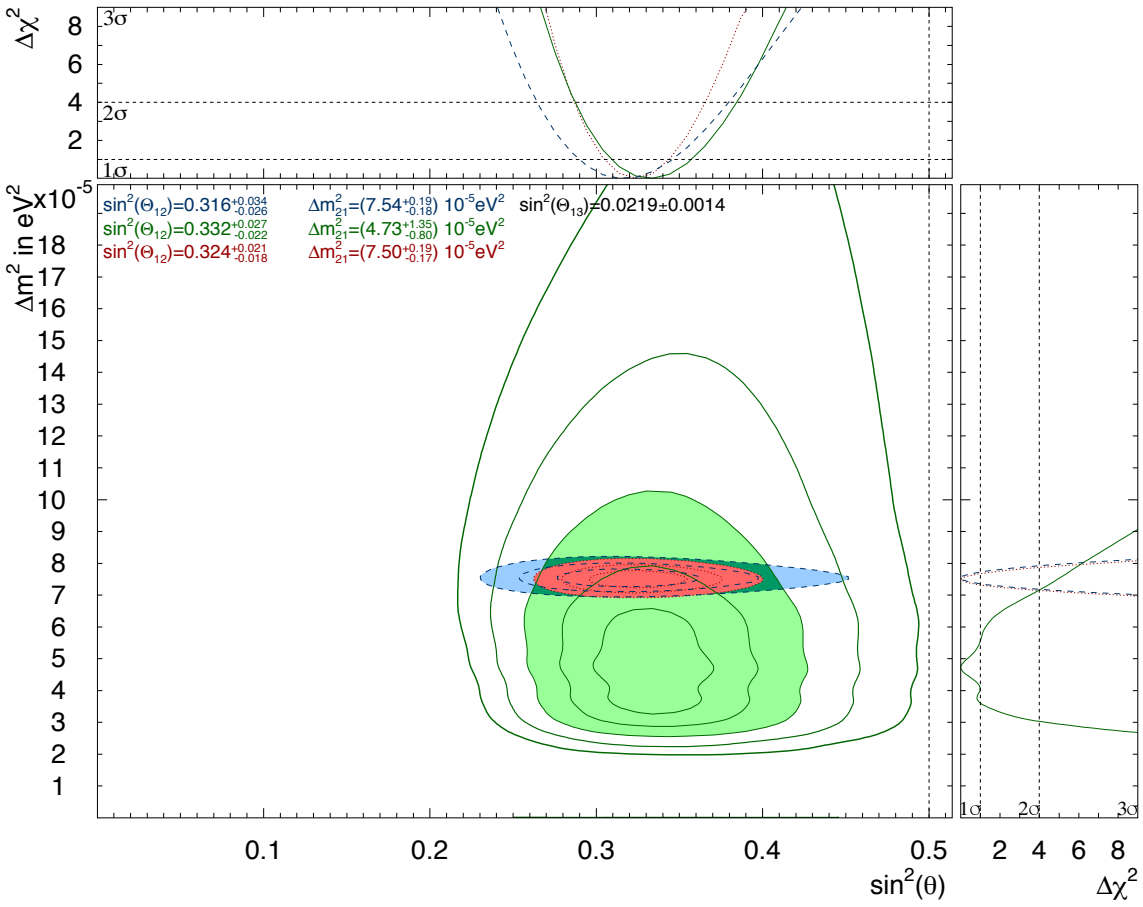

Figure 9.6: Oscillation parameters allowed by this analysis. Green area: SK contour (3σ), blue area: KamLAND contour (3σ) and red area: SK+KamLAND combined (3σ). Green solid lines: SK contour 1, 2, 3, 4, 5σ C.L. Blue dashed line: KamLAND contour (1, 2, 3σ C.L.). Red dotted line: SK + KamLAND contour (1, 2, 3σ C.L.).

Chapter 10

Discussion

As remaining problems, the spectrum upturn and the tension of Δm^2_{21} between solar and reactor neutrino experiments are described in Section 2.6. In this Chapter, these remaining problems are discussed.

10.1 Energy spectrum and electron neutrino survival probability results

Figure 10.1 shows the energy spectrum in the previous analysis (right) [27] and in this thesis (left) (same as Fig. 9.5). In the energy region of (4.5 - 5.0 MeV), the data was more than 2σ away from the averaged flux (black line) in the previous analysis, but the data of this analysis becomes consistent within 1σ.

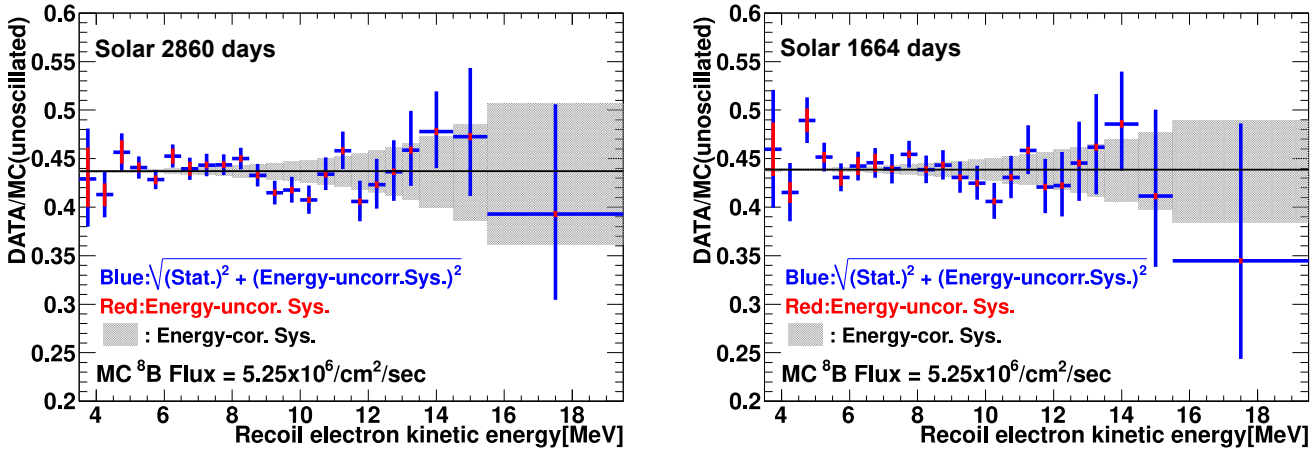

Figure 10.1: The energy spectrum corresponding to the data set of (Left) this thesis and (Right) the previous paper in SK-IV phase. The vertical axis shows the ratio of the observed neutrino flux to the expected unoscillated flux by the solar neutrino MC simulation.

The reason of this large shift in 4.5 - 5.0 MeV energy bin would be the increase of statistics because the tight fiducial volume cut of this analysis in Section 6.6.1 is loosen relative to that of

the previous analysis in the energy region. The tight fiducial volume cut in the previous analysis was

$$z < -7.5\,\mathrm{m}\,\mathrm{or}\,r^2 > 180\,\mathrm{m}\,(4.5\,\mathrm{MeV} \leq E < 5.0\,\mathrm{MeV}) \tag{10.1}$$

Therefore, the previous fiducial volume was smaller than that of this analysis as mentioned in Eq. 6.10 in the energy region.

The statistical errors of the energy spectrum in this analysis in the low-energy region is especially smaller than that before due to improvement of the SLE trigger threshold, and then the center value of the DATA/MC at the lowest energy bin decreases also. Therefore, the significance of the spectrum upturn will become weak.

On the other hand, by reconsidering an estimation of the energy resolution systematic uncertainty, the uncertainty is bigger than that of previous results in the high-energy region. Because of this modification, the sensitivity from the oscillation analysis didn't improve so much comparing to the previous analysis.

In order to estimate possible upturn of the electron neutrino survival probability distribution as a function of the neutrino energy ($P_{ee}(E_\nu)$), a parameterized $P_{ee}(E_\nu)$ distribution is introduced [27]. The $P_{ee}(E_\nu)$ distribution from the standard oscillation analysis is fitted with a quadratic function described in Eq. 10.2.

$$P_{ee,par}(E_\nu) = c_0 + c_1\left(\frac{E_\nu}{\mathrm{MeV}} - 10\right) + c_2\left(\frac{E_\nu}{\mathrm{MeV}} - 10\right)^2 \tag{10.2}$$

Using the $P_{ee,par}(E_\nu)$ from the fitted function (instead of $P_{ee}(E_\nu)$ from standard oscillation analysis), the modified expected energy spectrum of the recoil electron $b_{i,par}$ and $h_{i,par}$ (corresponding b_i and h_i in Eq. 9.32) are made, considering the energy resolution function (Eq. 5.4) and the average day/night asymmetry. Then, χ^2 is calculated by using the $b_{i,par}$ and $h_{i,par}$ (instead of b_i and h_i in Eq. 9.23-9.35). Finally, the fitted function giving the smallest χ^2 (χ^2_{min}) becomes the best fit. Among $\Delta\chi^2 = \chi^2 - \chi^2_{\mathrm{min}}$ less than 1, the regions between the maximum and the minimum $P_{ee,par}(E_\nu)$ at each E_ν are defined as 1σ region. For the combined SK and SNO and only SNO, the $P_{ee,par}(E_\nu)$ is estimated by using the similar treatment above.

Fig. 10.2 shows the electron neutrino survival probability distributions as a function of neutrino energy. The $P_{ee,par}(E_\nu)$ distribution from SK + SNO (red curve) is consistent with the $P_{ee}(E_\nu)$ distribution expected from neutrino oscillation at all solar best-fit parameter set (green curve) within 1.2σ and disfavors the $P_{ee}(E_\nu)$ distribution expected from neutrino oscillation at all solar + KamLAND best-fit parameter set (blue curve) by 2.0σ. In the previous results, the SK and SNO combined allowed region (red region) of the quadratic fit was in good agreement with the green and blue curves expected from neutrino oscillation at each best-fit point.

The 1σ region of SK (green area) for the solar 2860 days becomes flatter in comparison with the previous report (solar 1664 days) [27]. Moreover, the SNO result used in both solar 2860 days and 1664 days analyses has a little downturn. Therefore, it is found that the significance of the spectrum upturn of the combined SK and SNO (red line) is slightly decreased in this update (solar 2860 days).

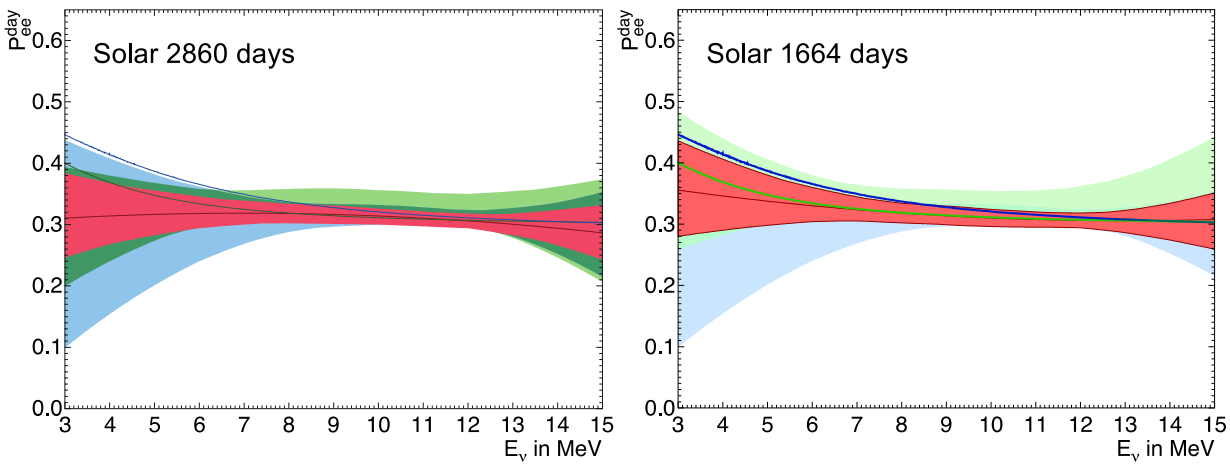

Figure 10.2: The electron neutrino survival probability as a function neutrino energy of (left) 2860 days and (right) 1664 days [27]. The $P_{ee,par}(E_\nu)$ region within 1σ of SK (green) and SNO (blue). The $P_{ee,par}(E_\nu)$ distribution (red line) obtained by fitting to data of SK +SNO within 1σ (red region). Blue line: the $P_{ee}(E_\nu)$ distribution expected from neutrino oscillation at Solar + KamLAND best-fit parameter set , and green line: the $P_{ee}(E_\nu)$ distribution expected from neutrino oscillation at all solar best-fit parameter set (in Section 10.2).

10.2 Oscillation results by all solar and the reactor neutrino experiments

There are several solar neutrino experiments outside of SK as mentioned in Section 2.4. A global oscillation analysis is done and will discuss the results in this section. Results of each experiment are referred to the paper of SNO [22], Gallex/GNO and SAGE [16], Homestake [14], Borexino [23] and KamLAND [24].

The SNO spectrum result is estimated and combined with SK results as follows. The spectrum fitting parameters c_0, c_1 and c_2 mentioned in Section 10.1 are considered with day-night asymmetry fitting parameter $a_0 = 0$ and $a_1 = 0$ obtained from the SNO published results [22]. The SNO's χ^2 ($\chi^2_{\rm SNO}$) is added to $\chi^2_{\rm SK}$ by regarding the SNO result as the fifth phase of SK [46]. Here, not only $\Phi^{^8{\rm B}}_{\rm SNO,NC}$ but also $\Phi^{\rm hep}_{\rm SNO} = (7.9 \pm 1.2) \times 10^3$ [/cm^2/s] from SNO is taken into account.

$$\chi^2_{\rm SK,SNO}(\theta_{12},\theta_{13},\Delta m^2_{21}) = {\rm Min}_{\tau,\epsilon,\rho,\beta,\eta}\left(\sum_{p=1}^{4}\chi^2_{p,\alpha_p} + \tau^2 + \sum_{p=1}^{4}(\epsilon_p^2+\rho_p^2) + \Phi + \chi^2_{\rm SNO}\right) \qquad (10.3)$$

Up to here, minimized $\beta_{\rm min}, \eta_{\rm min}$ and $\tau_{\rm min}$ are obtained.

Next, summation of the signal rate of pp, pep, ^{7}Be, ^{8}B and hep from the radio chemical experiments (Homestake, Gallex/GNO, SAGE) and the signal rate of ^{7}Be from Borexino are considered in this thesis. The χ^2 of Homestake, SAGE, Gallex/GNO and Borexino are merged in

the covariance approach by Eq. 10.4 [47].

$$\chi^2_{\rm covar}(\beta_{\rm min}, \eta_{\rm min}, \tau_{\rm min}, \theta_{12}, \theta_{13}, \Delta m^2_{21}) = \sum_{n,m=1}^{N} (R^{\rm expt}_n - R^{\rm theor}_n)[\sigma^2_{nm}]^{-1}(R^{\rm expt}_m - R^{\rm theor}_m) \qquad (10.4)$$

where, σ_{nm} is the covariance matrix taking into account the correlation of uncertainties of each experiment. $R^{\rm expt,theor}$ are the expected and theoretical rate, respectively, and N (= 3) shows the number of other experiments (Cl, Ga and Borexino).

Finally, the radio chemical chi-square ($\chi^2_{\rm covar}$), the combined SK + SNO chi-square ($\chi^2_{\rm SK,SNO}$) and Eq. 9.37 are added.

$$\chi^2_{\rm ALL} = \chi^2_{\rm SK,SNO} + \chi^2_{\rm time} + \chi^2_{\rm covar} \qquad (10.5)$$

Then, search of θ_{12} and Δm^2_{21} is done under the θ_{13} constraint.

The oscillation parameters allowed by SK, KamLAND and all solar experiments are shown in Fig. 10.3. The result from all solar experiments is

$$\sin^2\theta_{12} = 0.310 \pm 0.014 \qquad (10.6)$$

$$\Delta m^2_{21} = (4.82^{+1.22}_{-0.60}) \times 10^{-5}[eV^2]. \qquad (10.7)$$

Red contour of Fig. 10.3 is the allowed regions within 3σ obtained from a combination of the all solar neutrino experiments and KamLAND. The oscillation parameters from the all solar experiments and KamLAND are

$$\sin^2\theta_{12} = 0.310^{+0.013}_{-0.012} \qquad (10.8)$$

$$\Delta m^2_{21} = (7.49^{+0.19}_{-0.17}) \times 10^{-5}[eV^2]. \qquad (10.9)$$

The result is compared with the oscillation contour plot of the previous analysis [27] as shown in Fig. 2.8. The contour shape of solar global is slightly smaller than that of previous result. The uncertainties of the θ_{12} and Δm^2_{21} parameters are reduced from the previous analysis.

The oscillation results in this analysis show that the tension of Δm^2_{21} between the neutrino and anti-neutrino is still around 2σ level as shown in the right panel in Fig. 10.3, and it is slightly stronger compared with the previous analysis. In the future, it will be expected that the uncertainty of Δm^2_{21} is improved by updating the day-night asymmetry from the solar 1664 days to 2860 days data sets.

The $\sin\theta_{12}$ results of this and previous analyses are consistent. The same uncertainties are obtained. However, the center value of the $\sin\theta_{12}$ is slightly changed from 0.307 [27] to 0.310.

The differences from the previous analysis are described as follows. The data statistics is increased by 1.7 times in SK-IV, and the increase of the livetime is 1196 days. It corresponds to 21% of the livetime in the whole SK phase (5695 days). Moreover, the systematic uncertainties of the total neutrino flux and the energy spectrum are re-estimated. From this re-estimation, the energy resolution uncertainty becomes bigger than that of the previous analysis in the high-energy region. Therefore, the statistical uncertainties are reduced by adding the observed data while the systematic uncertainties are increased due to the re-estimation. As a result, these effects are almost compensated, but the total uncertainties are slightly decreased. The latest results of the

oscillation parameters from Particle Data Group [48] are reported as $\sin^2\theta_{12} = 0.307 \pm 0.013$ and $\Delta m^2_{21} = (7.53 \pm 0.18) \times 10^{-5}$ [eV^2]. In this thesis, the obtained oscillation parameters both $\sin^2\theta_{12}$ and Δm^2_{21} have the same level sensitivity as the current world best results. This is the first time that the results both $\sin^2\theta_{12}$ and Δm^2_{21} from a global solar oscillation analysis achieve the best sensitivity level.

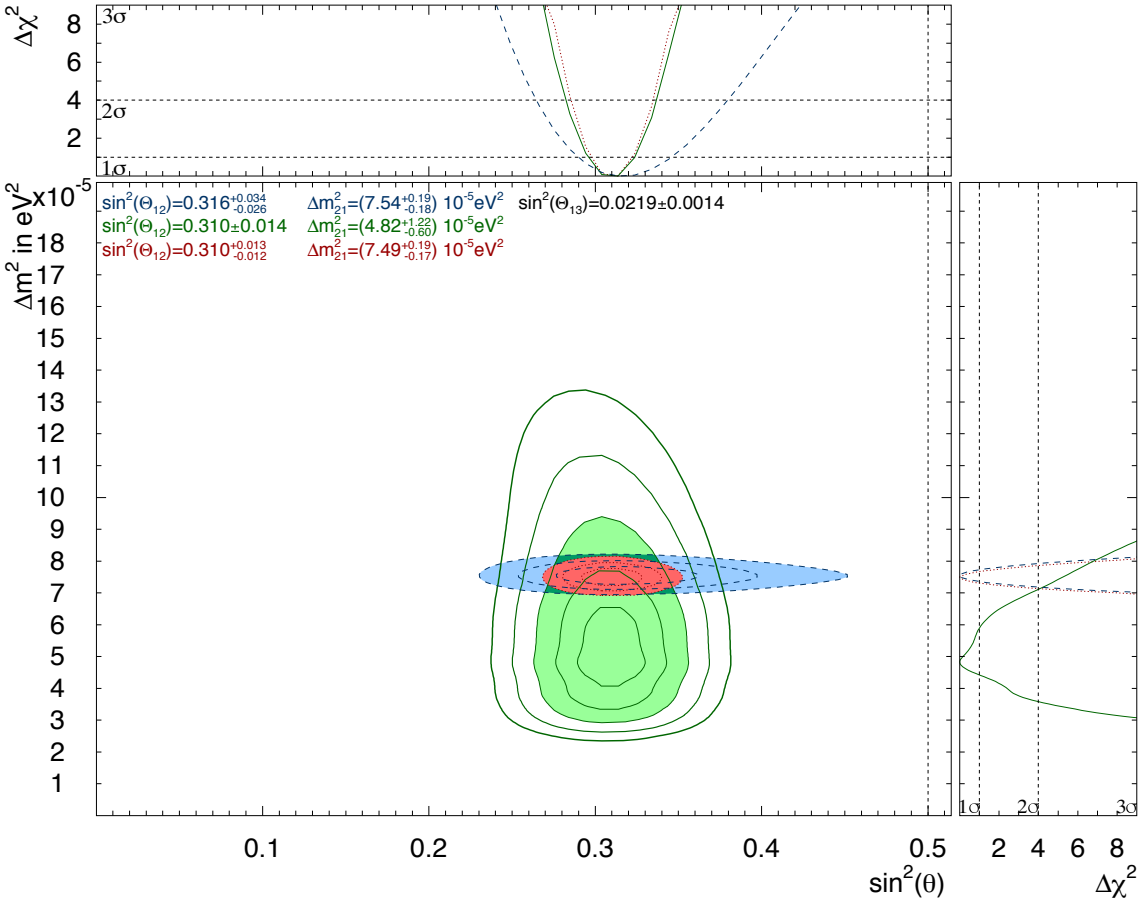

Figure 10.3: Oscillation parameters allowed by the neutrino experiments in this analysis. Blue area shows the KamLAND contour (3σ), green area shows the all solar contour (3σ) and red area shows the results of the combined all solar and KamLAND (3σ). Lines show 1, 2, 3, 4, 5σ C.L. of these oscillation parameters.

Chapter 11

Conclusion

The neutrino oscillation phenomenon provides a global understanding of the SSM and the solar neutrino experiments. However, there are a few remaining problems in the observed results. Among the problems, the spectrum upturn expected from the MSW effect and the tension of Δm^2_{21} between the solar and the reactor neutrino experiments are main research targets in this thesis. For the precise measurement of the solar neutrino, the improvement of the energy scale was done in SK-IV. In this analysis, for the first time, the gain correction is introduced into the energy reconstruction. Therefore, the amount of the used data is increased by 1.7 times, then the precise measurement becomes possible in a whole period of SK-IV. On the other hand, the systematic uncertainty is increased due to the re-estimation. As a result, the total uncertainties are slightly reduced.

The observed number of the solar neutrino events (3.5 -19.5 MeV) in SK-IV (total livetime 2860 days from Oct. 2008 to Dec. 2017) becomes:

$$N_{\rm obs} = 55,810 \pm 360\,({\rm stat.}) \pm 543\,({\rm syst.}). \tag{11.1}$$

The number of the solar neutrino events is increased by 23,919 events from the previous result until Feb. 2014. Then, the total ^{8}B solar neutrino flux of SK-IV is

$$\Phi_{^8{\rm B}}({\rm SK-IV}) = (2.295 \pm 0.015\,({\rm stat.}) \pm 0.037\,({\rm syst.})) \times 10^6/{\rm cm}^2/{\rm s}. \tag{11.2}$$

The flux combined with the all SK phases of 5695 days data is

$$\Phi_{^8{\rm B}}({\rm SK}) = (2.33 \pm 0.04\,({\rm stat.+syst.})) \times 10^6/{\rm cm}^2/{\rm s}. \tag{11.3}$$

Next, the spectrum upturn is evaluated using the electron neutrino survival probability obtained from the recoil electron energy spectrum. The statistical uncertainty of the energy spectrum is decreased in the low-energy region, and the uncertainty of the survival probability is also reduced in the low-energy region. As a result, the survival probability distribution obtained from the combined SK and SNO is consistent with the expected distribution from neutrino oscillation at all solar best-fit parameter set within 1.2σ and disfavors the expected distribution from neutrino oscillation at all solar + KamLAND best-fit parameter set by 2.0σ. Therefore, the significance of the spectrum upturn is slightly decreased in this analysis.

Finally, a standard neutrino oscillation analysis is performed. As a result, the best-fit neutrino oscillation parameters from SK are

$$\sin^2\theta_{12,{\rm SK}} = 0.332^{+0.027}_{-0.022} \tag{11.4}$$

$$\Delta m^2_{21,{\rm SK}} = (4.73^{+1.35}_{-0.80}) \times 10^{-5}[eV^2]. \tag{11.5}$$

The best-fit oscillation parameters from all solar experiments (including SK) are

$$\sin^2\theta_{12} = 0.310 \pm 0.014 \tag{11.6}$$

$$\Delta m^2_{21} = (4.82^{+1.22}_{-0.60}) \times 10^{-5}[eV^2]. \tag{11.7}$$

From KamLAND which is an anti-neutrino reactor experiment, $\sin^2\theta_{12} = 0.316^{+0.034}_{-0.026}$ and $\Delta m^2_{21} = (7.54^{+0.19}_{-0.18}) \times 10^{-5}$ [eV^2] are reported [24]. The tension of Δm^2_{21} between all solar experiments and KamLAND still remains $\sim 2\sigma$.

Then, the oscillation parameters obtained from all solar neutrino experiments and KamLAND is

$$\sin^2\theta_{12} = 0.310^{+0.013}_{-0.012} \tag{11.8}$$

$$\Delta m^2_{21} = (7.49^{+0.19}_{-0.17}) \times 10^{-5}[eV^2]. \tag{11.9}$$

In comparison to the previous results until Feb. 2014, the uncertainties of the $\sin^2\theta_{12}$ is the same level while that of Δm^2_{21} is reduced. These parameters are estimated by using the world's largest amont of the solar neutrino events, and they have the world's best sensitivity level.

Acknowledgements

I was able to carry out this study by receiving cooperation from many people. First, I am thankful to Prof. Y. Takeuchi for giving me the opportunity to participate at Super-Kamiokande which is the world's top class experiment. I truly thank you from the bottom of my heart.

I learned a lot of things about the solar neutrino analysis at SK from Dr. Y. Nakano. I got a lot of advice warmly from Prof. M. Nakahata, Prof. Y. Koshio, Prof. H. Sekiya, Prof. M. Ikeda, Prof. Y. Nakajima, Dr. T. Yano, Dr. S. ito, Dr. H. Ito, A. Orii when I was faced with a problem on this study. I have enjoyed passing the research life thanks to you.

I would like to thank Low-energy group members, Prof. M. Smy, Prof. M. M. Lluis, W. Pierce, L. Scott, W. Linyan. I can get many question and comment in the meeting, and I think that my English ability is improved.

Thank you for support from other SK group members, Prof. Y. Hayato, Prof. S. Mine, Prof. Y. Kishimoto, Prof. J. Kameda.

I would like to thanks staffs of Particle Physics Group at Kobe University, Prof. H. Kurashige Prof. Y. Yamazaki, Prof. K. Miuchi, Prof. A. Ochi, Prof. A. Suzuki, Prof. J. Maeda, Prof. S. Shimizu, Prof. T. Hara. I learned basic of the particle physics from them.

Finally, I have been a lifestyle with fulfilling days thanks to everyone. Thank you.

Makoto Hasegawa
January, 2019

Bibliography

[1] R. Oerter, *The Theory of Almost Everything* (2006)

[2] wikipedia [https://en.wikipedia.org/wiki/Standard_Model]

[3] J. Hosaka et al., Phys. Rev. D 73, 112001 (2006)

[4] B. Pontecorvo, JETP 6, 429 (1957)

[5] L. Wolfenstein, Phys. Rev. D 17 2369 (1978)

[6] L. Wolfenstein, Phys. Rev. D 20 2634 (1979)

[7] S. P. Mikheyev and A. Y. Smirnov, Nuovo Cimento C 9 N1 (1986)

[8] R. N. Mohapatra and P. B. Pal,
Massive Neutrino in Physics and Astrophysics, World Scientific (2004)

[9] J. N. Bahcall et al., Rev. Mod. Phys. 54 767 (1982)

[10] J. N. Bahcall, *Neutrino Astrophysics,* Cambridge University Press (1989)

[11] J. N. Bahcall et al., Astrophys. J. 621 85-88 (2005)

[12] J. N. Bahcall and M. H. Pinsonneault, Phys. Rev. Lett. 92, 121301 (2004)

[13] S. Turck-Chièze et al., Phys. Rep. 230 57-235 (1993)

[14] B. T. Cleveland et al., Astrophys. J. 496 505-526 (1998)

[15] Y. Fukuda et al., Phys. Rev. Lett. 77, 1683 (1996)

[16] J. N. Abdurashitov et al., Phys. Rev. C 80, 015807 (2009)

[17] W. Hampel et al., Phys. Lett. B 447 127-133 (1999)

[18] M. Altmann et al., Phys. Lett. B 616 174-190 (2005)

[19] Q. R. Ahmad et al., Phys. Rev. Lett. 89, 011301 (2002)

[20] B. Aharmim et al., Phys. Rev. C 72, 055502 (2005)

[21] B. Aharmim et al., Phys. Rev. Lett. 101, 111301 (2008)

[22] B. Aharmim et al., Phys. Rev. C 88, 025501 (2013)

[23] M. Agostini et al., arXiv:1707.09279 [hep-ex]

[24] A. Gando et al., Phys. Rev. D 88, 033001 (2013)

[25] K. Abe et al., Phys. Rev. D 97, 072001 (2018)

[26] M. Maltoni and A. Y. Smirnov, Eur. Phys. J. A 52-87 (2016)

[27] K. Abe et al., Phys. Rev. D 94, 052010 (2016)

[28] S. Fukuda et al., Nucl. Instrum. Meth. A 501 418-462 (2003)

[29] K. Abe et al., Nucl. Instrum. Meth. A 737 253-272 (2014)

[30] wikimedia [https://commons.wikimedia.org/wiki/File:Decay_chain(4n%2B2,_Uranium_series).PNG]

[31] S. Yamada et al., IEEE Transactions on Nuclear Science, 57, 428 (2010)

[32] Y. Takeuchi, Ph. D. thesis, University of Tokyo (1995)

[33] Y. Nakano, Ph. D. thesis, University of Tokyo (2015)

[34] M. Ikeda, Ph. D. thesis, University of Tokyo (2010)

[35] GEANT - Detector Description and Simulation Tool, CERN Program Library (1993)

[36] W. T. Winter et al., Phys. Rev. C 73, 025503 (2006)

[37] J. N. Bahcall, Hep energy spectrum, [http://www.sns.ias.edu/∼jnb/SNdata/sndata.html]

[38] M. Nakahata el al., Nucl. Instrum. Meth. A 421 113-129 (1999)

[39] E. Blaufuss et al., Nucl. Instrum. Meth. A 458 638-649 (2001)

[40] J. N. Bahcall et al., Phys. Rev. D 51, 6146 (1995)

[41] J. P. Cravens et al., Phys. Rev. D 78, 032002 (2008)

[42] K. Abe et al., Phys. Rev. D 83, 052010 (2011)

[43] Sunspot Index and Long-term Solar Observations [http://www.sidc.be/silso/datafiles]

[44] M. B. Smy et al., Phys. Rev. D 69, 011104 (2004)

[45] B. Yang, Ph. D. thesis, Seoul Nation University (2010)

[46] A. Renshaw, Ph. D. thesis, University of California (2013)

[47] G. L. Fogli et al., Phys. Rev. D 66, 053010 (2002)

[48] Particle Data Group, *Review of Particle Physics,* American Physical Society (2018)